COMPARATIVE STUDY OF THE EFFECT OF IMPURITIES ON THE DUCTILITY OF TANTALUM AND TUNGSTEN BASED ON ATOMISTIC AND FIRST PRINCIPLES CALCULATIONS

by

Zhiliang Pan

A dissertation submitted to the faculty of
The University of North Carolina at Charlotte
in partial fulfillment of the requirements
for the degree of Doctor of Philosophy in
Mechanical Engineering

Charlotte

2012

Approved by:

_____
Dr. Qiuming Wei

_____
Dr. Laszlo J. Kecskes

_____
Dr. Yong Zhang

_____
Dr. Jing Zhou

ABSTRACT

ZHILIANG PAN. Comparative study of the effect of impurities on the ductility of tantalum and tungsten based on atomistic and first-principles calculations.
(Under the direction of DR. QIUMING WEI)

Tungsten and tantalum are neighbors in the Periodic Table of the Elements and, as refractory metals, both have very high melting points (tungsten: 3422^{o}C, tantalum: 2996^{o}C). However, the ductility of the two metals is quite different especially at commercially available purity levels. Commercial purity polycrystalline tungsten shows brittle behavior in room temperature tensile tests, and its ductile-to-brittle transition temperature (DBTT) can be as high as 400^{o}C. In contrast, commercial purity polycrystalline tantalum shows completely ductile behavior at room temperature, and its DBTT can be as low as -250^{o}C. Based on published work, it has been well accepted that the brittleness of commercial purity tungsten is attributed to weakened grain boundaries (GBs) by segregated impurities. However, this consensus is far less sufficient to elucidate why there is a remarkable difference in ductility between the two metals.

In this work, based on the understanding that ductility is the competition between grain boundary (GB) separation and dislocation activities, we used density functional theory and molecular dynamics to systematically calculate the pristine and contaminated GB separation energy, the GB and dislocation core segregation energy of various impurities, and the effect of impurities on generalized stacking fault energy and Peierls energy of screw dislocations for tungsten and tantalum. The results show that for each impurity species, the GB and core segregation energies in tungsten are always significantly higher than those in tantalum, indicating that impurities in tungsten are more likely to segregate to GB regions

and the vicinity of dislocation core to influence them. The binding energy difference between GB and free surface site for each impurity species in tungsten is always higher than that in tantalum, indicating that the presence of impurities, if deemed undesirable, will cause a greater reduction in GB separation energy for tungsten. In addition, tungsten is more sensitive to sulfur impurity concentration level inside the GB than tantalum. Although both literature and our work have shown that the ductility of pure tungsten is already lower than that of pure tantalum, the remarkable difference of impurity effect on between the two metals makes the ductility of tungsten suffers more from the deleterious impurities than the ductility of tantalum. The analyses of the chemical and mechanical effects of impurities suggest that tungsten is more sensitive to impurities because of its low lattice constant and thus small interstitial sites despite other possible causes. The calculations of the effect of impurities on the dislocation related properties are not adequate to compare the impurity effect on between tungsten and tantalum due to the inappropriately chosen reaction paths.

ACKNOWLEDGMENTS

I would like to express my gratitude to Dr. Qiuming Wei and Dr. Laszlo Kecskes for advising me on my research. Thanks to Dr. Yong Zhang and Dr. Jing Zhou for being my committee members and sitting in my proposal and dissertation defenses and giving me valuable suggestions on my research. Thanks to the University Research Computing group for providing leading-edge high-performance computing environment and excellent consulting and assistance to my work. Thanks to the Army Research Laboratory for supporting my research.

TABLE OF CONTENTS

LIST OF TABLES

LIST OF FIGURES

LIST OF ABBREVIATIONS

DFT	density functional theory
MD	molecular dynamics
DD	dislocation dynamics
FCC	face-centered cubic
BCC	body-centered cubic
HCP	hexagonal close-packed
DBT	ductile-to-brittle transition
DBTT	ductile-to-brittle transition temperature
GB	grain boundary
FS	free surface
EAM	embedded atom method
STGB	symmetric tilt grain boundary
GSF	generalized stacking fault
DOF	degree of freedom
PN	Peierls-Nabarro
LDA	local density approximation
GGA	generalized gradient approximation
USPP	ultrasoft pseudopotential
CSL	coincident site lattice

NOMENCLATURE

$2\gamma_{int}$	the ideal work of interfacial separation (the decohesion energy)
$\dot{\varepsilon}$	strain rate
Q	activation energy
σ	stress
V	volume, activation volume
T	temperature
m	strain rate sensitivity
a_0	lattice constant
E_0	cohesive energy
B	bulk modulus
p	pressure
r, r_0	distance
C_{11}, C_{12}, C_{44}	elastic constant of cubic crystal
G	shear modulus
A	anisotropy coefficient
τ	shear stress
ν	Poisson's ratio
$2\gamma_s$	crystal cleavage energy
γ_{us}	unstable stacking fault energy
b	Burgers vector
$\hat{H}$	Hamiltonian operator

ψ	wave function
$n(\vec{r})$	electron density
E	binding energy
E^{DFT}	total energy of the system from DFT calculations
M_{ISO}	total energy of the isolated host atom from DFT calculations
I_{ISO}	total energy of the isolated impurity atom from DFT calculations
$E_{SGL}^{DFT}, E_{GB}^{DFT}, E_{FS}^{DFT}$	total energy of the single crystal, GB, FS systems from DFT calculations
E_{SGL}, E_{GB}, E_{FS}	binding energy of the single crystal, GB, FS systems
γ_{GB}, γ_{FS}	clean GB energy, clean FS energy
$\gamma_{GB}^{I}, \gamma_{FS}^{I}$	contaminated GB energy, Contaminated FS energy
$\mu_{SGL}^{I}, \mu_{GB}^{I}, \mu_{FS}^{I}$	binding energy of the impurity atom in the bulk, at the GB, on the FS site
$2\gamma_{SEP}, 2\gamma_{SEP}^{I}$	separation energy of clean or contaminated GB
$\Delta\mu^{I}$	binding energy difference of the impurity atom between scenarios when it is with the GB and the FS
$\Delta\mu_{GB}^{I}, \Delta\mu_{FS}^{I}$	GB/FS segregation energy impurities
$\mu^{I,Chem}$	chemical binding energy of impurities with the matrix
$\mu^{I,Mech}$	mechanical distortion energy induced by impurities in the matrix
$\mu_{SGL}^{I,Chem}$	chemical binding energy of the impurity in the bulk site
$\mu_{GB}^{I,Chem}$	chemical binding energy of the impurity at the GB site
$\mu_{FS}^{I,Chem}$	chemical binding energy of the impurity on the FS site
$\mu_{SGL}^{I,Mech}$	mechanical distortion energy induced by the impurity atom in the bulk site

$\mu_{GB}^{I,Mech}$	mechanical distortion energy induced by the impurity atom at the GB site
$\mu_{FS}^{I,Mech}$	mechanical distortion energy induced by the impurity atom on the FS site
$\Delta\mu_{GB}^{I,Chem}, \Delta\mu_{FS}^{I,Chem}$	chemical contribution of the GB, FS segregation energy
$\Delta\mu_{GB}^{I,Mech}, \Delta\mu_{FS}^{I,Mech}$	mechanical contribution of the GB, FS segregation energy
k, k_0	spring constant
$\gamma_{\{xxx\}}(x)$	GSF energy of clean {xxx}plane at displacement x
$\gamma_{\{xxx\}}^{I}(x)$	GSF energy of contaminated {xxx} plane at displacement x
$\Delta E(x)$	Peierls energy at displacement x
$\gamma_{Peierls}$	unstable Peierls energy

CHAPTER 1: INTRODUCTION

Materials and their applications play a decisive role in the development and advancement of science and technologies which conversely advance the discoveries and applications of both natural and artificial materials. The specific applications of materials are determined by their properties. For example, copper can be used as electrical wires to convey electricity from one place to another due to its superior electrical conductivity; while materials with superior mechanical properties may serve as structural components to withstand external loads or as mechanical components to convert thermal energy, electrical energy, etc. into mechanical energy or vice versa. Of the mechanical properties, strength and ductility are probably the most important properties of materials and of the primary concern to designers and engineers when selecting appropriate materials to design and build reliable structural or mechanical systems.

1.1 Conflict between strength and ductility

The strength of materials is their ability to withstand external stress without failure and is intimately related to the bonding energies and lattice constants of materials. In tension tests, it usually refers to tensile strength or to yield strength for ductile materials if yielding is regarded as failure. Ductility is a measure of the degree of plastic deformation and is usually measured in tension tests by elongation to failure or percent reduction in cross section area of the tested specimen. Both strength and ductility represent the resistance of a material to catastrophic failure under various loading conditions and are of

overriding importance to a stable and reliable system. Unfortunately, there exists a paradox between strength and ductility [1]. Materials can be strong or ductile, but rarely both at the same time [2, 3], not to mention those materials that are both weak and brittle simultaneously. It is incumbent upon materials scientists to improve the ductility of high strength materials or to increase the strength of ductile materials or to make a respectable combination between strength and ductility. To the best of the author's knowledge, a large amount of work has been performed for the physical understanding of strength, such as ideal cleavage strength, ideal shear strength, and yield strength; and it is feasible to predict the strength of materials utilizing computer simulations based on density functional theory (DFT) [4], molecular dynamics (MD), and dislocation dynamics (DD) [5, 6]. However, much less work has been reported for the understanding of ductility, especially the conflict between strength and ductility, and methods to reconcile such conflict.

1.2 Ductile to brittle transition behavior

Solid materials can be grouped into three basic classifications: metals, ceramics and polymers [7]. Most of the metals, according to their crystal structures, can be grouped into three categories: face-centered cubic (FCC), body-centered cubic (BCC), and hexagonal close-packed (HCP). Usually ceramics such as aluminum oxide, silicon carbide etc. are brittle; FCC metals, such as copper, gold etc. are ductile; whereas there exist some materials whose ductility or brittleness is dependent on the ambient temperature. These materials exhibit a ductile to brittle transition (DBT) behavior at a characteristic temperature, i.e. ductile to brittle transition temperature (DBTT). Materials with DBT behavior are brittle when the ambient temperature is lower than DBTT, ductile when the

ambient temperature is higher than DBTT. Typical examples include most of the BCC metals, such as iron, tungsten, and tantalum etc., and their alloys.

1.3 Comparison between tantalum and tungsten

Tantalum and tungsten are two of the five widely used refractory metals (the metals whose melting points are equal to or greater than that of chromium [8]) and both are very difficult to melt. The melting point of tantalum is as high as 2996 ºC, about two times that of iron, whereas tungsten has the highest melting point of all metals, which is about 3422 ºC. Due to their high melting points, they can be used as crucibles, filaments or in other kinds of high temperature applications. Tantalum and tungsten are neighbors in the periodic table of the elements; the atomic numbers of the two elements are 73 and 74 respectively. Both as very dense metals, the mass density of tantalum is 16.65 kg/m^3, more than two times that of iron, while the density of tungsten is still much higher, about 19.25 kg/m^3. The most stable crystal structures of both metals are BCC structure and they both have very high cohesive energy, 8.1eV for tantalum and 8.9eV for tungsten [9]. Despite their proximity in many physical properties, there are significant differences in their mechanical properties, prominently in their strength and ductility.

The mechanical properties of tantalum and tungsten are well documented in the literature. The representative results are summarized in Table 1. From the data provided in Table 1 we can see that for both single crystalline and polycrystalline cases, despite the discrepancies among various authors, the DBTT of tantalum is always much lower than that of tungsten. At room temperature, polycrystalline tantalum is ductile with more than 20% elongation, whereas commercial purity polycrystalline tungsten is completely brittle even though its tensile strength is more than double that of tantalum. Although the DBTT

of metals strongly depends on mechanical, structural, and chemical conditions [10], there is no doubt that the ductility of tantalum is always higher than that of tungsten, given that the comparison is made under similar conditions.

Table 1-1: Properties of tantalum and tungsten documented in the literature

	Tantalum		Tungsten	
Melting point (°C)	2996		3422	
Cohesive energy (eV)	8.1		8.9	
Mass density (kg/m^3)	16.65		19.25	
Lattice structure	BCC		BCC	
	Single crystal	Polycrystalline	Single crystal	Polycrystalline
DBTT (K)	Ductile at 4.2K [11, 12] (High purity)	23 [13]	77 [14] (High purity)	Brittle at RT [15] (Commercial)
		~25 [16]	Ductile at 77K [17]	~350 [18, 19]
			Ductile at 199K [20, 21]	508-553 [22] (Commercial)
			370-470 [23, 24] (Pre-cracked)	573 [14] (Commercial)
				756 [25] (Commercial)
				589 [26]
				673 [27] (As sintered)
RT Strength (MPa)	~100 [12] (High purity)	~200 [28]	~800-900 [20]	~560 [15]
		~240 [29]		
RT Elongation		>20% [28]	27% [15]	

1.4 Nature of ductility

To understand the remarkable difference in ductility between tantalum and tungsten, we need to understand the nature of ductility. Cottrell [30] gave a fundamental and profound description on how solid material deforms from atomistic level, "*When a large force is applied to a crystal two things may happen; the atoms in the crystal may slide past one another; and they may pull apart.*" The slide of atoms, such as nucleation or generation or movement of dislocations, twinning, and detwinning etc. leads to permanent shear deformation or plastic deformation of the crystal, the amount of which before fracture is defined as ductility. For crystalline materials, the primary source of plastic deformation comes from dislocation activity. The pulling apart of atoms results in bond breaking and cleavage of the crystal, and represents brittle behavior. Generally speaking, ductility is determined by the competition between dislocation activities and cleavage (transgranular fracture), or the failure at some weak links within the material such as grain boundaries (intergranular facture).

1.5 Three ways to understand the difference in ductility between tantalum and tungsten

Based on the understanding of ductility, many efforts have been undertaken to address the issue of brittleness of tungsten mainly through three approaches. The first approach concerns primarily the role of grain boundaries (GBs) in the deformation of polycrystalline materials based on the premise that the brittleness is attributed to the weak GBs or low GB separation energy [31]. The second approach concerns primarily the role of dislocations in the deformation of materials based on the premise that the high ductility of materials is attributed to the easy activation of dislocation activities, and it is difficult to nucleate/generate or move dislocations in brittle materials. The third approach attempts to

provide a holistic picture by taking into account the roles of both GBs and dislocations. In other words, it looks at the competition between dislocation activities and GB behavior at crack tips. It is based on the notion that dislocation nucleation occurs first at crack tips of ductile materials that will blunt the crack tip, whereas crack propagation occurs first in brittle materials. The following three sections will summarize the findings in the literature relevant to this issue.

1.5.1 The role of grain boundaries and grain boundary segregation

In polycrystalline materials, GBs play an important role in determining the mechanical properties such as ductility and strength. During tensile test, brittle materials fail through intergranular fracture, i.e. crack propagation is along GBs [7]; whereas ductile materials fail though intragranular fracture, resulting in fracture surface consisting of numerous spherical “dimples” [7]. The direct interpretation of the difference in fracture behavior between brittle and ductile materials is that the cohesion of GBs is a controlling factor limiting the ductility of materials [32]. In other words, qualitatively, materials with strong GBs are ductile, and those with weak GBs are brittle. Since the DBTT of single crystal tungsten is lower than that of polycrystalline tungsten, and the addition of impurity level to polycrystalline tungsten results in an increase in DBTT [33], the room temperature brittleness of commercial purity polycrystalline tungsten is attributed to the weakened GBs by the segregated impurity atoms.

GB segregation of impurity atoms occurs in many polycrystalline materials which inevitably changes the cohesion of GBs and thus the mechanical properties. Usually the presence of impurities inside GBs has a deleterious effect on the mechanical properties by embrittling the host material. Typical examples include hydrogen [34, 35], phosphorus,

and sulfur and so on in iron and steel [31, 36], sulfur in nickel [31, 37], bismuth in copper [31, 38-41], and oxygen, phosphorus, sulfur and so on in tungsten [14, 33]. Sometimes the segregated impurities inside GBs have a beneficial effect by enhancing the cohesion of GBs and thus improve the ductility of the host materials. Examples are provided by boron or carbon in iron [42, 43], zirconium, aluminum, boron, or carbon in molybdenum [44, 45], boron or carbon in tungsten [46-48], and boron or zirconium in nickel based alloys [49].

To improve the mechanical properties of polycrystalline materials, material scientists need to exploit the beneficial effect of some impurities on GBs and at the same time to reduce or circumvent the detrimental effects of some other impurities. Since in the periodic table there are so many elements that can be either impurities or host atoms, it is unrealistic for material scientists to discover the optimum conditions merely through trial and error, a labor-intensive, time-consuming and tedious approach, even though it has been used by human beings probably since the Bronze Age. As an alternative, therefore, we need to understand the underlying mechanisms or reasons why and how these impurities affect the GBs so as to guide our design of and search for new advanced materials.

1.5.1.1 Experimental investigation of grain boundary segregation

Although some consensus has been reached hitherto in several specific cases, the understanding of why and how impurities affect the mechanical properties of GBs is still evolving. In what follows, it will be described and summarized in approximately chronological order. Decker [49] investigated the effect of boron and zirconium on creep-rupture properties of nickel based alloy in 1960, and found out that the existence of proper amounts of boron and zirconium retard the micro-cracking and thus slow down the rupture process. Kameda [50] investigated the effect of antimony on the fracture behavior

of an alloy steel in 1980, and found out that antimony can lower the intergranular cohesive energy, reduce the stress field of a crack tip that is necessary to initiate dislocations, and thus decrease the local dislocation activities at crack tips. He [35] also investigated the hydrogen-induced intergranular fracture behavior of an alloy steel doped and undoped with phosphorus, tin or antimony and proposed a dynamic model which attributes the hydrogen embrittlement to the accumulation of hydrogen ahead of a moving microcrack.

1.5.1.2 Atomistic simulation of the effect of segregated impurities

With the advent of powerful computers, more and more researchers began to use computer simulations to unravel the underlying mystery associated with mechanical properties of materials. For example, in his paper where the idea of embedded atom method (EAM) was first proposed, Daw [51] investigated the effect of hydrogen interstitials on nickel single crystals based on atomistic simulations. The result shows that hydrogen can reduce the fracture stress in nickel. Cottrell [43] also utilized the embedded atom theory to make a comparative study of the effect of hydrogen and carbon on crack propagation along the GBs of iron. His results indicate that when a crack propagates along the GBs, the segregated hydrogen interstitials can readily transfer from in-GB state to in-crack state, thus contributing nothing to intergranular cohesion; whereas carbon interstitials make this progress through successive jump, indicating a surplus energy barrier between carbon and its surrounding iron atoms when pulling them apart. This energy barrier will definitely retard the crack propagation and thus enhance the GBs. Dorfman's [32] Monte Carlo atomistic simulations revealed that boron additives can also increase the energy barrier against separation of $\Sigma 3(111)$ GBs in tungsten. Farkas and co-workers [52] investigated the effect of interstitial hydrogen and carbon impurities on

the fracture behavior of Σ5 symmetrical-tilt grain boundary (STGB) of iron using EAM potentials in their molecular dynamics (MD) simulations and observed that the presence of hydrogen inside GBs leads to a transition for crack propagation from an intragranular to intergranular manner, thus embrittles the GB. They also observed that carbon has the opposite effect by inducing the crack to propagate into grain interior.

1.5.1.3 Rice-Wang model of the effect of segregated impurities

The majority of the efforts made so far to understand why and how impurity atoms affect GBs are mostly phenomenological and ambiguous descriptions rather than genuine understanding. This scenario has been changed since 1989 when Rice and Wang [31] proposed their model within a thermodynamic framework for this issue. The Rice-Wang model states that the ideal work of interfacial separation (the decohesion energy) $2\gamma_{int}$ plays an important role in controlling embrittlement. They further suggested that the decohesion energy of segregated GB can be determined as that of clean GB plus the binding energy differences per unit area for impurity atoms at a GB and at a fractured free surface (FS). If the binding energy of segregated impurities with GBs is higher than that with the corresponding FSs, the impurities 'prefer' to stay at GBs rather than FSs, and will increase the ideal work of GB separation and thus enhance the GBs. Otherwise they will embrittle or weaken the GBs.

1.5.1.4 Limitations of the previous investigations

The investigations mentioned above are based on experiments, thermodynamics considerations or atomistic simulations. They have their respective limitations in spite of their merits and contributions to improve our understanding of the issue. Experiments are able to provide tangible evidence that shows the effect of impurities on GBs, but are not

good at elaborating details at atomistic or electronic level. This is especially true for those performed many years ago, before advanced techniques for material characterization were well developed. Theoretical models based on thermodynamics have significantly improved our understanding from the very basic principles. However, the statistical nature of thermodynamics defies analysis in detail which is often important to materials design. Atomistic simulations suffice to give details at atomistic level, but their accuracy and reliability are limited by the empirical interatomic potentials available. For example, although Cottrell [43] successfully simulated the beneficial effect of boron, he failed to simulate the deleterious effect of hydrogen on iron GBs due to the limitations of the empirical potentials. Even though the interatomic potentials have now been derived from *ab initio* calculation data through, for example, force-matching method [53] and are able to give quite accurate expression of interatomic interactions, it is still almost implausible to base the understanding at electronic level on them since the potentials in atomistic simulations are only used to determine the force filed among atoms, although they 'borrow' such concept as electron density from quantum electronic calculations.

1.5.1.5 First-principles calculations of the effect of segregated impurities on GBs

Based on quantum mechanics, first-principles quantum electronic calculations are able to give accurate predictions of interatomic potentials and binding energy without input from empirical data. As such, it can provide a good way to the understanding of the impurity effect on GB separation energy [31] at electronic level. Although it is implausible to apply first-principles calculations to systems as large as those calculated using atomistic simulations, the quite localized nature of impurity effects makes it feasible to use electronic calculations to model the electronic structures of relatively small systems [42] ,

such as an individual grain boundary. In 1982, Messmer [54] presented the results from fully quantum mechanical cluster calculations of various systems (sulfur, phosphorus, and carbon in iron, sulfur and boron in nickel) and related the effect of impurity atoms on GBs to their electronegativity or their ability to draw charge from neighboring host atoms. Strong embrittling impurities such as sulfur atoms have high electronegativity and thus tend to draw charge from the neighboring host atoms to themselves. As a consequence they reduce the charge density which is necessary to hold the GB together and weakened GBs ensue; in contrast, cohesive enhancers such as carbon and boron have relatively low electronegativity and show much reduced tendency to draw charge from the host atoms and thus do not weaken the metal-metal bonds. Instead, these impurity atoms form homo-polar bonds with the host atoms and provide additional enhancement to the host GBs. This is the so-called charge transfer model. Wu and co-workers [55] investigated the effects of phosphorus and boron on the GB cohesion of iron by the local density full potential augmented plane wave method. They attributed the beneficial effect of boron to the iron-boron hybridization or covalent bonding normal to the GBs; whereas the nonhybridization between iron and phosphorus leads to detrimental effect on GB cohesion. This interpretation was supported by Krasko's [56] spin-polarized linear Muffin-Tin Orbital (LMTO) calculations of various impurities (boron, carbon, phosphorus and sulfur) in iron. Krasko and co-worker [57, 58] also investigated the effect of hydrogen on the GB cohesion of iron using the same technique. Their results show that hydrogen and iron form very weak covalent bond due to s-pd hybridization, thus only contributing marginally to the GB cohesion. Furthermore, the hydrogen embrittling effect manifests itself in that it can break the original metallic bonding between the iron atoms without introducing

additional cohesion due to its weakening bonding with the iron atoms, thus decreasing the intergranular cohesion. In addition, in their first-principles and semi-empirical calculations of the effect of impurities on GBs of tungsten, Krasko and co-worker[58, 59] proposed another important mechanism that is beneficial to GB cohesion. Due to its lowest energy inside GBs, boron not only enhances the GB cohesion itself, but it also displaces other impurities that are mostly detrimental to GB cohesion off the segregated GBs. As a result, boron can efficiently increase the GB cohesion. This is the so-called site competition effect.

Geng and co-workers [60] investigated the effect of hydrogen, boron and phosphorus on a $\sum 5$ nickel GB, and suggested that the combining effect of atomic size and chemical bonding behavior of the impurities with the surrounding nickel atoms determines the embrttling behavior. According to their understanding, impurities with small atomic size or strong tendency to form covalent bonding with the host atoms are favorable to increase GB cohesion, whereas those with a large atomic size or ionic bonding with the host atoms decrease GB cohesion. Rez [42] calculated the average *d* band energy of neighboring iron atoms of various impurities (boron, carbon, phosphorus, and sulfur) and stated that phosphorus and sulfur fill more antibonding states than boron and carbon. Moreover, he rejected the charge transfer model since his results show that, in the cases of phosphorus and sulfur, charge is transferred in the direction opposite to that expected from electronegativity considerations. Fen's [61] first-principles calculations of nitrogen and phosphorus in iron GB show that the atomic size effect manifests itself in inducing local distortion of lattice. Another factor that is similar to atomic size effect is bond length effect shown in Dorfman's [32] calculations of boron in tungsten which indicates that the bond

length of boron-boron and boron-tungsten is lower than that of tungsten-tungsten. Based on the intuitive understanding, the impurity that forms short bond tend to attract neighboring host atoms to it, thus increasing the cohesion.

The investigations mentioned above are mostly concentrated on the effect of light impurities on the GBs of transition metals. In fact, transition metals themselves can act as impurities to tune the GB properties of other transition metals. To understand how a transition metal impurity atom influences the GBs, Geng and co-workers [62] calculated the effects of molybdenum and palladium on iron GB cohesion and proposed an electronic level phenomenological model to predict the effect of various segregated substistutional alloy additions on GB cohesion of metallic alloys. Based on their calculations they attribute the embrittlement potency of substitutional additions to three factors: volume effect or volume mismatch due to the size difference between the segregant and the GB site, bonding characters in both the GB and the FS, and the heat of formation of the considered system. Shang and Wang [63] investigated the electronic effects of niobium and vanadium on the GB cohesion of iron and found that the chemical effect and geometry effect of the substitutional segregant play crucial but opposite role in determining the GB cohesion. Here the chemical effect refers to that induced by substitution of the segregant for the GB host atom, without considering structure relaxation; whereas the geometry effect refers only to the structure relaxation contribution.

Janisch and Elsässer [64] investigated the effect of hydrogen, boron, carbon, nitrogen and oxygen on the interfacial cohesion of Σ5 symmetrical tilt grain boundaries (STGB) in niobium and molybdenum. The analysis showed that boron and carbon enhance the GBs by forming angle-dependent covalent-like bonds with neighboring host atoms and

inducing covalent metal-metal bonds across the GB, while hydrogen, nitrogen and oxygen weaken the GB by forming isotropic polar-like bonds with neighboring host atoms. Duscher and co-workers [40] investigated the mechanism behind the embrittlement of copper by bismuth through both experiments and first-principles calculations, and found that the presence of bismuth can render the neighboring copper atoms to take on a zinc-like electronic structure. However, the first-principles calculations of bismuth in copper by Schweinfest and co-workers [39] ruled out the electronic effect and instead supported a simple atomic size effect. This atomic size effect manifests itself in that large bismuth atoms weaken the interatomic bonding by pushing apart the copper atoms at GBs. This standpoint was supported by Lozovoi and co-workers [65] who investigated effect of bismuth, silver, and sodium on copper GB cohesion. Ironically, Geng and co-workers [66] commented that the conclusion of Schweinfest's and co-workers is incomplete and failed to distinguish the chemical and mechanical contributions (atomic size effect or geometry effect). Their own calculation showed that the chemical effect should not be neglected and contributes 35% to the total embrittlement potency. In their investigation of the effect of dopants on gold GB cohesion, Chew and co-workers [67] also suggested that the effect of impurity originates from both mechanical and electronic interactions and dopants with smaller diameter and lower electronegativity than gold are beneficial to gold GBs.

Rez and Braithwaite [68] investigated the effect of boron, carbon, phosphorus, and sulfur on the GB cohesion of iron. They suggested that whether the two grains adjacent to the GB are pushed apart or pulled together is dependent not only on the impurity atomic size, but also on whether the impurity atoms occupy the substitutional or interstitial sites. This is the aforementioned geometry effect or mechanical effect or size (both atomic or GB

site size) effect. Their results negates the charge transfer model and indicates that carbon atoms enhance the GB by forming a carbide phase at the GB, and weaken the GB slightly otherwise. This result is consistent with Rice and Wang's [31] uncertainties about the role of carbon in iron, but is inconsistent with Krasko's [56] work. Yamaguchi and co-workers [37] investigated the sulfur-induced embrittlement of nickel and found that the drastic decrease of GB cohesion is caused by the short-range overlap repulsion among densely segregated and neighboring sulfur atoms inside a GB. Different from many other first-principles calculations, they considered the effect of impurity concentration on the GB cohesion of the matrix material, and this short-range repulsion exists only when the impurity concentration is high enough inside the GB.

Lozovoi and Paxton [69] investigated the effect of boron concentration on the GB cohesion of copper and found that the strengthening effect attains a maximum value when all the interstitial sites inside GB are occupied by boron atoms. Keeping increasing the concentration by substituting the host atoms at the GB will undermine the strengthening effect due to the significant distortions introduced by boron atoms. More importantly, they proposed a ghost impurity cycle [65, 69] to understand the strengthening mechanism. According to their description, the change of GB separation energy due to segregated impurities is attributed to three mechanisms: "host removal" mechanism corresponding to broken host-host bonds by removing host atom, "substitutional structure" mechanism corresponding to the atomic structure distortion caused by the impurity atoms, and "chemical+compressed impurity" mechanism due to the interaction between the impurity and the host atoms.

Many of the aforementioned first-principles investigations of impurity effects on the mechanical properties of GBs, based on the Rice-Wang model, considered only the GB and the FS conditions which in turn correspond to the initial and the final state of a tensile test of the bi-crystal configuration, respectively. Therefore, they have disregarded the role of the specific tensile process which should also be very important to the understanding of the impurity strengthening or weakening mechanisms. In this regard, Yamaguchi and co-workers performed first-principles simple tensile test on a nickel GB doped with sulfur [37] and an iron GB doped with phosphorus and sulfur [70]. In addition, in the calculations of the iron GB, they added solute atoms into the GB progressively, rather than did it once and for all as in the aforementioned other calculations. The results showed that there are two mechanisms responsible for the GB decohesion. The first is the fracture surface stabilization by the segregated solute atoms without interactions between them; the second is GB destabilization by the repulsive interactions among the segregated solute atoms. Due to the convergence issue regarding stressed conditions, first-principles simple tensile test calculation does not include the geometry and cell optimization during the tensile test and thus is at least incomplete to the understanding of impurity effects. Therefore, in their first-principles tensile test calculations on an iron Σ3 GB with and without phosphorus segregation, Yuasa and Mabuchi [71] included the geometry optimization and cell optimization only in the tensile direction and found that the bond formed between iron and phosphorus atoms is broken first. This event accelerates the breaking of the neighboring iron-iron bonds. They attributed the easy-breaking of iron-phosphorus bond to its covalent-like localized bonding and reduced mobility of the electrons. However, both Yamaguchi [37, 70] and Yuasa [71] did not consider the effect of the lateral contraction or

Poisson's ratio effect in their calculations, which, according to Tian and co-workers [72], can remarkably reduce the total energy of both clean and sulfur-segregated nickel Σ5 GBs during tension process. But it only has minor effect on nickel Σ3 GB because of the close packing of (111) planes. They also considered the effect of magnetism on the straining process and found that magnetism noticeably reduces the GB toughness.

1.5.1.6 Comments on the calculation work

Despite the various viewpoints associated with the understanding of the impurity strengthening or weakening mechanisms, the results of the atomistic and especially first-principles calculations in the literature are qualitatively consistent with experimental results. For light impurities in the investigated metals, boron and carbon usually enhance the GBs, while hydrogen, nitrogen, oxygen, phosphorus, and sulfur weaken the GBs. The mechanisms why and how impurities change the GB cohesion are suggested in these first-principles investigations to intimately relate to electronegativity (this leads to the so called charge transfer model.) of the impurity atom, chemical bonding (covalent bonding due to hybridization, or noncovalent bonding) between impurity atoms and neighboring host atoms, mechanical or geometry effect (impurity atomic size effect or volume effect or bond length effect) due to the mismatch between impurity atom and the lattice site at the GB, site competition effect between various impurities, interaction between impurity atoms , and so on and so forth. The charge transfer model has been partly rejected soon after its publication probably because it is only suitable to ionic bonding, and fails to interpret the covalent bonding related strengthening or embrittling mechanisms.

Based on the Rice-Wang model [31], we need to create a GB structure and its corresponding FS structure to calculate the GB separation energy. To calculate the

contributions from various mechanisms [62, 65, 69], we can divide the procedure to generate GB and the corresponding FS with impurities into several virtual steps. Firstly, create a relaxed clean GB and FS. Secondly, remove one of the host atoms inside the GB and the FS if we want to create a GB with substitutional impurity atom. This step will generate a void and break the bonds formed between the removed atom and the neighboring atoms, thus decreasing the GB cohesion. This is the aforementioned host removal effect [65, 69]. For GB with interstitial impurities, the contribution from this effect is zero. Thirdly, insert the impurity atom into the substitutional or interstitial site and relax the position of the impurity atom, but at the same time fix the GB and/or the FS structure. This step is used to calculate the chemical contribution from the inserted impurity atom. Lastly, relax the positions of all the host atoms as well as that of the impurity atom and calculate the mechanical contribution.

However, physically it is almost impossible to discriminate or decouple the contributions from the various mechanisms which eventually come from the Coulombic interactions among the nuclei and the electrons and the quantum mechanics governed interactions among the electrons. For example, the chemical contribution from the impurity atom is influenced by the atomic positions which are more important in determining the mechanical contributions. Another issue pertaining to atomic size effect is how to define the size of an atom because in fact it changes with the bonding environment of the atom of interest. Moreover, we can investigate and assess the effect of various impurities on GB cohesion through first-principles calculations without discriminating the contributions from various mechanisms, provided the utilized model resembles the real GB and FS structure.

Nevertheless, it is still necessary to base the understanding on this many factors. As mentioned earlier, on the one hand, it is not feasible to find out good impurity/matrix combinations through a trial and error approach only since there are so many elements that can be both impurity and matrix material in the periodic table; on the other hand, the first-principles calculations are very expensive and time consuming. The significance of distinguishing various mechanisms is, based on our understanding, to build a direct link between the effect of impurity on matrix material properties and the properties of the impurity itself. It is believed that it will create a simple rule to guide the impurity selection. As a preliminary selection rule, for instance, the criteria used to assess the contributions from various mechanisms need not be exact, and whether the selected combination is good or not relies on further first-principles calculations and experimental verifications. For example, the size of impurity atom can be simply estimated from the atomic volume in the structure of its elemental crystals [62]. In fact, a phenomenological model [62] based on the aforementioned mechanisms has been proposed and is quite consistent with expensive first-principles calculations.

Based on the first-principles calculation work published so far, some consensus has been reached regarding why and how segregated impurities affect the GB properties. In terms of chemical effect, covalent bonding between the impurity atom and the neighboring host atoms is believed to strengthen the GB. In terms of mechanical effect, small impurity atom is preferred to improve the cohesion of GB with interstitial segregants; whereas for GB with substitutional segregants, it is preferred that the atomic size of the impurity atom be less than that of the host atoms. However, based on an intuitive understanding, the most important feature of an impurity atom that tends to strengthen the host GB and that has not

been plainly pointed out in literatures is that it exists in a strong elemental crystal form and favors spatial chemical bonding network with its neighboring atoms. This chemical bond network is necessary to link the host atoms across the GB. Based on this simple rule, the best impurity elements should be in the boron group, the carbon group and transition metal groups. With another two requirements that the impurity should be small and able to form covalent bonds with host atoms, boron and carbon are singled out to be the best candidates to enhance the interstitial atom segregated GBs, since they are the smallest atoms in their respective groups. Obviously, the veracity of this selection result has been proved by computational and experimental results.

First-principles tensile test calculations elaborate further on why and how segregated impurities alter the GB properties. However, despite the various proposed mechanisms, the trend shown in the tensile test calculations can be understood in terms of first-principles calculations based on the Rice-Wang model. The logic is as follows. During tension deformation, each atom responds to attain the lowest possible potential energy. For impurity atom that prefers to stay inside the GB according to the Rice-Wang model, the separation of GB makes its potential energy higher than that of its previous state. As such, the impurity atom will “try” to retard the separation of GB in order to reduce its potential energy as much as possible, and thus a strengthened GB ensues. Whereas for impurity atom that prefers to stay in FS, the GB separation process makes its potential energy lower than its previous state, and therefore the impurity atom will “try” to facilitate the separation of the GB so as to obtain more energy reduction, and thus leads to weakened (embrittled) GB. Therefore, the embrittling potency predicted from first-principles tensile

test calculations should be checked against the predictions from first-principles calculations based on the Rice-Wang model.

Most of the investigations summarized above concentrate on the positive or negative effect of segregated impurity atoms on the host GBs and the underlying mechanisms of such effects. Based on these investigations, it is sufficient to claim that brittleness of commercial purity polycrystalline tungsten is at least partly attributed to the embrittling effect of various impurities. But here one may raise the following question: why do the segregated impurities selectively weaken the GBs of tungsten, while have minor effect on the GB of commercial purity polycrystalline tantalum that is also segregated with various impurities? This question is based on the literature data which has roughly shown that the impurity atoms have similar effect on the GB of various metals. To answer this question, some references proposed that tungsten [73] is sensitive to the impurity level while tantalum [16, 28] has tolerance for interstitial foreign elements. However, it seems that such a statement is just a recast of the same question, rather than the answer to the question. Alternatively, one may ask: What makes tungsten more sensitive to impurity atoms than tantalum; and further what are the underlying mechanisms that render tantalum more tolerant to impurity atoms. At this point, answers to such questions still remain elusive.

1.5.2 Role of dislocations

Depending on the microstructural features such as grain size, crystal structure, and environmental conditions and loading conditions such as temperature and loading rate, the plastic deformation of crystalline materials may proceed through dislocation activities [74], grain rotation and GB sliding [75], twinning [76], and so on and so forth. Dislocation

activities, such as dislocation nucleation from GBs or crack-tips, dislocation multiplication by means of, for example, Frank-Read sources [77] and dislocation movement dominate the plastic deformation mechanism from single crystal down to the nanocrystalline (grain size smaller than 100 nm) regime. Therefore, the properties of dislocations, such as their nucleation, mobility, and so on are important factors influencing the ductility of materials. This notion is based on the aforementioned understanding that ductility is determined by the competition between GB separation and dislocation activities. Dislocation activities are relatively difficult to occur inside hard materials, but easy to take place inside soft materials, vice versa. The conventional wisdom about ductility is that hard materials such as diamond and most ceramics possess low ductility or even complete brittleness, whereas soft materials such as gold, silver exhibit high ductility. This is consistent with experimental observations and the conflict [1, 2] between strength and ductility. As depicted in Table 1, ample experiments have shown that for both single crystal and polycrystalline tantalum and tungsten, no matter whether they are of high or commercial purity, the yield strength of the former is always lower than that of the later. It should be noted here that in the case of polycrystalline tungsten at room temperature or below the DBTT, nearly completely brittle fracture occurs prior to actual yielding. But the fracture strength of tungsten is still much higher than the yield strength of polycrystalline tantalum of similar microstructure (similar particularly grain size). As a consequence, we can come to the following qualitative corollary: dislocation mediated plasticity is difficult to operate in tungsten, yet it is relatively easy in tantalum. Therefore, a number of authors have tried to relate the relatively low ductility and the DBT behavior of tungsten to its dislocation

properties and attempted to interpret the DBT behavior of materials in terms of dislocation activities particularly in front of the crack tips [23, 24, 78].

1.5.2.1 Dislocation activities versus ductility and DBTT

Dislocations are a line defects inside crystalline materials. They can typically be classified into edge dislocations, screw dislocations or mixed type dislocations based on the relationship between dislocation line and the Burgers vector. Based on whether a dislocation introduces or removes stacking faults during its movement, it can also be classified into partial dislocation or full dislocation. Dislocation activities may involve the nucleation, movement, multiplication of dislocations and the interaction between dislocations, just to name a few. During the plastic deformation of crystalline solids, what dislocation activities dominate the deformation process and contribute to most of the plastic strain depends on the specific material (lattice structure), the stress state, temperature, loading rate, microstructures and sometimes the deformation history of the solid. For materials with DBT behavior, the deformation mechanism usually changes with the ambient temperature, which in turn eventually changes the failure mode. For example, based on Wronski and Fourdeus's work [19], polycrystalline tungsten in tension fails through slip induced cleavage in the temperature range 140-490K, while twining is observed at 77K. An investigation [27] on the fracture toughness of tungsten alloys shows that above DBTT, the screw dislocations move through double kink mechanism. Below DBTT, a screw dislocation dissociates into three partial dislocations that are less mobile, and this behavior of screw dislocations is held responsible for the brittle behavior below DBTT. The work of Gumbsch and co-workers [23, 24, 79, 80] of single crystalline tungsten revealed that dislocation nucleation is the limiting factor at low temperature;

while the DBT transition itself and the fracture toughness above DBTT is controlled by the dislocation mobility.

1.5.2.2 Crack and dislocations

Dislocations can affect the ductility and fracture toughness of a crystalline solid through their interactions with cracks. It is well known that cracks are notoriously responsible for the radical reduction of strength due to the crack induced stress concentration which is sensitive to the sharpness of the crack-tip [81]. For ductile materials, it is easy for dislocations to nucleate and move from crack-tips. This will shield or blunt the crack-tips and as such will retard the propagation of cracks. Consequently, more energy has to be dissipated, leading to increased fracture toughness; whereas for brittle or semi-brittle materials, the absence or scarcity of dislocation activities near crack-tips makes this process less probable or even impossible [27, 80]. In addition to the beneficial shielding effect of dislocations on the existing cracks, dislocations can also nucleate cracks that are deleterious to the fracture toughness of the material. For example, the cleavage of tungsten in Wronski's work [19] is induced by slip due to dislocation movement. Another tensile experiment on a tungsten thin foil inside electron microscope showed that micro cracks can be nucleated from dislocation arrays formed during the deformation process [19]. Another unwanted but probably inevitable effect of dislocation activity is that it favors the nucleation and growth of voids from vacancy sites which eventually coalesce to form cracks and lead to fracture of especially ductile materials [82].

1.5.2.3 Strain hardening and ductility

Strain hardening, also known as work hardening, is a common phenomenon where the flow stress of metals and alloys increases with accumulating plastic deformation. Both

experimental [20] and theoretical investigations [83, 84] have shown that strain hardening is due to multiplication and subsequent interactions of dislocations. When the number of dislocations increases dramatically through dislocation multiplication, they interact and intersect with each other, resulting in a dense dislocation network. This will also eventually suppress the nucleation of new dislocations, and also decrease the mobility of existing dislocations. The consequence of this process is that the flow stress becomes higher and higher, until when the dislocation density is saturated, and the flow stress reaches a maximum value and the material begins to fracture. In this connection, strong strain hardening make the stress rapidly reach this maximum value and start to decrease due to the onset of fracture. Therefore, given the same yield strength, strong strain hardening definitely will not lead to very high ductility although strain hardening is necessary to suppress plastic localization or instability such as necking during tensile test according to Considère criterion [85] and Hart criterion [86].

1.5.2.4 Strain rate hardening and ductility

Dislocation activities are thermally activated processes where the activation energy can be overcome by thermal energy and mechanical work by external loading [87-89]. The plastic deformation in terms of strain rate can be described by an Arrhenius type equation as follows [90]:

$$\dot{\varepsilon} = \dot{\varepsilon}_0 \exp\left(-\frac{Q-\sigma V}{k_B T}\right). \tag{1.1}$$

where $\dot{\varepsilon}_0$ is a (pre-exponent) constant, Q is the activation energy, V activation volume, k_B Boltzmann constant, and T absolute temperature. Equation (1.1) can be rewritten as

$$\sigma = \frac{Q}{V} + \frac{k_B T}{V}\ln\left(\frac{\dot{\varepsilon}}{\dot{\varepsilon}_0}\right). \tag{1.2}$$

Equation (1.1) or (1.2) is not a perfect description of a thermally activated process. However, it reflects the basic underlying principle and provides a qualitative relationship between the stress and the imposed strain rate, i.e., the stress increases with increasing strain rate. Based on the conventional wisdom that high yield stress means low ductility or high DBTT, the strain rate can influence the ductility and DBTT. This is particularly true for body-centered cubic metals and some hexagonal close-packed metals [91] and is consistent with experimental observations [73, 80, 92, 93].

According to Gilman [90], the yield stress can be given by:

$$\sigma_y = \frac{Q}{V + AT}, \tag{1.3}$$

where A is a constant, Q is the activation energy. The activation volume V and strain rate sensitivity $m = \frac{\partial \ln \sigma}{\partial \ln \dot{\varepsilon}}$ are related through the following equation [94]:

$$m = \frac{\sqrt{3} k_B T}{\sigma_y V}. \tag{1.4}$$

From equation (1.3) and (1.4) we obtain

$$\sigma_y = \frac{(Q / A)}{T} - \frac{\left(\sqrt{3} k_B / A\right)}{m}. \tag{1.5}$$

Equation (1.5) indicates that the yield stress σ_y increases with decreasing temperature, but with increasing strain rate sensitivity. This means high strain rate sensitivity increases the yield stress, and decreases ductility, which seems to contradict with that superplastic materials must have very high strain rate. Our understanding is that superplastic deformation usually happens at high homologous temperature (half the absolute melting point), and the stress level is dominated by the temperature effect. Another thing is that the mechanism responsible for superplastic behavior is largely different from behavior at low

homologous temperatures, in that superplasticity usually occurs at quite low strain rate, and involves diffusion, GB sliding, dislocation climbing, etc.

1.5.2.5 Impurity effect on dislocations and ductility

When segregated into GBs, impurities can not only influence GB properties such as GB cohesion, but they can also influence dislocations when distributed in the close vicinity of dislocations inside the grain interior. For example, they change the dislocation mobility, and thus change the yield strength and ductility. Interactions between dislocations and impurities such as pipe diffusion [95], strain aging and Cottrell atmosphere [96], etc., control many material properties such as yield strength, tensile strength and ductility, and so on. Usually the impurities in the vicinity of a dislocation have a pinning or dragging effect on the dislocation and as such they lower the dislocation mobility, which in turn increases the yield or tensile strength and decreases the ductility. For example, in addition to its beneficial effect on GB cohesion, when sitting inside the grain interior, carbon can also have embrittling effect on tungsten resulting from the interaction between carbon atoms and dislocations. This effect is evidenced by the increased yield strength [33]. That the interactions between impurities and dislocations in tungsten are responsible for the DBT behavior is also evidenced by Giannattasio's experimental results [73]. These results show that the DBTT of tungsten is very sensitive to the impurity level and the activation energy associated with the DBT behavior (i.e., with the mobility of dislocations) of low purity tungsten is higher than that of high purity tungsten. Another example is provided by the interstitial elements in tantalum where it has been experimentally shown that the dissolved oxygen, nitrogen or air can increase the hardness and tensile strength of tantalum and decrease the elongation to failure [97, 98]. However, some impurities can instead

decrease the strength of tungsten, thus increasing the ductility and decreasing the DBTT. The typical example is tungsten- rhenium alloys [99].

According to the classical theory of dislocations [100, 101] which is based on the theory of elasticity and continuum mechanics, the solute or impurity atoms will almost always harden the matrix material by retarding or pinning the dislocations surrounded by the solute atmospheres. This effect is due to the elastic distortions introduced by the size mismatch between the impurity atoms and the host atoms, no matter whether the solute atoms sit in the interstitial or substitutional sites. This elegant theory has been successfully used to interpret many experimental results such as the upper and lower yield point phenomena that exist in the plastic deformation of many metals and alloys [101]. However, due to the limitations of the theory of linear elasticity, it fails in modeling the dislocation core structure which is highly non-linear and probably more important in determining the dislocation mobility. So the interactions between impurities and dislocations can only be understood through elastic strain field between them which requires that impurity atoms must be far away enough from the dislocation core. It is also impossible for this theory to deal with the effect of chemical bonding from electronic level, which, according to Gilman [90], is more fundamental and important to understand the mechanical behavior of various materials. Since the impurities tend to segregate into the vicinity of dislocation core and will more or less change the core structure, some efforts have been undertaken to work on the impurity effect on dislocation core from first-principles calculations instead of classical dislocation theory. For example, Romaner [102] and co-workers investigated the effect of rhenium on the core of screw dislocations of tungsten and found that rhenium can induce a

transition from a symmetric to an asymmetric core and a reduction in Peierls stress, thus increasing the number of possible slip systems and decreasing the yield stress.

1.5.2.6 Dislocation related parameters

Several parameters, either intrinsic or extrinsic, are intimately related to the properties of dislocations; or they are used to describe the dislocation properties. Such parameters at least qualitatively correlate with the ductility of materials. When we compare such properties as ductility of different materials, it is not feasible to make the comparison under all the possible conditions defined by the tremendous number of microstructures possessed by each material. However, we can exclusively compare the parameters that are intrinsic to the material or those of prevailing microstructures such as dislocations. It is also recommended that the parameters are measurable either through experiments or theoretical calculations. These parameters are but not limited to cohesive energy, lattice constant, crystal structure, crystal elastic constants, shear modulus, bulk modulus, ideal shear strength, shear strength, dislocation mobility, number of slip systems, number of reaction path, and so on. All these parameters are closely related to each other and are important for the mechanical properties of especially crystalline materials.

The cohesive energy and lattice constants relate closely to the elastic constants, the elastic modulus such as the shear modulus, bulk modulus, and strength such as shear and tensile strength. We can understand this relationship using a simple model. Assume the interatomic potentials of materials are described by the formula $\phi(r) = \phi_0 f(r_0 / r)$ with only two parameters, viz. the depth of the potential well E_0 and the equilibrium distance r_0. The function $f(r_0 / r)$ reaches minimum when the interatomic distance $r = r_0$, i.e. $\phi'(r_0) = 0$. One typical and well-known example of this type of interatomic potential is the

Lenard-Jones potential. For simplicity, we consider a simple cubic unit cell with interactions only coming from the first nearest neighbors. In this case the energy of the unit cell is $U(r) = E_0 f(a_0 / r)$, where E_0 is the cohesive energy, a_0 the lattice constant. The bulk modulus of the material is defined as $B = -dp/(dV/V)$, here V is the volume of the unit cell and equals r^3 in this case. Since $dU = pdV$, we have

$$B = -V\frac{d^2U}{dV^2}\Big|_{r=a_0} = -V\frac{d^2U}{dr^2}\left(\frac{dr}{dV}\right)^2\Big|_{r=a_0} . \tag{1.6}$$

After substitution of U, the bulk modulus is finally expressed as

$$B = \frac{E_0}{9a_0^3}\left(-f''(1)\right) . \tag{1.7}$$

From equation (1.7) we can see that the bulk modulus of the material is proportional to the cohesive energy and the inverse of the lattice constant cube. Although this model is too simple to be used for quantitative evaluation, it still gives us some qualitative sense of physical understanding. In fact, we can simply derive equation (1.7) with the term $\left(-f''(1)/9\right)$ replaced by a coefficient, merely according to the unit of elastic modulus and strength which is the unit of energy divided by that of volume. We can also perceive the elastic modulus as the increase of energy density caused by a unit of elastic strain, and the strength as the increase of energy density needed to make materials fail. From Figure 1-1, we can see that the bulk moduli of both group VA and VIA transition metals show quite good linear relationship with the ratio of cohesive energy to the cube of lattice constant. This is probably because when we choose the materials to plot, we choose those that behave similarly. For example those elements that sit in the same column group of the periodic table, have the same crystal structure. Most importantly, they can probably be modeled using similar interatomic potentials. Nevertheless, it is implausible to use this

model to understand the mechanical properties of every material, since materials properties are influenced by many other factors as well.

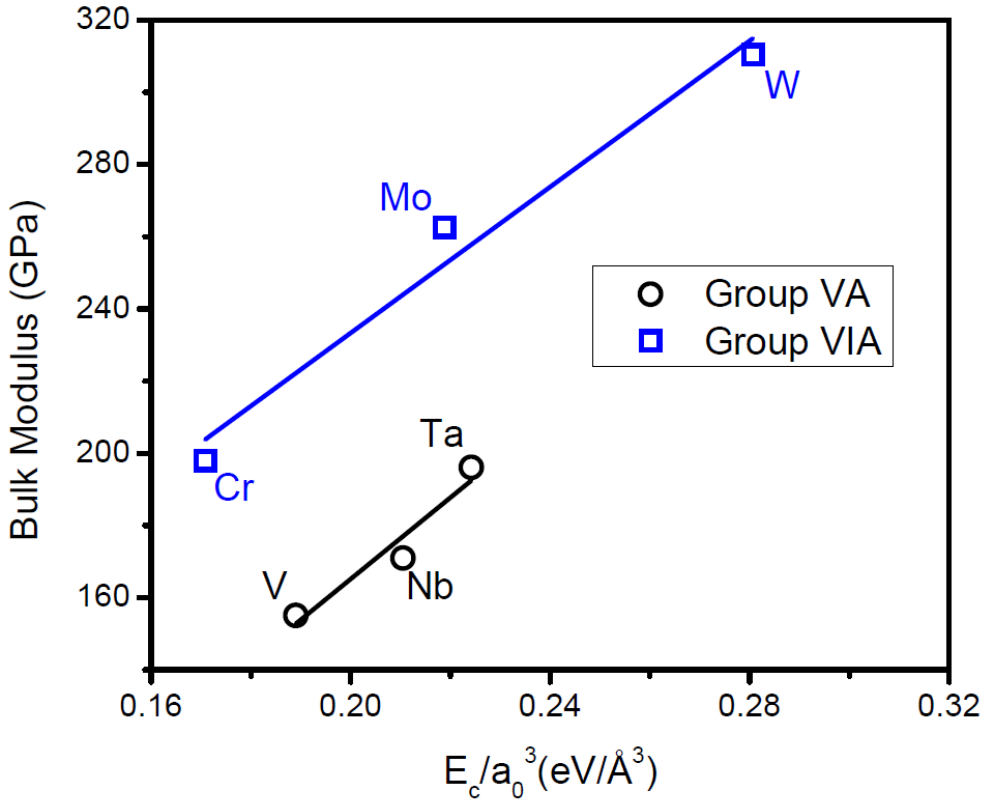

Figure 1-1: The approximate linear relationship between bulk modulus and the ratio of cohesive energy to lattice constant cube for group VA and VIA transition metals. The data is from [103].

Another interesting thing is ductility. If the materials can be modeled using the aforementioned formula $U(r) = E_0 f(a_0 / r)$, and if we loosely define strain as $\varepsilon = \ln(r / a_0)$, then the formula can be rewritten as $U(\varepsilon) = E_0 f(e^{-\varepsilon})$. This means that the internal energy of the system is actually a function of the strain, and the ductility of the

material is only determined by the function $f(x)$, and has nothing to do with cohesive energy.

The strength of a crystalline solid is closely dependent on the dislocation mobility and thus the ability of plastic deformation and ductility. Cubic crystals have only three independent elastic constants C_{11}, C_{12} and C_{44} based on contracted notation [90]. For a single crystal with cubic symmetry, the common relationships between elastic constants and elastic modulus are as follows [90].

Bulk modulus:

$$B = \frac{C_{11} + 2C_{12}}{3} . \tag{1.8}$$

Anisotropy coefficient:

$$A = \frac{2C_{44}}{C_{11} - C_{12}} . \tag{1.9}$$

Shear modulus for various planes in various directions:

$$\begin{aligned} G_{\{100\}<***>} &= C_{44} \\ G_{\{111\}<***>} &= \frac{3C_{44}(C_{11} - C_{12})}{4C_{44} + C_{11} - C_{12}} \\ G_{\{110\}<110>} &= \frac{C_{11} - C_{12}}{2} \\ G_{\{110\}<001>} &= C_{44} \end{aligned} . \tag{1.10}$$

Shear modulus is the resistance of a material to resist elastic shape change, and is closely related to the shear strength and dislocation mobility. Qualitatively speaking, high shear modulus and shear strength usually means low dislocation mobility and ductility, given the comparison is made for materials with the same crystal structure.

Probably dislocation mobility is the most important parameter related to the plastic deformation ability and ductility of materials. It is defined as [90]

$$\mu(\tau) = \frac{dv}{bd\tau}, \tag{1.11}$$

where v is the dislocation velocity, b the Burgers vector of the dislocation and τ the applied shear stress. Dislocations with higher mobility can attain higher speed with the same stress level or need less stress to attain a prescribed speed. Dislocation mobility is hard to measure directly, but it correlates with many other parameters such as generalized stacking fault (GSF) energy or γ-surface [104, 105], Peierls-Nabarro (PN) stress and energy barrier [106, 107] that are measurable at least through theoretical calculations. PN theory is too simplistic and is often inconsistent with experimental observations [90], most probably due to the oversimplified interatomic force model and to the fact that it does not take into consideration of the specific crystal structure. However, when combined with atomistic simulations and first-principles calculations, the principlal ideas and concepts of this theory are still very useful and indispensable to investigate the dislocation properties. Some efforts [108-115] have been embarked on to investigate the dislocation mobility by calculating the PN stress and energy barrier as a dislocation core moves along different prescribed paths such as those of straight dislocation movement and kink formation. Those calculated parameters can then be used to estimate the dislocation mobility and make comparisons between various materials.

The concept of GSF is an extended version of stacking fault which can be created by breaking the normal stacking sequence of the periodic arrangements within a crystal along a specific crystallographic direction. Different from a regular stacking fault whose atomic planes must be those of the stacking planes of the perfect crystal, the positions of GSF plane can be anywhere. They are generated by cutting a crystal along a specific crystal plane and then moving one part of the crystal with respect to the other by a displacement

vector **t** that is parallel to the cutting plane [104, 105, 116, 117]. The consequence in terms of energetics of this movement is the increase of the crystal energy. The energy difference per unit area between the displaced crystal and the perfect crystal is defined as the GSF energy $\gamma(\mathbf{t})$. This energy is actually a two dimensional function of the displacement vector and generates a so-called γ-surface in a prescribed three dimensional coordinate system.

The concept of GSF is essentially significant for the investigation of the structure and properties of dislocations and thus the plastic deformation ability of materials. The negative gradient of the GSF energy represents the restoring stress acting across the cutting plane and can be qualitatively used to analyze the spreading of dislocation cores [105]. For BCC metals, the dominant line defect responsible for plastic deformation is screw dislocation with Burgers vector along <111> directions. So the displacement vector is usually chosen to be along one of the <111> directions when calculating the GSF energy. It is based on such calculations where it is proposed that for BCC metals along {110} cutting plane, the screw dislocation core prefers to be symmetric or non-degenerate if $\gamma(b/3)>2\gamma(b/6)$, while asymmetric or degenerate otherwise [105]. The GSF energy can also be used to calculate the shear modulus which is the gradient of GSF energy for an infinitesimal displacement vector and the ideal shear strength which is the maximum of the gradient of the GSF energy. In addition, the peak value of the GSF energy is controlled by the cohesive energy [105]. Therefore the qualitative link between plastic deformation ability and GSF energy is that a low GSF energy means low energy barrier in shear deformation and thus it should favor plastic deformation and high ductility.

The last but not the least important parameter is the number of possible reaction paths. Its role is as important but might not be as prominent as that of the aforementioned

dislocation related parameters. Theoretically speaking, we can make the material deform in any way we want by controlling the movement of individual atoms. However, there are so many atoms and so many degrees of freedom (DOF), that it is impossible to control all or even part of them. So the materials can respond to the external loading through innumerable choices or reaction paths. For solid materials, different reaction path has different energy barrier which need to be surmounted before the deformation occur. Qualitatively speaking, the higher the energy barrier, the more difficult it is to activate the deformation process. Therefore, in spite of so many reaction paths, materials deform only through those with considerably low energy barrier. In other words, the energetically possible reaction paths may be favored to contribute to the plastic deformation of the material. For example, at relatively low homologous temperatures, the plastic deformation of crystals proceeds through dislocation activities instead of the ideal shear process because the energy barrier of the former is much lower than that of the latter. Screw dislocation in BCC metals usually moves through the double kink mechanism rather than as a straight line because of the same reason. Usually, the energy barrier of straight dislocation movement is higher than that of curved dislocation. It is also true that energetically it is more difficult to nucleate a dislocation within a perfect crystal than move an existing dislocation. Apparently, for a given crystal, a sessile dislocation has higher energy barrier to dislocation motion than a glissile dislocation. The possible reaction paths also depend on the loading conditions which make it impossible for some reaction paths to occur even their energy barriers are much lower than those of actually more favored paths. One typical example is that compressive loading does not favor such deformation mode as necking or rupture which often happens for ductile materials under tension.

The deformation ability of materials increases with the number of possible reaction paths. For example, the plastic deformation ability of crystalline metals is determined by the number of possible slip systems that can be easily activated by stress. This is the essential reason why most hexagonal close packed (HCP) metals are less ductile than many FCC and BCC metals, since the former have fewer active slip systems than the latter. There are two principal ways to increase the strength of materials. One is to increase the energy barriers of the possible reaction paths, by for example adding impurities into the lattice and thus impeding the dislocation movement. The other way is to reduce the number of DOF and thus the number of possible reaction paths with low energy barrier, by, for example, decreasing the grain or sample size. In other words, one has introduced the well-known size effect [118-122]. In essence, the two general methodologies used to design and fabricate materials, i.e., the top-down and the bottom-up methods are to generate the microstructures that favor the beneficial reaction paths and suppress the detrimental ones. For ductile materials, plastic reaction paths are favorable, such as dislocation movement, partial dislocation movement accompanied with the formation of stacking fault, and twinning. For brittle materials, brittle reaction paths are favorable, such as crack nucleation and propagation.

Although not stated explicitly and proved rigorously, it is presumed that the aforementioned dislocation related parameters are consistent to the understanding and prediction of the plastic deformation ability or even ductility of materials. More specifically, researchers from different groups usually concentrate on different aspects of the mechanical behavior of materials. For example, some of them focus on elastic constants or moduli, some of them on PN model, yet some others on dislocation mobility

and dislocation dynamics, and so on. This is partly because the experimental or calculation methodologies they adopt have their own limitations. For example, first-principles calculations are limited by their incapability in dealing with large scale simulations that involve a large number of atoms, such as that of double kink mechanism. So they can only be used to calculate the elastic moduli, the Peierls energy barrier and stress based on the simple PN model. Atomistic simulations can deal with larger scale problems such as double-kink mechanism, deformation mechanism of nanocrystalline metals [123-126]. But they still cannot handle mesoscale problems which could otherwise be dealt with by dislocation dynamics simulations. However, in spite of so many limitations, they can still be employed to answer the same question: why a material is ductile or brittle, weak or strong based on the presumption that those parameters are closely related with each other and can be put into a unified picture.

1.5.2.7 Dislocation related parameters of tantalum and tungsten

Based on the above understanding, it is necessary to list all the dislocation related parameters of tantalum and tungsten to show their ability of plastic deformation. Table 1-2 gives the elastic constants and moduli of BCC tantalum and tungsten from both experiments and theoretical calculations. From this table we can see that all the listed elastic moduli of tungsten are higher than those of tantalum despite the small discrepancies from different reports. The average shear modulus of tungsten is more than double that of tantalum, indicating that plastic deformation is more difficult to occur in tungsten.

Elastic constants and moduli alone are not enough to show the plastic deformation ability and sometimes the inconsistency between them and other parameters does exist. For example the shear modulus of aluminum is lower than that of copper, but it has higher ideal

Table 1-2: Elastic constants and moduli of tantalum and tungsten. The units are GPa, except for the anisotropy factor A and Poisson's ratio ν. The elastic moduli are calculated based on Voigt average [100].

Metal	C_{11}	C_{12}	C_{44}	B	G	E	A	ν	Reference
Ta	267	161	82.5	196	70.7	189	1.56	0.339	[100]
	257	163	71	194	61.4	167	1.51	0.357	[127]
	265	159	74	194	65.6	177	1.40	0.348	[128]
	291	162	84	205	76.2	203	1.30	0.334	[129]
	266	161	83	196	70.8	190	1.58	0.339	[130]
	266	161	82	196	70.4	189	1.56	0.340	[105]
	261	157	81.8	192	69.9	187	1.57	0.337	[131]
W	521	201	160	308	160	409	1.00	0.278	[100]
	500	205	130	303	137	357	0.88	0.304	[127]
	553	207	178	322	176	447	1.03	0.269	[129]
	523	204	161	310	160	410	1.01	0.280	[130]
	523	205	161	311	160	410	1.01	0.280	[131]
	529	209	162	316	161	413	1.01	0.282	[132]
	522	204	161	310	160	410	1.01	0.280	[105]

Table 1-3: Some of the dislocation related parameters for tantalum and tungsten

	Tantalum		Tungsten	
$\gamma_{\{110\}<111>}$ (eV/Å^2)	0.052	[133]	0.116	[102]
			0.101	[109]
	0.059	[134]	0.137	[134]
$\gamma_{\{211\}<111>}$ (eV/Å^2)	0.069	[134]	0.143	[134]
	0.059	[133]		
Peierls Energy Barrier (eV/b)	0.07	[135]		
	0.038	[136]		
Peierls Stress (GPa)	1.8	[135]	2.88	[102]
			4.5	[109, 137]
Kink Formation Energy (eV)	0.67-1.84	[138]		
	1.1	[136]		

shear strength which is probably more important to indicate the plastic deformation ability [139]. So it is also necessary to list such parameters as the Peierls energy barrier, Peierls stress and kink formation energy etc. which are more directly related to the dislocation mobility. As shown in Table 1-3, which also gives the maximum values of the GSF energy

of both {110} and {211} plane shearing along <111> direction, the value of every parameter of tantalum is lower than that of its counterpart in tungsten whenever the comparison is possible. This again indicates that the plastic deformation ability of tantalum is much higher than that of tungsten. It therefore at least partly explains why the ductility of tantalum is higher than that of tungsten. Although the results are obtained through different methods and may not be accurate and there are some discrepancies between those values, it is ample to make qualitative comparisons. In addition, the large difference between various parameters between tantalum and tungsten indicates that the plastic deformation ability of tantalum should be much higher than that of tungsten, since the discrepancies of the data for the individual metal always fail to eliminate the significant difference between the two different metals.

1.5.2.8 Comments on role of dislocations in plastic deformation of materials

The investigations on the role of dislocations in plastic deformation and ductility of materials concentrate on the dislocation properties per se. This is true even for the applications of new computational techniques such as dislocation dynamics, molecular dynamics and DFT on the calculations of dislocation properties. Many researchers actually have tried to relate the dislocation properties to the plastic deformation properties, such as strain hardening [83, 84, 140-142], strain rate hardening [87-89], plastic anisotropy [105, 109, 143, 144], and so on. On the other hand, they have not taken into much consideration of the ductility of materials despite the conventional wisdom that low dislocation mobility usually points to low ductility. Therefore, the studies on dislocations have the same shortcomings as those on GBs, in that they have only considered one specific metal or one specific group of metals. Few comparisons have been made between different metals. This

might have been due to the fact that it has been presumed that materials with similar crystalline structures possess similar plastic deformation properties. It might have also been presumed that GB separation or intragranular cleavage is not a serious issue during the deformation process dominated by dislocations, because when investigators try to study the specific properties of materials, they usually single out one factor for examination and fix other factors to avoid coupling effects which may largely complicate the problem. This is probably why people chose single crystalline tungsten when investigating the role of dislocations in the DBT behavior [24], since the usually weak GB of tungsten is not a problem anymore in the case of single crystals of tungsten. Although some people have considered the interactions between dislocations and GBs [145, 146], they have usually concentrated on the influence of GBs on dislocations, such as acting as barrier to the dislocation motion and thus strengthening the material, and disregard the influence of dislocations on GBs, assuming that GB is not a serious issue for the understanding of the results. By doing this, it is possible to obtain consistent results on the one hand, but it is not appropriate to come to a complete understanding and sometimes it can even lead to controversial issues on the other. The root cause for this is that other factors do have influence on the investigated properties.

1.5.3 Competition between GB separation and dislocation activity

Since both GBs and dislocations are important to the understanding of plastic deformation and ductility of polycrystalline pure metals, in many cases they cannot be separated and considered on an individual basis to give a consistent and complete picture of the physical processes involved. Therefore, it is highly necessary to consider the competition between them when addressing the plastic deformation of polycrystalline

metals. In this section, the GB separation process also includes the cleavage of grains, based on the understanding that any cutting plane inside a single crystal can be considered as the creation of a special GB with zero misorientation and zero GB energy. In what follows, several criteria are proposed to characterize the ductility of materials based on different competition mechanisms.

1.5.3.1 Ratios of shear modulus to bulk and to Young's modulus

The deformation of materials can be divided into two modes: dilatational and shear deformation. The former refers to change in volume; the latter refers to change in shape. The parameter that characterizes the resistance to elastic dilatational deformation is the bulk modulus; the parameter that depicts the resistance to elastic shape change is the shear modulus. The ductility of a material is determined by the competition between the dilatational facture deformation and the plastic shear deformation. Pure plastic shear deformation includes debonding and subsequent rebonding processes and it actually will not result in failure. As a matter of fact, failure is always a result of dilatational deformation accompanied with the debonding process only. Based on this understanding, it is reasonable to use the ratio of shear modulus to bulk modulus G/B to qualitatively compare the ductility of different materials [147-149]. Materials with low G/B behave more like liquid and are ductile, whereas those with high G/B behave more like solid and are brittle. Similarly, we can also use the ratio of shear modulus to Young's modulus G/E to perform the comparison. In fact, this ratio can not only be used to evaluate the intrinsic plasticity of crystalline metals, but it can also be used to evaluate the fracture toughness of metallic glasses [150].

1.5.3.2 Poisson's ratio and anisotropy

Poisson' ratio is defined as the ratio of the induced transverse strain to the longitudinal strain during elastic deformation. For isotropic materials which only possess two independent elastic moduli, the bulk modulus B, shear modulus G and the Poisson's ratio ν are associated with each other by the following equation

$$\frac{G}{B}=\frac{3(1-2\nu)}{2(1+\nu)}. \tag{1.12}$$

From this equation, we can infer that $-1\le\nu\le 0.5$, since $0\le G/B\le\infty$. In this regard, Poisson's ratio also measures the resistance of a material to volume change against the resistance to shape change [149]. According to the qualitative relationship between ductility and the ratio G/B, it is reasonable to suggest that Poisson's ratio is also related to the ductility of at least isotropic materials. In fact, it has been proved that Poisson's ratio is related to the malleability of materials in a limited temperature range, and provides a good criterion for evaluation of ductility and brittleness of crystalline and even amorphous metals [149, 151]. For anisotropic materials, extreme values of Poisson's ratio in single crystals are also found to be strongly correlated with elastic anisotropy [152], indicating that it could also be related to the ductility of materials. For isotropic materials, the specific reaction path is determined by the loading conditions, whereas for anisotropic materials, the effect of loading condition on plastic deformation will not be as straightforward and simple. Even not the most favored by loading conditions, the reaction path that has low energy barrier still get a chance to occur and to contribute to the overall plasticity. Therefore, the influence of anisotropy can be understood in such a manner that it may increase the number of possible ductile or brittle reaction paths and thus alter the

competition between the two kinds of paths, eventually resulting in changes of deformation mode or ductility.

1.5.3.3 Ratio of the ideal tensile strength to the shear strength

For a single crystal, the ideal tensile strength is the maximum stress achieved when separating the single crystal along a cutting plane and is the upper limit of the tensile strength of materials. Ideal shear strength is the maximum stress achieved when shearing the single crystal along a cutting plane and is the upper limit of shear strength of materials. Ideal tension deformation results in cleavage and brittle fracture, whereas ideal shear results in plastic deformation. So the ratio of the ideal tensile strength and the ideal shear strength $\sigma_{\max} / \tau_{\max}$ can be used as a criterion in the competition between ideal tension and shear processes. To use this criterion, it is presumed that whichever higher of the ideal tensile and shear strength values is the harder to reach. Thus, materials with high $\sigma_{\max} / \tau_{\max}$ have relatively higher ideal tensile strength and shear stress reaches the ideal shear strength first, resulting in ductile behavior. Otherwise, materials with low $\sigma_{\max} / \tau_{\max}$ have relatively higher ideal shear stress and tensile stress reaches the ideal tensile strength first, resulting in cleavage and brittle behavior. This understanding is not complete and rigorous, but the criterion based on which still provides quite a consistent comparison of ductility among different materials [81, 153].

1.5.3.4 Relative tensile stress and shear stress

It is worth noting that materials with high tensile/shear strength usually have high tensile/shear modulus. This means that, based on the theory of linear elasticity, the tensile/shear stress of materials with high tensile/shear strength ratio increases faster with tensile/shear strain than that of materials with low tensile/shear strength. Therefore, it is

difficult to determine which stress reaches the maximum value first. To resolve this issue, Kelly and co-workers [153] proposed that if the ratio of the largest tensile stress to the largest shear stress close to the crack tip is greater than that of the ideal cleavage stress to the ideal shear stress, a fully brittle facture occurs. Otherwise, the facture of the crystal is accompanied with plastic flow. The criterion can be expressed in yet another way. If the actual largest relative tensile stress is higher than the largest relative shear stress at the crack tip, the crystal breaks in a fully brittle manner. Otherwise, the facture process will exhibit plastic feature. Here the relative tensile stress is defined as the tensile stress divided by the ideal tensile stress, and the relative shear stress is defined as the shear stress divided by the ideal shear stress. This criterion actually tells which stress (tensile or shear) reaches the ideal strength value first, and also gives results quite consistent with that predicted by the ratio of the ideal tensile and shear stresses [81, 153].

1.5.3.5 Ratio of cleavage energy to unstable stacking energy

As we have mentioned before, a material may have many possible reaction paths to choose in response to external loading. However, only those with the lowest energy barrier are highly possible to dominate the deformation process. Therefore, it is necessary to set up a criterion to evaluate the ductility of the material in terms of the level of the energy barriers for a specific reaction path, be it dislocations, twinning, or stacking faults mechanism. Ideal tensile facture generates two FSs, the energy of which is the cleavage energy $2\gamma_s$ and can be used as the energy barrier to the fracture process, where γ_s is the specific surface energy (energy per unit surface area). The energy barrier corresponding to the ideal shear process is the unstable stacking fault energy γ_{us} [154], which is the maximum value of the aforementioned GSF energy when shearing in the Burgers vector

direction. The ratio of the cleavage energy to the unstable stacking fault energy $2\gamma_s / \gamma_{us}$, can be used to determine the competition between ideal cleavage and shear deformation. Materials with relatively high unstable stacking energy and thus low cleavage energy prefer cleavage and are thus brittle, and are ductile otherwise. It should be noted that ideal shear is not a realistic plastic reaction path and dislocation activities instead dominate the plastic deformation process. Therefore, it is not very appropriate to base the criterion on the competition between ideal shear and cleavage. But this does not fundamentally negate the validity of this criterion. Rice [154] investigated the dislocation nucleation from a crack-tip and found that the level of stress intensity factor required for dislocation nucleation is proportional to the square root of unstable stacking fault energy. Based on this observation, Rice proposed a similar criterion that uses the ratio of the surface energy to the unstable stacking energy γ_s / γ_{us}. This criterion is based on a crack-tip model inside a single crystal; however, it can be easily extended to the case when the crack-tip is along a GB by simply replacing the cleavage energy $2\gamma_s$ with the GB separation energy $2\gamma_{sep}$.

1.5.3.6 Rice-Thomson model

Rice and Thomson [155] investigated the competition between cleavage and blunting dislocation nucleation at the tip of an atomically sharp crack. They proposed that crystals with wide dislocation cores and small values of the parameter $\mu b / \gamma$ are ductile (μ is the shear modulus, b the magnitude of dislocation Burgers vector and γ the surface energy of the material), while crystals with narrow dislocation cores and large values of $\mu b / \gamma$ are brittle. This criterion is also set up in terms of energy barriers. But the difference between this criterion and the previous one is that the term μb in this criterion refers to the

energy barrier of dislocation nucleation from the crack-tip, whereas the term γ_{us} in the previous criterion refers to the energy barrier of ideal shear which actually is almost impossible to occur during the plastic deformation process. To extend the application of this model to the case where the crack is along a GB with and without segregated impurities, Rice and Thomson [31, 156] put forth another more general criterion. They suggested that the material is brittle if the cleavage energy or GB separation energy is less than that necessary to nucleate dislocation at the crack-tip; otherwise, the crack-tip will be blunted by dislocation emission, resulting in more or less ductile behavior.

1.5.3.7 Cohesive zone model and dislocation dynamics

The criterion used in the Rice-Thomson model is highly dependent on the predetermined reaction paths and may not be valid if the reaction paths have been changed [157]. In other words, the Rice-Thomson model has only considered the competition between cleavage and dislocation activities at crack-tips, but it has not considered the competition among various reaction paths of cleavage or dislocation events. This can be important, since the crack does not necessarily propagate along the crack plane and may not even be smooth and flat [158-160], and the slip plane of dislocations might also change, only if they are energetically favorable. More importantly, the Rice-Thomson approach was proposed based on theoretical analysis at crack-tips of materials and is more or less ideal or even impractical. As a nice try, Zeng and Hartmaier [161] proposed a more general approach when investigating the size effects on fracture toughness of tungsten. They applied the cohesive zone model in front of the crack tip to simulate the cleavage behavior, and put dislocation sources near the crack tip to simulate the dislocation nucleation and propagation using two dimensional dislocation dynamics. The merit of this approach is that

the reaction path and number of dislocations are not predetermined. This model can be easily extended to polycrystalline materials if the GBs are modeled with cohesive zone and grains are modeled using dislocation dynamics.

1.5.3.8 Ductility of tantalum and tungsten in terms of a competition mechanism

Table 1-4: Parameters for tantalum and tungsten

	Tantalum		Tungsten	
G/B	0.36	[100]	0.52	[100]
	0.26-0.35	[90]	0.46-0.55	[90]
σ_{max}/τ_{max}			5.04	[153]
	1.89*	[127]	1.62*	[127, 162]
γ_s/γ_{us}	2.6	[154]	1.1	[154]
	3.7	[154]	1.6	[154]
$\mu b/\gamma$	6.2	[154]	26	[155]
* The ideal tensile is along <100> direction, the ideal shear is along <110> direction on {111} plane.				

We can use the criteria based on the competition mechanism to compare the ductility between pure tantalum and pure tungsten, as shown in Table 1-4. From the data listed here we can see that all the relevant parameters indicate that the ductility of tantalum is higher than that of tungsten.

1.5.3.9 Comments on the competition mechanism

The aforementioned criteria can be used to evaluate the intrinsic ductility of various materials. Such evaluation requires that materials of interest have similar microstructures such as grain size, grain shape, and density of dislocations and so on. In other words, these criteria failed to account for the extrinsic factors of the material due to the predetermined paths. In fact, the dislocations nucleated at the crack-tip may choose different ways to slip, and due to the complicated stress state at the crack-tip, many other plastic deformation

mechanism such as deformation twinning [163] or even phase transformation [164] might also occur. For brittle solids, the crack may propagate along the predetermined path or through other paths. With the evolution of the deformation and crack propagation processes, the previous ongoing reaction paths involving both dislocations and cracks may change to other energetically easier paths. For example, the crack-tip might be blunted through nucleated dislocations in the beginning. However, when the plastic deformation at the crack-tip is saturated, the crack can still propagate in a brittle-like manner. For polycrystalline materials, during the deformation, the GBs will hinder the dislocation movement which conversely could also change the structure of GBs, that of grain interior, and the roughness of FS. All of these changes will in turn change the competition behavior and influence the final ductility. So the ductility of materials is very difficult to evaluate although theoretically it can be done using many methods such as classical or even first-principles calculations, MD simulations and multiple scale simulations without considering the computational capabilities of computers.

1.6 Comments on the existing work.

One common feature of the literature efforts is that they have concentrated only a single aspect of the problem, while disregarded other important aspects consciously or unconsciously. As a consequence, they have arrived at incomplete and not-so-well substantiated conclusions. The investigations on the role of GBs have only concentrated on the effect of impurities on GB separation energy and answered the question why commercial purity polycrystalline tungsten is more brittle than pure (single crystal) tungsten. However, it is much more difficult for such efforts to address the question why tantalum is more ductile than tungsten. The investigations on the role of dislocations have

concentrated on the relationship between the strength and the mobility of dislocations. Such an approach can actually offer reasonable explanations of the source of ductility. However, they fail to answer the question why some metals with high dislocation mobility still possess lower ductility than those with relatively low dislocation mobility. Typical examples are provided by alkali metals which probably have the lowest yield strength and thus the highest dislocation mobility, but not the highest ductility of metallic materials. Even the work on the competition between ductile and brittle deformation mechanisms is too simplistic to give quantitative assessment of ductility of various materials with various microstructures.

Notwithstanding the lack of a complete or rigorous assessment of ductility, we have ample and tangible evidence from both experimental and theoretical studies to support the notion that pure tantalum is much more ductile than pure tungsten. We can even conclude that the distinction of ductility between commercial purity tantalum and tungsten comes from that between pure tantalum and tungsten. This is because the residual ductility of tantalum is still better than that of tungsten, even if we presume that impurities have similar effect on both metals given the same impurity level. However, despite the validity of this presumption in many cases, we have to admit that at least some impurity elements are selective about matrix materials, and the effect of those elements could dramatically change from one matrix to another. Similarly, some matrix materials could also be selective about the impurity elements, which can be seen from the variation of impurities' solubility in various matrix materials. As such, the conclusion drawn above is at least incomplete. Here we see a pressing need for more rigorous and thorough investigations to reach a more consistent and holistic understanding.

1.7 What we will do in this work.

In this thesis, based on the literature work, we have recognized the fact that pure tantalum is more ductile than pure tungsten. This fact can be understood in terms of the competition between GB separation and dislocation activities. We will concentrate on the effects of impurities on the properties of GBs and dislocations. The segregation energies of various impurities in tantalum and tungsten will be evaluated using first principles calculations. First, we use density functional theory (DFT) to systematically calculate the separation energies of symmetric tilt Σ3(111) GBs of both tungsten and tantalum, with and without interstitial impurity atoms (H, B, C, N, O, F, Al, Si, P, S, Cl, and Fe). The effect of sulfur concentration on GB separation energy is also investigated. Second, we systematically calculate the GSF energy and Peierls energy of the screw dislocation of tantalum and tungsten, with and without interstitial impurities (B, C, O, and S). Last, we calculate the segregation energy of impurities (H, B, C, N, O, F, Al, Si, P, S, Cl, and Fe) inside the perfect crystal interior, at the GBs, or at the dislocation cores. This is because such segregation energies essentially determine the final statistical distribution of impurities inside the matrix, which in turn eventually influences the properties of GBs and dislocations. Based on these calculations and those on pure tantalum and tungsten in the literature, we will attempt to make a systematic and complete comparison of ductility between commercial purity tantalum and tungsten of similar microstructures. As to why pure tantalum are much more ductile than pure tungsten is another important topic which requires more efforts of extensive research, and, if unnecessary, will not be discussed in detail in this thesis. We hope this work will shed light on the understanding of the failure and toughening mechanism of commercial purity metals and serve as design guidelines to

improve the working performance of refractory metals for applications especially in harsh conditions.

1.8 The organization of this thesis.

In this chapter, we have given a meticulous, comprehensive and critical review of the understanding of the ductility and the various factors that influence ductility through three different ways. Since we are using DFT to perform the calculations, a brief introduction to the theoretical background of DFT and the related computational techniques will be given in Chapter 2 for the sake of the integrity of this thesis. In Chapter 3, we will present the first-principles calculation work on the effect of various impurities on the GB separation energies of tantalum and tungsten. We will also try to answer the question why commercial purity tantalum is more ductile than tungsten in terms of the role of GBs. In Chapter 4, we will present the first principles calculations on the effects of several impurities on the Peierls energy of screw dislocations in tantalum and tungsten, and will try to address the problem of ductility from the role of dislocations. In Chapter 5, we will combine the results of Chapter 3 and Chapter 4 and attempt to provide a concerted solution to the problem. Some fundamental discussions about the nature of strength, ductility and toughness will also be given in this chapter. Then in Chapter 6, we will summarize and draw some significant conclusions from our work. We will discuss the future work in the last chapter.

CHAPTER 2: DENSITY FUNCTIONAL THEORY- A BRIEF INTRODUCTION

As we know, the principles of quantum mechanics can be described in three equivalent but different ways: Schrödinger and Dirac's wave mechanics, Heisenberg's matrix mechanics, and Feynman's path integral formulation based on the principle of least action. Density functional theory (DFT) can also be perceived as yet another equivalent formulation of quantum mechanics, and has been widely used in physics, chemistry, materials science, and so on [165, 166]. The emergence of DFT resulted from the difficulties of applying Schrödinger equation in the calculation of material properties. The principle or the brilliant idea of DFT will be introduced in the following from this perspective without considering the technical details which can be found in many theoretical books and articles [167-176].

2.1 The Schrödinger equation

We start from the time independent Schrödinger equation shown as follows [177]

$$\begin{aligned} &\hat{H}\psi\left(\vec{r}_1,\vec{r}_2...\vec{r}_N\right)=E\psi\left(\vec{r}_1,\vec{r}_2...\vec{r}_N\right) \\ &\hat{H}=-\frac{\hbar^2}{2m}\sum_{i=1}^{N}\nabla_i^{\,2}+\sum_{i=1}^{N}v\left(\vec{r}_i\right)+\sum_{i=1}^{N}\sum_{j<i}U\left(\vec{r}_i,\vec{r}_j\right) \\ &\nabla_i^{\,2}=\frac{\partial^2}{\partial x_i^{\,2}}+\frac{\partial^2}{\partial y_i^{\,2}}+\frac{\partial^2}{\partial z_i^{\,2}}, \end{aligned} \tag{2.1}$$

where $\hat{H}$ is the Hamiltonian operator, ψ the time-independent wave function, E the total energy of the system, N the number of electrons in the system, $\vec{r}_i=\left(x_i,y_i,z_i\right)$ the coordinates of the ith electron, $v\left(\vec{r}\right)$ the external potential, $U\left(r_i,r_j\right)$ the electron-electron

interaction. The key step to solve quantum mechanical problems is to obtain the wave function by solving the Schrödinger equation given the potential and electron-electron interaction energy, since all the properties of the system are stored in the wave function, and can be obtained through the application of their respective operators on the wave function, as shown in equation (2.2).

$$\langle o \rangle = \left\langle \psi \middle| \hat{O} \middle| \psi \right\rangle = \int \psi^* \hat{O} \psi d^3\vec{r}_1 d^3\vec{r}_2 \cdots d^3\vec{r}_N, \qquad (2.2)$$

where $\hat{O}$ is the operator corresponding to the observable physical property of o. For example, the operator corresponding to the total energy E of the system is Hamiltonian $\hat{H}$. Theoretically speaking, the Schrödinger equation can be used to solve any quantum mechanical problems. However, this is feasible only when solving single electron problems, such as the hydrogen atom. It is also possible to solve multi-electron problems without considering the electron-electron interactions, which is a strong assumption. Other than that, however, when the interactions among the electrons are included, it is very difficult and oftentimes even impossible, to solve the Schrödinger equation analytically or even numerically. For such complex problems, therefore, practical approaches need to be developed.

2.2 From the wave function to the electron density

The multi-particle wave function uses the coordinates of all electrons as independent variables, and actually tries to keep the information associated with each electron. However, it is practically unnecessary and impossible to discriminate between different electrons. In view of this, a good approach is to obtain the statistical distribution of those electrons without considering their differences. This makes electron density a good choice. The electron density of a system is the sum of the spatial probability density

of all electrons in the system. Given N electrons and the corresponding wave function $\psi(r_1, r_2 \cdots r_N)$ in the system, the probability density of the ith electron is

$$n_i(\vec{r}) = \int \psi^*(\vec{r}_1, \cdot\cdot \vec{r}_{i-1}, \vec{r}_{i+1}, \cdot\cdot \vec{r}_N)\psi(\vec{r}_1, \cdot\cdot \vec{r}_{i-1}, \vec{r}_{i+1}, \cdot\cdot \vec{r}_N) d^3\vec{r}_1 \cdot\cdot d^3\vec{r}_{i-1} d^3\vec{r}_{i+1} \cdot\cdot d^3\vec{r}_N.$$

Since the wave function of electrons is antisymmetric, i.e.

$$\begin{aligned}
&\psi(\vec{r}_1, \vec{r}_2, \cdot\cdot \vec{r}_i \cdot\cdot \vec{r}_j \cdot\cdot \vec{r}_N) = -\psi(\vec{r}_1, \vec{r}_2, \cdot\cdot \vec{r}_j \cdot\cdot \vec{r}_i \cdot\cdot \vec{r}_N) \\
&\Rightarrow \psi^*(\vec{r}_1, \vec{r}_2, \cdot\cdot \vec{r}_i \cdot\cdot \vec{r}_j \cdot\cdot \vec{r}_N)\psi(\vec{r}_1, \vec{r}_2, \cdot\cdot \vec{r}_i \cdot\cdot \vec{r}_j \cdot\cdot \vec{r}_N) \\
&= \psi^*(\vec{r}_1, \vec{r}_2, \cdot\cdot \vec{r}_j \cdot\cdot \vec{r}_i \cdot\cdot \vec{r}_N)\psi(\vec{r}_1, \vec{r}_2, \cdot\cdot \vec{r}_j \cdot\cdot \vec{r}_i \cdot\cdot \vec{r}_N) \\
&\Rightarrow n_i(\vec{r}) = n_j(\vec{r}).
\end{aligned}$$

The electron density of a system is then

$$\begin{aligned}
n(\vec{r}) &= \sum_{i=1}^{N} n_i(\vec{r}) = N n_1(\vec{r}) \\
&= N \int \psi^*(\vec{r}, \vec{r}_2, \cdot\cdot \vec{r}_N)\psi(\vec{r}, \vec{r}_2, \cdot\cdot \vec{r}_N) d^3\vec{r}_2 d^3\vec{r}_3 ... d^3\vec{r}_N.
\end{aligned} \tag{2.3}$$

2.3 The Hohenberg-Kohn theorem

The significance of introducing electron density can be seen from the Hohenberg-Kohn theorem [177, 178] which states that the ground state wave function is a functional of the ground state electron density $n(\vec{r})$. This implies that all ground state observables are functionals of the electron density, since they are functionals of the wave function. In other words, the ground state electron density plays the role of ground state wave function and contains all the ground state information of the system. For example, the number of electrons N is a functional of the electron density.

$$N[n] = \int n(\vec{r}) d^3\vec{r}. \tag{2.4}$$

The total energy of the system is as follows

$$
\begin{aligned}
E &= \left\langle \psi \left| \hat{H} \right| \psi \right\rangle = T + V + U \\
T &= -\frac{\hbar^2}{2m} \sum_{i=1}^{N} \int \psi^* \nabla_i^{\,2} \psi \, d^3\vec{r}_1 d^3\vec{r}_2 \cdots d^3\vec{r}_N \\
V &= \sum_{i=1}^{N} \int \psi^* v(\vec{r}_i) \psi \, d^3\vec{r}_1 d^3\vec{r}_2 \cdots d^3\vec{r}_N \\
U &= \sum_{i=1}^{N} \int \psi^* \sum_{j<i} U(\vec{r}_i, \vec{r}_j) \psi \, d^3\vec{r}_1 d^3\vec{r}_2 \cdots d^3\vec{r}_N .
\end{aligned}
\tag{2.5}
$$

Here T is the kinetic energy of the electrons, V the potential energy, and U the energy due to interactions among electrons. We can easily show that V is an explicit functional of $n(\vec{r})$. In fact, because $v(\vec{r}_i)$ is real, we have

$$
\begin{aligned}
&\int \psi^* v(\vec{r}_i) \psi \, d^3\vec{r}_1 d^3\vec{r}_2 \cdots d^3\vec{r}_N \\
&= \int v(\vec{r}_i) \psi^* \psi \, d^3\vec{r}_1 d^3\vec{r}_2 \cdots d^3\vec{r}_N \\
&= \int v(\vec{r}_i) \, d^3\vec{r}_i \int \psi^* \psi \, d^3\vec{r}_1 d^3\vec{r}_2 \cdots d^3\vec{r}_{i-1} d^3\vec{r}_{i+1} \cdots d^3\vec{r}_N \\
&= \int v(\vec{r}_i) n_i(\vec{r}_i) d^3\vec{r}_i \\
&= \int v(\vec{r}) n_i(\vec{r}) d^3\vec{r} \\
&\Rightarrow V = \sum_{i=1}^{N} \int v(\vec{r}) n_i(\vec{r}) d^3\vec{r} \\
&\qquad = \int v(\vec{r}) \sum_{i=1}^{N} n_i(\vec{r}) d^3\vec{r} \\
&\qquad = \int v(\vec{r}) n(\vec{r}) d^3\vec{r} .
\end{aligned}
$$

Hohenberg and Kohn showed that T and U are also functionals of $n(\vec{r})$, the forms of which are independent of $v(\vec{r})$, albeit without explicit expressions, like V. Now it is enough to say that the total energy is a functional of the electron density, i.e.

$$
E[n] = T[n] + U[n] + \int v(\vec{r}) n(\vec{r}) d^3\vec{r} . \tag{2.6}
$$

If we know the exact expression of this functional, it is very easy to solve the ground state electron density by minimizing the functional through variational principle.

2.4 From discrete particles to continuum

Although the energy V of the electron system due to external potential can be explicitly expressed as a functional of the electron density $n(\vec{r})$, the energy U due to the interaction among electrons cannot be expressed explicitly and thus is difficult to calculate through $n(\vec{r})$. However, given $n(\vec{r})$, it is still possible to give an approximation to U by perceiving the discrete electrons as continuum charge. For a Coulomb system, the interaction between the ith and jth electron is

$$U(\vec{r}_i, \vec{r}_j) = \frac{e^2}{|\vec{r}_i - \vec{r}_i|},$$

where e is elementary charge. Then for a continuum charge, the charge of the infinitesimal volume near $\vec{r}$ is $dq = e \cdot n(\vec{r}) d^3\vec{r}$, and the interaction between charge at $\vec{r}$ and $\vec{r}'$ is

$$dU = \frac{dqdq'}{|\vec{r} - \vec{r}'|} = e^2 \frac{n(\vec{r}) d^3\vec{r} \cdot n(\vec{r}') d^3\vec{r}'}{|\vec{r} - \vec{r}'|}.$$

The energy due to the interaction is then

$$U_H[n] = \frac{e^2}{2} \int \frac{n(\vec{r}) n(\vec{r}')}{|\vec{r} - \vec{r}'|} d^3\vec{r} d^3\vec{r}'. \tag{2.7}$$

Here $U_H[n]$ is Hartree energy and clearly a functional of $n(\vec{r})$.

2.5 From multi particle to single particle

For a multiple electron system, the electrons are completely indistinguishable. This suggests that we can treat all the electrons as identical particles and assume that they experience the same potential $v_s(\vec{r})$. Then we can solve the universal one-electron Schrödinger equation as follows [177]

$$\left[-\frac{\hbar^2}{2m}\nabla^2 + v_s(\vec{r})\right]\varphi_i(\vec{r}) = \varepsilon_i\varphi_i(\vec{r}). \tag{2.8}$$

If we have the corresponding potential $v_s(\vec{r})$, we can solve the equation. If the system is in ground state, according to Pauli exclusion principle that different electrons must occupy different orbitals or wave functions, the electrons should occupy the N lowest energy states. The electron density is given by

$$n(\vec{r}) = \sum_{i=1}^{N} f_i \left|\varphi_i(\vec{r})\right|^2, \tag{2.9}$$

where f_i is the occupation number.

2.6 The Kohn-Sham equations

Based on the above thinking, Kohn and Sham [177, 179, 180] proposed a set of self-consistent equations to replace the multiple-particle Schrödinger equation.

$$\begin{aligned}
&\left[-\frac{\hbar^2}{2m}\nabla^2 + v_s(\vec{r})\right]\phi_i(\vec{r}) = \varepsilon_i\phi_i(\vec{r}) \\
&n(\vec{r}) = \sum_{i=1}^{N} f_i \left|\phi_i(\vec{r})\right|^2 \\
&E_0 = \sum_{i=1}^{N}\varepsilon_i + \frac{e^2}{2}\int\frac{n(\vec{r})n(\vec{r}')}{\left|\vec{r}-\vec{r}'\right|}d^3\vec{r}d^3\vec{r}' + \int v(\vec{r})n(\vec{r})\,d^3\vec{r} + E_{xc}[n]
\end{aligned} \tag{2.10}$$

,

where

$v_s(\vec{r}) = v(\vec{r}) + v_H(\vec{r}) + v_{xc}(\vec{r})$

$v(\vec{r})$: External potential

$v_H(\vec{r}) = e^2\int\frac{n(\vec{r}')}{\left|\vec{r}-\vec{r}'\right|}d^3\vec{r}'$: Hartree potential

$v_{xc}(\vec{r}) = \frac{\delta E_{xc}[n]}{\delta n(\vec{r})}$: Derivative of functional $E_{xc}[n]$

$E_{xc}[n]$: Exchange and correlation energy due to the e-e interactions.

The Kohn-Sham equations can be solved iteratively as follows

Step1: Give an trial electron density, $n(r)$
Step2: Determine $v_H(\vec{r})$ and $v_{xc}(\vec{r})$
Step3: Solve single particle Kohn-Sham Equation for $\phi_i(r)$
Step4: $n'(r) = \sum_i f_i |\phi_i(r)|^2$
Step5: If $n'(r) \neq n(r)$, $n(r) = n'(r)$, go to step 2
Step6: Calculate total energy and other relevant properties.

The advantage of the Kohn-Sham equations against the Schrödinger equation is that they can be easily implemented into computer programs and then solved numerically [181]. This makes some people perceive DFT as a numerical approximation to quantum mechanics. In fact, the development of DFT does not introduce any approximations and can be considered as an identical form of the Schrödinger equation until the exchange-correlation functional is given explicitly to make numerical calculations possible.

2.7 The exchange-correlation energy

The exchange-correlation energy E_{xc} is the term that stakes out the difference between Kohn-Sham scheme and others such as the Hatree scheme and Hatree-Fock scheme [177]. E_{xc} is often decomposed as $E_{xc} = E_x + E_c$, where E_x is the exchange energy due to the Pauli principle and the fact that electrons are not distinguishable, E_c is the correlation energy due to mutual avoidance of the interacting electrons or the dependence of electrons. To solve the Kohn-Sham equations, we need to know the form of $v_{xc}(\vec{r})$ or $E_{xc}[n]$. The approximations made to E_{xc} lead to many versions of DFT such as (i) the local density approximation (LDA) where $E_{xc}[n] = \int f(n(\vec{r}))d^3\vec{r}$ which only accounts for the local electron density and (ii) the generalized-gradient approximation

(GGA) [182, 183] where $E_{xc}[n] = \int f\left(n(\vec{r}), \nabla n(\vec{r})\right) d^3\vec{r}$ which also include the gradient of the electron density comparing with LDA.

2.8 Pseudopotentials.

When doing calculations, people always try to reduce as much computational cost as possible given the guaranteed accuracy. This is also possible for DFT calculations given the fact that the chemical bonding of materials are determined by the valence electrons and almost independent on core electrons. In other words, the density of the core-shell electrons does not change much with chemical environment, and can be treated universally, for example, using pseudopotentials [184-188] which are the same as the real potentials beyond a cutoff distance, but different otherwise. The pseudopotential and the pseudo wave functions of the core-shell electrons are chosen to match various physical and mathematical properties of the true ion core [189]. The most widely used pseudopotentials are the ultrasoft pseudopotentials (USPP) developed by Vanderbilt [188]. These potential (USPP) use low energy cutoff and thus are more computationally efficient.

2.9 Geometry optimization

When solving the Kohn-Sham equations we actually fix the external potentials by fixing the given positions of the atoms. However, the total energy of the system is not only dependent on the electron density but also on the position or geometry of atoms. It is almost impossible to give the positions right in the minimum energy state when setting up DFT calculations. And it is necessary to relax the geometry or run geometry optimization to reach the minimum total energy. The scheme is simple. At first, an initial geometry is given to run the DFT calculations; then the force acting on each atom is obtained by calculating the gradient of the total energy. The positions of the atoms are updated

according to the calculated forces using, for example, the conjugated-gradient method. These steps are repeated iteratively until the force acting on each atom is less than a critical value such as 0.01eV/Å [189].

CHAPTER 3: CALCULATIONS OF GB PROPERTIES

In this chapter, we use density functional theory (DFT) to calculate the GB separation energy of ∑3 (111) symmetric tilt grain boundary (STGB) with and without impurity atoms for tantalum and tungsten. We also use molecular dynamics (MD) method to calculate the GB separation energy of various clean GB structures and the temperature effect on clean ∑3 (111) STGB separation energy for tantalum and tungsten. The organization of this chapter is as follows. We give the atomic configurations for DFT and MD calculations in the first section of this chapter; then based on the Rice-Wang model, we developed the formulas to calculate GB energy, surface energy and GB separation energy from the output of DFT and MD calculations. The results are described in the third section. In the fourth section, we talk about why and how impurity atoms influence the GB separation processes and we try to separate the effect into chemical effect and atomic size or mechanical effect. Finally, we discuss the results and point out the necessity of investigating the effect of impurities on the dislocation properties.

3.1 Calculation set up

3.1.1 Atomic configurations

According to the Rice-Wang model, we use three different kinds of atomic configurations to calculate the GB energy, free surface (FS) energy and GB separation energy with and without impurities. The details on how to calculate them will be discussed

in Section 3.2. In present section, we only give a description to these configurations used in DFT calculations.

Figure 3-1 gives the atomic configuration of a pure single crystal. It is used as a reference or control sample to calculate the GB energy and the FS energy. An orthorhombic super cell is used to model the system and the dimension of the super cell are $2\sqrt{2}a_0$, $\sqrt{6}a_0$, and $4\sqrt{3}a_0$ respectively along x, y, and z directions, where the lattice constant a_0 is 3.30Å for tantalum and 3.18Å for tungsten. The crystallographic directions of the super cell are shown in the figure. The super cell consists of 96 atoms and periodic boundary conditions are applied in the x, y, and z directions.

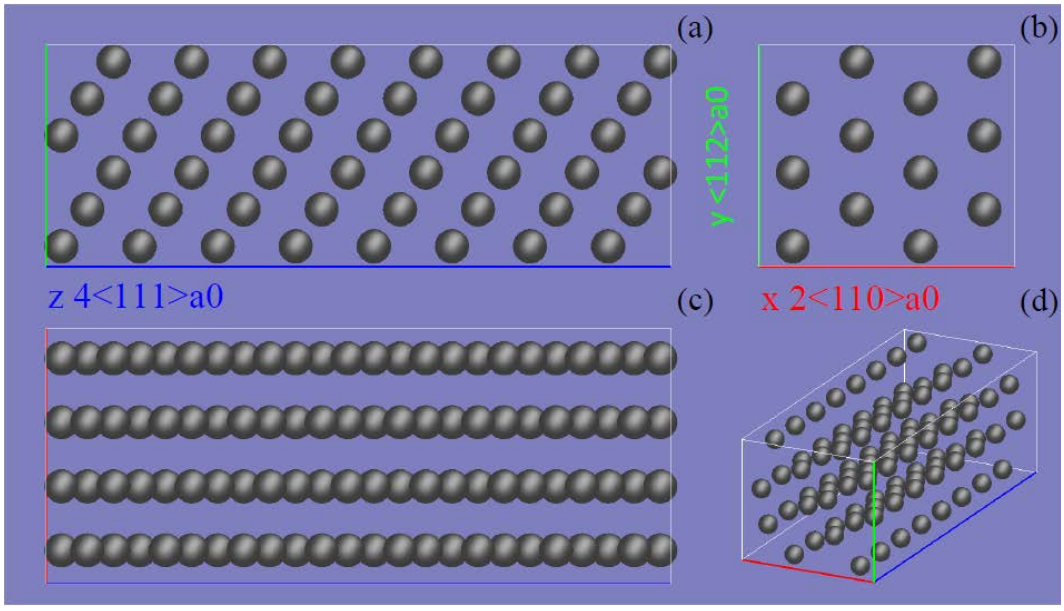

Figure 3-1: Standard views of the atomic configuration of a pure single crystal. (a) yz plane of the super cell, (b)xy plane, (c) xz plane, (d) trimetric view of the super cell. The red axis is x, green axis y, blue axis z. The length and crystallographic direction of each axis are also given in this figure. Unless specified otherwise, the layout setting applies to all the following configurations used in DFT calculations.

Figure 3-2 gives the atomic configuration of ∑3 (111) STGB which is used to calculate the GB energy. The sizes and crystallographic directions of the super cell are the same as the single crystal shown in Figure 3-1. The white atom inside the GB represents impurity atom (H, B, C, N, O, F, Al, Si, P, S, Cl, and Fe), and will be removed if we calculate the clean GB energy. The super cell contains 96 matrix atoms and one impurity atom. Since periodic boundary conditions are applied in all three directions, the super cell actually contains two GBs, one is in the middle of the cell, the other one is shared by the super cell and its periodic image.

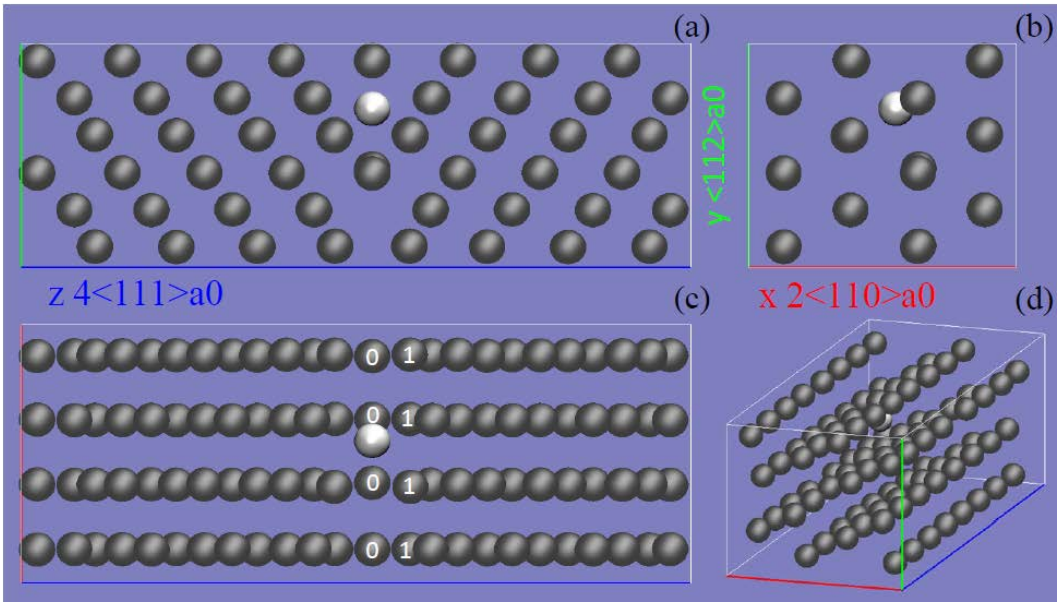

Figure 3-2: Standard views of the atomic configuration of ∑3 (111) STGB. The white atom is the interstitial impurity atom inside the GB. Atoms marked with number 0 or 1 are substitutional sites.

Figure 3-3 gives the atomic configuration of a single crystal containing two FS which is used to calculate the FS energy. The sizes along x and y directions and crystallographic directions of the super cell are the same as the single crystal shown in

Figure 3-1, however, we insert a space of 4Å between the outmost atoms and the super cell boundary in the z direction to create the FS. Since periodic boundary conditions are applied in all three directions, similarly to Figure 3-2, the super cell also contains two FS. The white atom represents the impurity atom and can be removed if we calculate the clean FS energy.

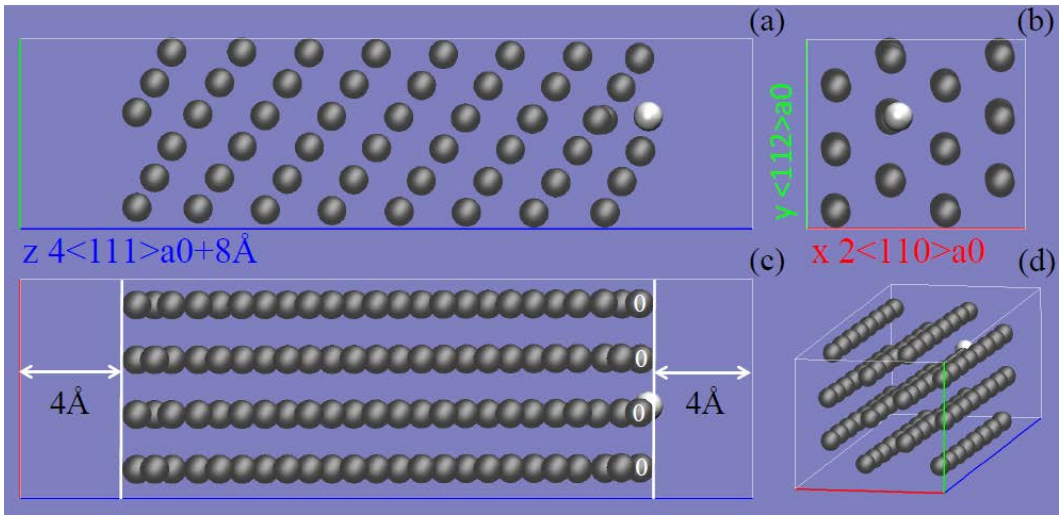

Figure 3-3: Standard views of the atomic configuration of the single crystal slab with two FS. The white atom is the interstitial impurity atom on the FS. Atoms marked with number 0 are substitutional sites.

The contaminated configurations shown above contain only one interstitial impurity atom in each super cell, thus it cannot be used to investigate the effect of impurity concentration level on the mechanical properties of GBs. To do this, we remove the interstitial atom in the GB shown in Figure 3-2 and replace some of the marked atoms with sulfur atoms. Five concentrations are investigated. The first sample contains only one sulfur atom which substitutes one of the 0 site atoms, and the concentration is 0.25ML (mono layer, 1ML corresponds to 4 atoms). The second sample contains two sulfur atoms which substitute two of the 0 site atoms, and so on. The fifth sample contains 8 sulfur

atoms which substitute the entire 0 site and 1 site atoms, and the concentration is 2ML. The two FS correspond to the first GB sample are one clean FS and one with a sulfur atom. The separation of the second sample generates two FS contaminated with one sulfur atom. The third GB produces one FS with one sulfur atom and one FS with two sulfur atoms. The fourth GB produces two FS contaminated with two sulfur atoms. The last GB produces two FS contaminated with four sulfur atoms. These contaminated FS can be created by substituting one to four of the 0 site atoms of the single crystalline slab (after removing the interstitial atom) shown in Figure 3-3.

In our MD simulations, for both tantalum and tungsten, seven STGBs are created inside the bi-crystal configurations using ideal CSL (coincident site lattice) construction [190], which is also used to construct the sample shown in Figure 3-2. Using CSL notations, the seven samples are denoted as ∑3{111}/<110>, ∑5{210}/<100>, ∑5{310}/<100>, ∑29{520}/<100>, ∑49{263}/<322>, ∑49{853}/<111>, and ∑49{194}/<511>. Periodic boundary conditions are used in all three directions of the orthorhombic samples. There are thus two GBs contained in each simulation box, one is in the middle of the box, and the other one is shared by the box and its periodic images. For each STGB sample, we create a single crystalline sample whose crystallographic direction is that of one of the grains of the bi-crystal sample to act as the reference configuration. We also created a single crystalline slab, the only difference between which and the single crystal sample is that we do not apply periodic boundary conditions in the direction that is perpendicular to the GB plane, so that we can calculate the energy of the surface formed after GB separation. The three different configurations contain the same number of atoms.

3.1.2 DFT and MD settings

We use the open source code CPMD [191] to perform the geometry optimization calculation. It is a parallelized code particularly designed for use in Car-Parrinelo molecular dynamics [192] using a plane wave basis set and pseudopotentials. In our calculations, the energy cutoff of the plane wave basis set used to expand the Kohn-Sham orbitals is 37Ry (1Ry=13.6eV) or 503eV. The exchange-correlation functional $E_{xc}[n]$ is developed by Perdew and Wang based on GGA scheme and is termed PW91 [183]. The interaction between ions and electrons is described using the Vanderbilt ultrasoft pseudopotentials [188]. During the geometry optimization process, the positions of the atoms are updated until the forces acting on them are less than 0.026eV/Å. To save calculation time, we use the adaptive gradient criterion in which the wave function convergence criterion is proportional to the energy gradient or force criterion by a factor of 0.0002. The validity of this relaxed criterion can be confirmed by the fact that the calculation of forces does not require highly converged wave functions.

Our MD simulations were performed using the large-scale atomic/molecular massively parallel simulator (LAMMPS) developed by Plimpton and co-workers [193, 194]. Two embedded atom method (EAM) interatomic potentials developed by Li [195] and Zhou [196] were used to describe the interatomic interactions of tantalum and tungsten respectively. The time step is 1fs during the simulations. The sample is relaxed using NPT MD (whereby the number of atoms, pressure and temperature of the sample are held constant) to ensure a zero pressure of the sample. The temperature for the seven different STGBs is 1K, which is different from that in DFT calculations where the temperature should be considered as 0K since we only perform geometry optimization calculations. Six

temperatures (1, 77, 100, 200, 300, and 400K) are used to simulate the temperature effect on the GB separation energy of the $\sum 3\{111\}$ STGB of tantalum, eight (1, 77, 100, 200, 300, 400, 500, 600K) are used for tungsten.

3.2 GB, FS, GB separation, and segregation energy calculations

First we need to calculate the binding energy which is the mechanical energy required to disassemble a whole bonded atomic system into isolated atoms through the formula

$$E = \sum_{i=1}^{N} M_{ISO}^{i} - E^{DFT}, \tag{3.1}$$

where E^{DFT} is the energy of the whole bonded system from DFT calculations, and M_{ISO}^{i} the energy of the *i*th isolated atom from DFT calculations. Then the binding energy of the single crystal system shown in Figure 3-1 is

$$E_{SGL} = N_M M_{ISO} - E_{SGL}^{DFT}.$$

The binding energy of the clean GB (without impurities) system is

$$E_{GB} = N_M M_{ISO} - E_{GB}^{DFT}.$$

The binding energy of the GB system with one impurity atom is

$$E_{GB}^{I} = N_M M_{ISO} + I_{ISO} - E_{GB}^{I,DFT}.$$

The binding energy of the clean free surface (FS) system is

$$E_{FS} = N_M M_{ISO} - E_{FS}^{DFT}.$$

The bind energy of the FS system with one impurity atom is

$$E_{FS}^{I} = N_M M_{ISO} + I_{ISO} - E_{FS}^{I,DFT},$$

where N_M is the number of matrix atoms, M_{ISO} the energy of an isolated matrix atom, I_{ISO} the energy of an isolated impurity atom.

When introducing a GB inside a single crystal, the binding energy of the system will decrease. The GB energy is defined as the loss of binding energy divided by the GB area. Then for the configuration shown in Figure 3-2, the clean GB energy is

$$\gamma_{GB} = \frac{E_{SGL} - E_{GB}}{2A} = \frac{E_{GB}^{DFT} - E_{SGL}^{DFT}}{2A}, \tag{3.2}$$

where A is the area of the GB. The super cell in Figure 3-2 includes one clean GB and a contaminated GB if counting the impurity atom, we have

$$\gamma_{GB} + \gamma_{GB}^{I} = \frac{E_{SGL} - E_{GB}^{I}}{A}.$$

Then the energy contaminated GB is

$$\begin{aligned} \gamma_{GB}^{I} &= \frac{E_{SGL} - E_{GB}^{I}}{A} - \gamma_{GB} \\ &= \gamma_{GB} - \frac{\mu_{GB}^{I}}{A}, \end{aligned} \tag{3.3}$$

where

$$\mu_{GB}^{I} \triangleq E_{GB}^{I} - E_{GB} = E_{GB}^{DFT} + I_{ISO} - E_{GB}^{I,DFT},$$

is the binding energy of the impurity atom inside the GB.

Similarly, for the FS energy we have

The clean FS energy

$$\gamma_{FS} = \frac{E_{SGL} - E_{FS}}{2A} = \frac{E_{FS}^{DFT} - E_{SGL}^{DFT}}{2A}. \tag{3.4}$$

The energy of the contaminated FS

$$\begin{aligned} \gamma_{FS}^{I} &= \frac{E_{SGL} - E_{FS}^{I}}{A} - \gamma_{FS} \\ &= \gamma_{FS} - \frac{\mu_{FS}^{I}}{A}, \end{aligned} \tag{3.5}$$

where

$$\mu_{FS}^{I} \triangleq E_{FS}^{I} - E_{FS} = E_{FS}^{DFT} + I_{ISO} - E_{FS}^{I,DFT},$$

is the binding energy of the impurity atom on the FS.

When GB separation occurs, two FS will be generated. The GB separation energy is defined as

$$2\gamma_{SEP}^{X} = \gamma_{FS}^{1} + \gamma_{FS}^{2} - \gamma_{GB}^{X}. \tag{3.6}$$

This is the minimum amount of work per unit area done to make GB separation happen. Here we use the superscript X to denote general type of GBs. For the clean ∑3(111) STGB shown above, the two generated FS are identical, thus the GB separation energy is

$$2\gamma_{SEP} = 2\gamma_{FS} - \gamma_{GB}. \tag{3.7}$$

However, for the separation of a contaminated GB, one of the FS is clean; the other one contains the impurity atom that originally resides in the GB before separation. The GB separation energy in this case is

$$\begin{aligned} 2\gamma_{SEP}^{I} &= \gamma_{FS}^{I} + \gamma_{FS} - \gamma_{GB}^{I} \\ &= 2\gamma_{SEP} + \frac{\Delta\mu^{I}}{A}, \end{aligned} \tag{3.8}$$

where

$$\Delta\mu^{I} = \mu_{GB}^{I} - \mu_{FS}^{I} \tag{3.9}$$

is the binding energy difference of the impurity atom between scenarios when it is with the GB and the FS, respectively.

The GB/FS segregation energy of the impurity atom is defined as the difference of the binding energies between the GB/FS site and the inner bulk site [197]. The binding energy of the impurity atom inside the bulk site is

$$\mu_{SGL}^{I} \triangleq E_{SGL}^{I} - E_{SGL} = E_{SGL}^{DFT} + I_{ISO} - E_{SGL}^{I,DFT}. \tag{3.10}$$

Thus the GB segregation energy is

$$\begin{aligned} \Delta\mu_{GB}^{I} &\triangleq \mu_{GB}^{I} - \mu_{SGL}^{I} \\ &= \left(E_{GB}^{DFT} - E_{GB}^{I,DFT}\right) - \left(E_{SGL}^{DFT} - E_{SGL}^{I,DFT}\right). \end{aligned} \tag{3.11}$$

Similarly, the FS segregation energy is

$$\begin{aligned}\Delta\mu_{FS}^{I} &\triangleq \mu_{FS}^{I} - \mu_{SGL}^{I} \\ &= \left(E_{FS}^{DFT} - E_{FS}^{I,DFT}\right) - \left(E_{SGL}^{DFT} - E_{SGL}^{I,DFT}\right).\end{aligned} \tag{3.12}$$

The binding energy of the impurity atom with the matrix material can be divided into two parts: chemical energy defined as the work needed to remove the impurity while keep the host atoms fixed [62] and mechanical energy defined as the binding energy decrease of the host atoms due to impurity induced local distortion. If we use $E^{\circ,DFT}$ and E° to represent the total energy and binding energy of the system after removing the impurity, then the chemical energy is

$$\begin{aligned}\mu^{I,Chem} &\triangleq E^{I} - E^{\circ} \\ &= E^{\circ,DFT} + I_{ISO} - E^{I,DFT}.\end{aligned} \tag{3.13}$$

The mechanical energy is

$$\begin{aligned}\mu^{I,Mech} &\triangleq E - E^{\circ} \\ &= E^{\circ,DFT} - E^{DFT}.\end{aligned} \tag{3.14}$$

Then the binding energy of the impurity atom with the host material is

$$\mu^{I} = \mu^{I,Chem} - \mu^{I,Mech}. \tag{3.15}$$

The GB segregation energy is

$$\Delta\mu_{GB}^{I} = \Delta\mu_{GB}^{I,Chem} + \Delta\mu_{GB}^{I,Mech}, \tag{3.16}$$

where $\Delta\mu_{GB}^{I,Chem} = \mu_{GB}^{I,Chem} - \mu_{SGL}^{I,Chem}$ is the chemical contribution, and $\Delta\mu_{GB}^{I,Mech} = \mu_{SGL}^{I,Mech} - \mu_{GB}^{I,Mech}$ the mechanical contribution.

The FS segregation energy is

$$\Delta\mu_{FS}^{I} = \Delta\mu_{FS}^{I,Chem} + \Delta\mu_{FS}^{I,Mech}, \tag{3.17}$$

where $\Delta\mu_{FS}^{I,Chem} = \mu_{FS}^{I,Chem} - \mu_{SGL}^{I,Chem}$ is the chemical contribution, and $\Delta\mu_{FS}^{I,Mech} = \mu_{SGL}^{I,Mech} - \mu_{FS}^{I,Mech}$ the mechanical contribution.

The binding energy difference in Equation 3.9 is

$$\Delta\mu^{I} = \Delta\mu^{I,Chem} + \Delta\mu^{I,Mech}, \tag{3.18}$$

where $\Delta\mu^{I,Chem} = \mu_{GB}^{I,Chem} - \mu_{FS}^{I,Chem}$ is the chemical contribution, and

$\Delta\mu^{I,Mech} = \mu_{FS}^{I,Mech} - \mu_{GB}^{I,Mech}$ the mechanical contribution.

3.3 Results

From Equations 3.1-3.9, we can calculate the GB, FS and GB separation energies of tantalum and tungsten based on the output of DFT calculations. The results are shown in the following sections.

3.3.1 GB energy

The GB energies for tantalum and tungsten are calculated from equations 3.2 and 3.3 and are shown in Figure 3-4. Almost all the impurities decrease the GB energy of both tantalum and tungsten except for chlorine which increases the GB energy of tungsten. The change of GB energies of tantalum and tungsten against various impurities follows the same trend and correlates with the group and period of these impurity elements in the Periodic Table of the Elements. For the impurity elements in the same period, such as from boron to fluorine, and from aluminum to chlorine, the GB energies of both metals first decrease then increase with the increasing group number. For the elements in the same group, it is observed that the decreasing effect of impurity elements with lower period is always higher than that of elements with higher period. Most importantly, given the same impurity element, the GB energy of tungsten is always higher than that of tantalum; even the quantitative differences of GB energy between tantalum and tungsten are quite close. It needs to be pointed out that the GB energy ($0.175 eV/Å^2$) of pure tungsten from our calculation is less than half of that ($0.5823 eV/Å^2$) from Grujicic's [14] MD simulations.

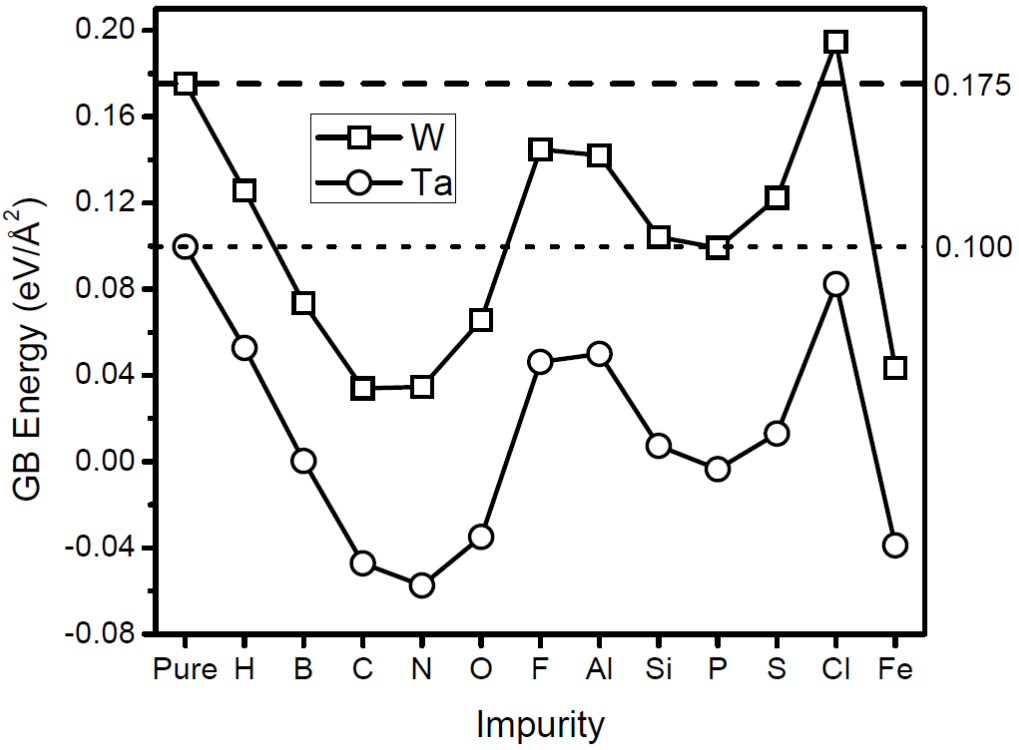

Figure 3-4: GB energy of a ∑3 STGB for tantalum and tungsten with and without impurities. The dashed line shows the GB energy level of pure tungsten, and the dotted line gives the GB energy level of pure tantalum, respectively.

3.3.2 Surface energy

The surface energy of the {111} plane for tantalum and tungsten are calculated from equations 3.4 and 3.5 and are shown in Figure 3-5. The findings are very similar to that for GB energy. All the impurities decrease the surface energy of both tantalum and tungsten. The change of surface energies of tantalum and tungsten against various impurities follows the same trend and correlates with the group and period of these impurity elements in the Periodic Table. For the impurity elements in the same period, the surface energies of both metals first decrease and then increase with the increasing group number. For the elements in the same group, it is observed that the decreasing effect of

impurity elements with lower period is always higher than that of elements with higher period. But the difference between them becomes smaller when compared with that in the decreasing effect on GB energy, indicating that the GB energy is more sensitive to the period of impurity elements than the surface energy. Given the same impurity element, the surface energy of tungsten is also always higher than that of tantalum; and the quantitative differences of surface energy between them are quite close. The surface energy (0.229eV/Å^2) of pure tungsten from our calculation is still less than that (0.4285eV/Å^2) from Grujicic's [14] MD simulations.

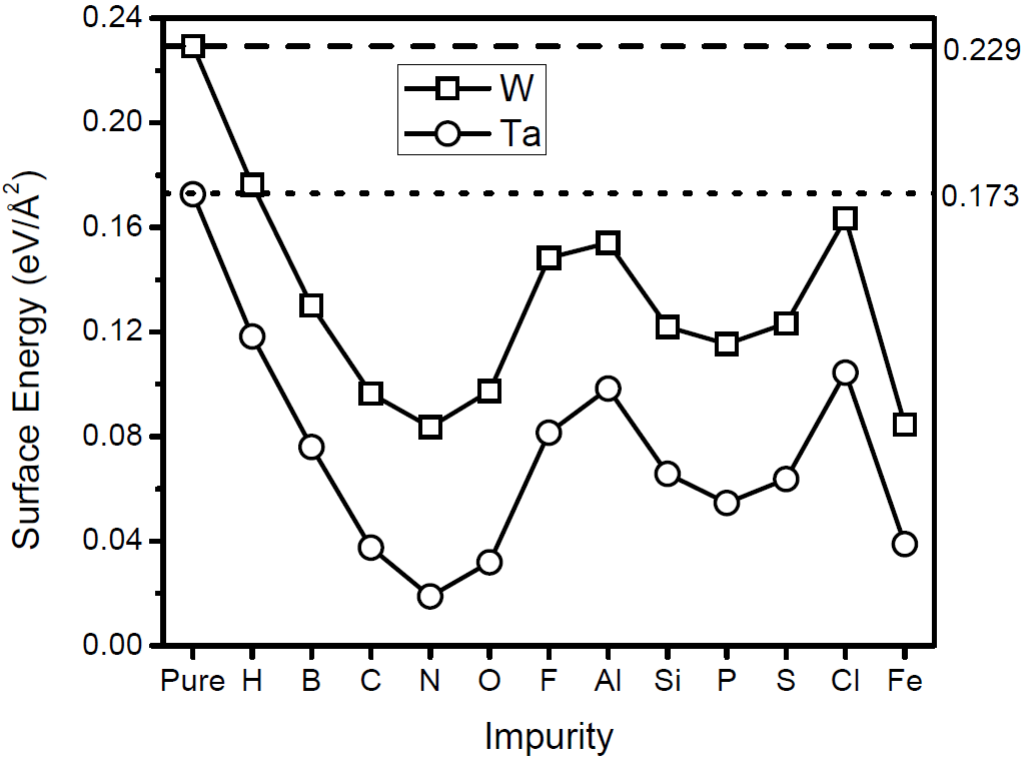

Figure 3-5: Surface energy of {111} plane for tantalum and tungsten with and without impurities. The dashed line shows the FS energy level of pure tungsten, the dotted line shows that of pure tantalum.

3.3.3 The binding energy difference of impurity between GB and FS

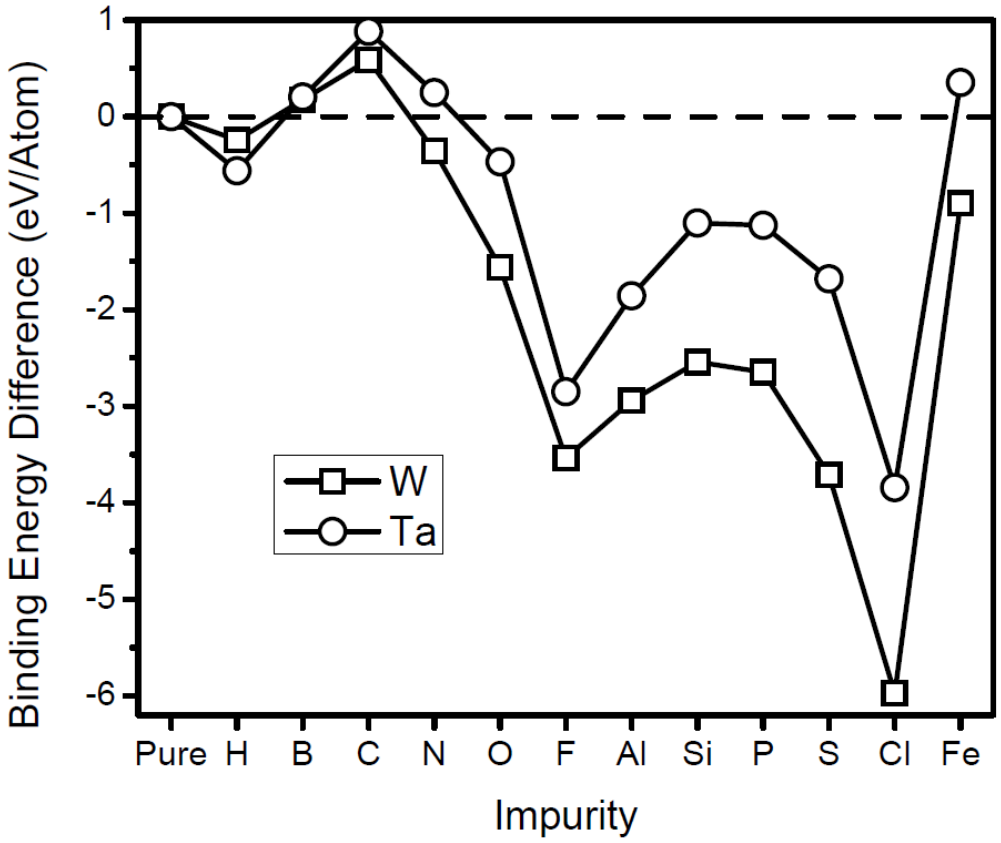

Figure 3-6: Binding energy difference of impurity atoms in between GB and FS for tantalum and tungsten. The binding energy difference between clean GB and FS is set to be zero and acts as reference value, the position of which is marked by the dashed line.

The binding energy difference of various impurities with tantalum and tungsten is calculated from Equations 3.9 and the results are shown in Figure 3-6. This parameter reveals the site preference of impurity atoms. A negative value means that the binding energy of the impurity atom with GB is less than that with FS, and therefore the impurity atom 'prefers' to stay on FS, rather than inside the GB, whereas a positive value means otherwise. From the results displayed in Figure 3-6, we can see that almost all the

impurities have negative binding energy difference for both tantalum and tungsten. Exceptions include boron and carbon in both metals and nitrogen and iron in tantalum. This indicates that only carbon and boron can increase the GB separation energy of both metals according to Equation 3.8. Similar to the GB and FS energy, the change of binding energy difference of tantalum and tungsten against various impurities follows the same trend and correlates with the group and period of these impurity elements in the Periodic Table. For the impurity elements in the same period, the binding energy difference for both metals first increases, and then decreases with the increasing group number, revealing that, although the effect of various impurities on GB and FS energy follows a similar trend, impurity atoms with moderate group numbers show the preferential tendency to sit inside GB. For the elements in the same group, it is observed that the binding energy difference of impurity elements with lower period is always higher than that of elements with higher period, indicating the tendency to sit inside GB for the former impurities. For hydrogen, the binding energy difference of tungsten is always higher than that of tantalum; however, for the rest of the impurities, the binding energy difference of tungsten is always lower than that of tantalum. This indicates that tungsten is more sensitive to impurity with high period, but it is less sensitive to low period impurity elements than tantalum.

The results shown in Figure 3-6 negate the charge transfer model [54] which states that the impurity with higher electronegativity will have more embrittling effect on the GB by drawing charges from its neighboring atoms, though the results do show a relevance to the electronegativity of impurities in that fluorine and chlorine, the elements that possess the highest electronegativity in the Periodic Table, have the strongest embritlling effect on the GB of both tantalum and tungsten. For example, the electronegativity increases with

increasing group number for elements from the same period, such as from boron to fluorine or from aluminum to chlorine. However, the embrittling effect first decreases and then increases with the increasing group number. The model seems to be appropriate only for impurity elements with large group numbers. If considering the elements in the same group, for example fluorine and chlorine, the embrittling effect of a low period impurity that possesses higher electronegativity is actually less than that of a high period impurity that possesses lower electronegativity. This indicates that the electronegativity per se is not a good indicator to the embrittling trend and other mechanisms such as size effect should be responsible for it.

3.3.4 GB separation energy

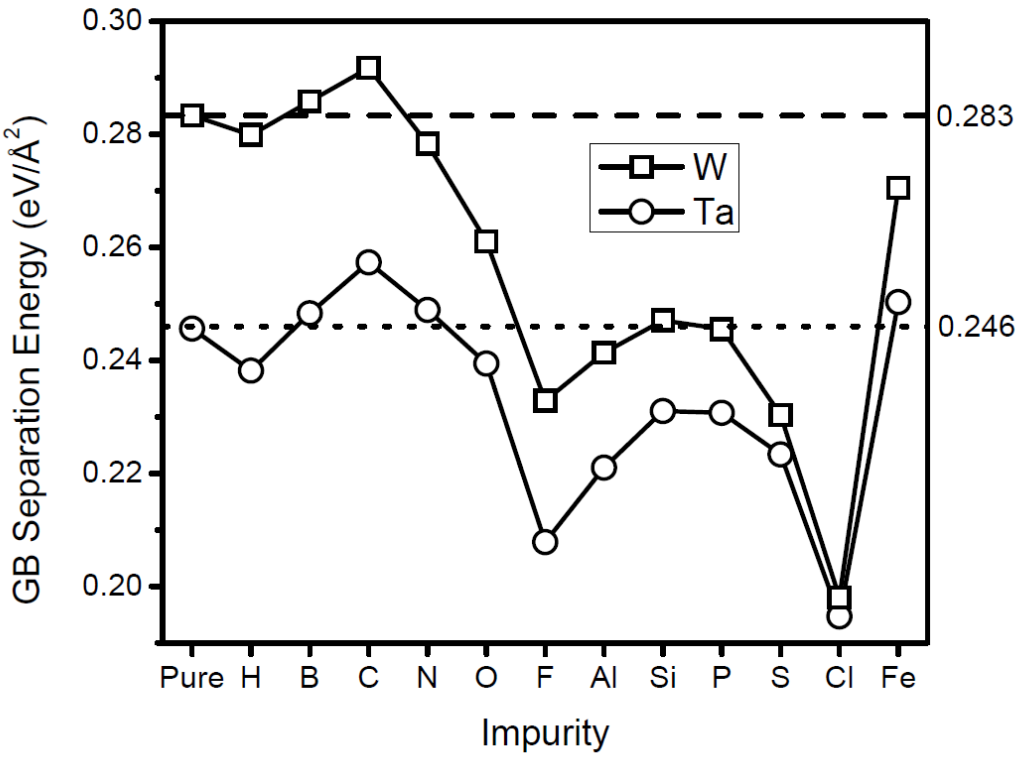

Figure 3-7: GB separation energy of ∑3 STGB for tantalum and tungsten with and without impurities. The dashed line shows the clean GB separation energy level of tungsten, and the dotted line shows that of tantalum.

The GB separation energy for tantalum and tungsten are calculated from Equations 3.7 and 3.8. The results of calculations are presented in Figure 3-7. Almost all the impurities decrease the GB separation energy of both tantalum and tungsten. Exceptions include boron and carbon which strengthen the GB of both metals and nitrogen and iron which strengthen the GB of tantalum. The GB separation energy of tantalum and tungsten against various impurities follows the same trend and correlates with the group and period of these impurity elements in the Periodic Table. These findings are consistent with binding energy difference shown in Figure 3-6 because of Equation 3.8. For the impurity elements in the same period, such as from boron to fluorine, and from aluminum to chlorine, the GB separation energies of both metals first increase and then decrease with the increasing group number. For the elements in the same group, it is observed that the separation energy of GB contaminated with lower period impurity element is always higher than that of GB contaminated with higher period elements. For the same impurity element, the GB separation energy of tungsten is always higher than that of tantalum. The clean GB separation energy of tungsten is 0.283eV/Å^2, close to Grujicic's [14] result (0.2747eV/Å^2), but less than that from Dorfman's [32] Monte Carlo atomistic simulations (0.3424 eV/Å^2). The ratio (0.246/0.283=0.87) of the clean GB separation energy between tantalum and tungsten is close to that (8.1/8.9=0.91) of cohesive energy between the two metals, indicating that the GB separation energy is approximately proportional to the cohesive energy.

3.3.5 GB separation energy for various concentration of sulfur

We only calculated the effect of the concentration level of sulfur on the GB separation energy, since sulfur is one of the primary allegedly detrimental impurity

elements that exist in commercially pure tungsten [198] and is also known to embrittle the GB of nickel [37]. The results of calculations are displayed in Figure 3-8. From the results

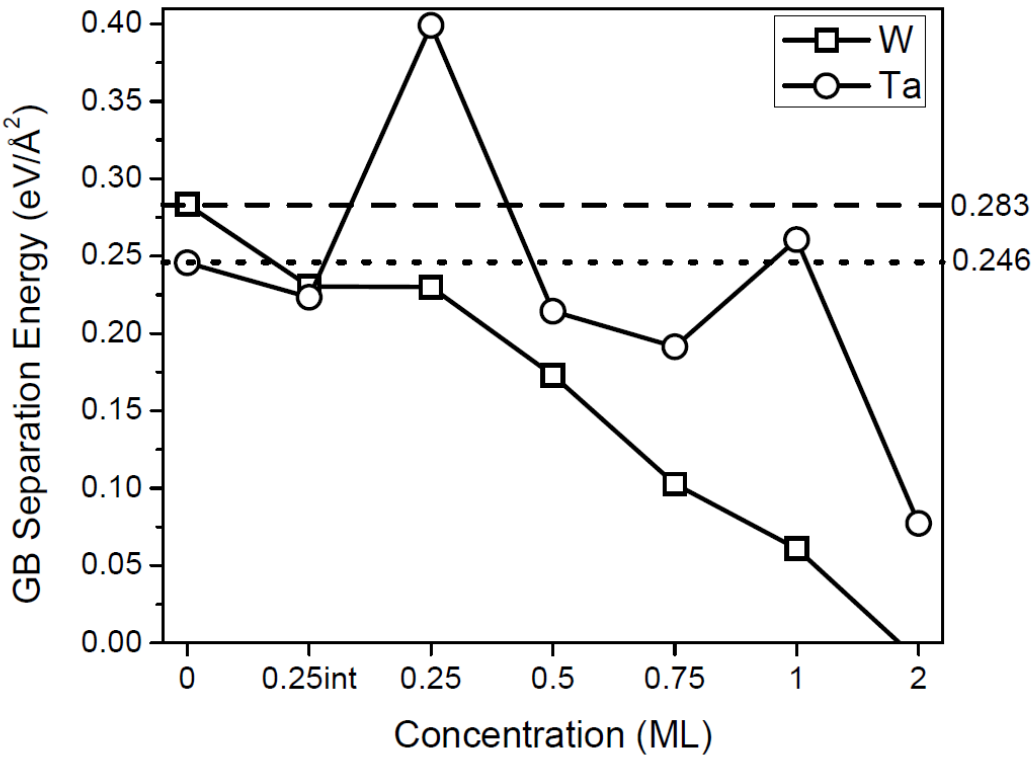

Figure 3-8: GB separation energy of ∑3 STGB for tantalum and tungsten with various concentration levels of sulfur atoms. The dashed line shows the clean GB separation energy level of tungsten, the dotted line shows that of tantalum. The tick label 0.25int represents the GB with one interstitial sulfur atom as shown in Figure 3-2, and the rest represent GB with or without substitutional sulfur atoms.

we can see that the GB separation energy of tungsten decreases rapidly with the increasing concentration level, and is less than that of tantalum when the concentration of sulfur is more than 0.25ML. It even becomes negative at concentration level of 2ML. The change of GB separation energy of tantalum against concentration level is different with that of tungsten. The overall trend is similar. However, the GB separation energy for tantalum does not decrease monotonically with the increasing concentration. Instead, two spikes are

detected at the concentration level of 0.25ML and 1ML, respectively. The separation energy of tantalum GB at the concentration of 0.25ML is even higher than that of clean tungsten GB. Although the two exceptions are due to the annihilation of the two GBs during the geometry optimization process based on the corresponding atomic configurations, it suffices to say that GB separation energy of tungsten is very sensitive to sulfur concentration level, consistent with experimental observations [73], whereas that of tantalum is tolerant to sulfur concentration level.

3.3.6 GB separation energy of different GB structures

The GB separation energy of various clean CSL STGBs for tantalum and tungsten is given in Figure 3-9. It is obvious that for any specific GB structure, the GB separation energy of tungsten is always higher than that of tantalum. This can be understood in terms of the universal features of bonding in metals which explains the empirical result that the surface energy per surface atom is proportional to the cohesive energy per bulk atom [199]. Since the cohesive energy of tungsten is higher than that of tantalum, the surface energy of tungsten should be higher than that of tantalum, which actually has been observed in our DFT and MD calculations. It is also reasonable to assume qualitatively that the GB energy and GB separation energy of tungsten is higher than those of tantalum. It is worth noting that GB separation energy of the $\sum 3$ STGB of both metals based on MD calculations is less than that calculated using DFT method. This is probably because we have adjusted the box size to reach zero pressure state in MD simulations, thus the change in the cross section area of the GB and surface will change the GB energy, surface energy and eventually the GB separation energy. Another possible reason can be attributed to the less accurate EAM potentials used in MD simulations when compared with the accuracy of DFT calculations.

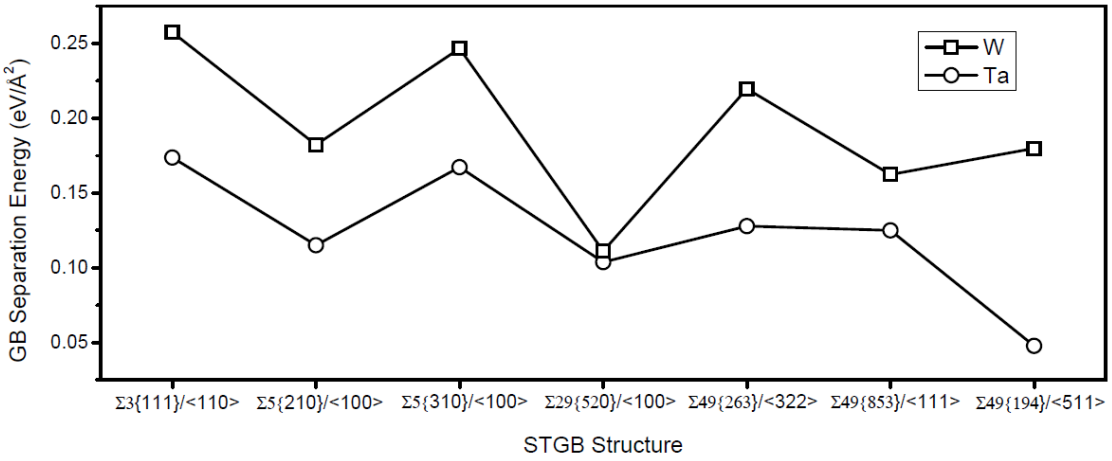

Figure 3-9: GB separation energy of various clean CSL STGBs for tantalum and tungsten from MD simulations.

3.3.7 Effect of temperature on GB separation energy

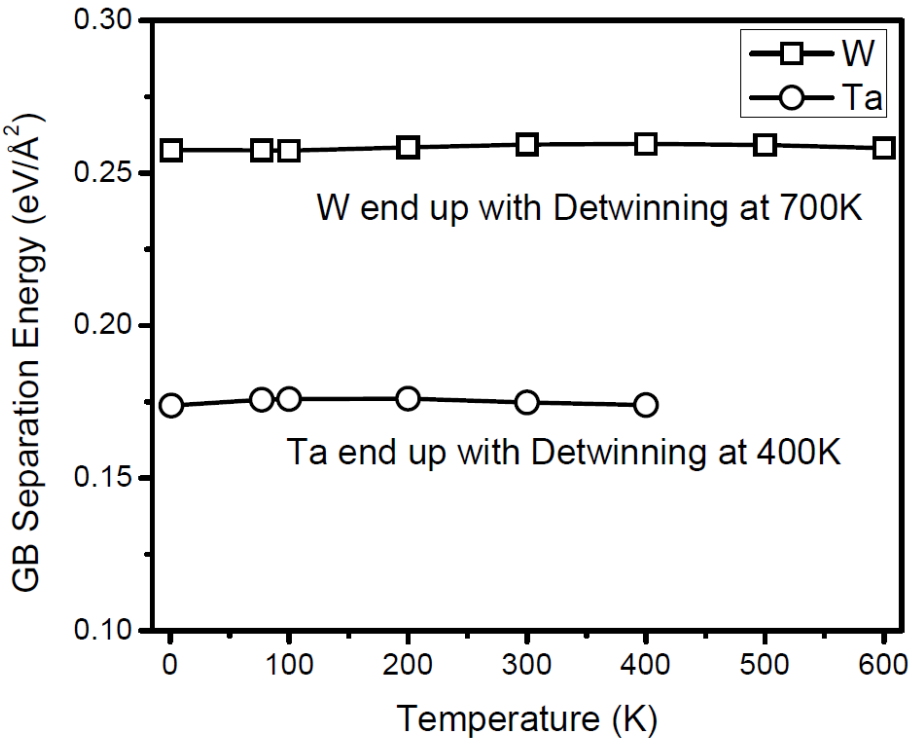

Figure 3-10: GB separation energy of the ∑3 STGB of tantalum and tungsten as a function of temperature.

Figure 3-10 shows the effect of temperature on the GB separation energy of the ∑3 STGB. From this figure we can see that for both tantalum and tungsten, the GB separation energy is not a strong function of temperature. In fact, our results displayed in Figures 3-11 and 3-12 show that both the GB energy and surface energy are not strong functions of temperature. When calculating the GB and surface energies at various temperatures, we make the reference atomic configuration at the same temperature, and thus the total kinetic energies of the atoms in the reference configuration and that contains GBs or surfaces are actually equal. The total energy difference between them is therefore the difference in the potential energy, since the kinetic energy terms cancel each other. This means that GB and surface energy is not a function of temperature unless the temperature induced microstructural transition occurs that leads to the change of the potential energy. So the small change of GB energy, surface energy and GB separation energy for various temperatures observed in our MD simulations is due to this transition, which can be confirmed by Figure 3-13. It shows that the equilibrium structure of ∑3 STGB of tantalum become more disordered at 77K compared with that at 1K. This temperature induced transition from an ordered state to a more disordered state also occurs in tungsten at about 200K. The transition leads to a subtle decrease in GB energy, as shown in Figure 3-11, and a subtle increase in GB separation energy, as shown in Figure 3-10, indicating that the ordered GB is a metastable structure, whereas the disordered GB at higher temperature is more stable. Keeping increasing the temperature will not increase the GB separation energy further, but eventually the two GBs contained in the super cell annihilate into a single crystal for tantalum at 400K and tungsten at 700K.

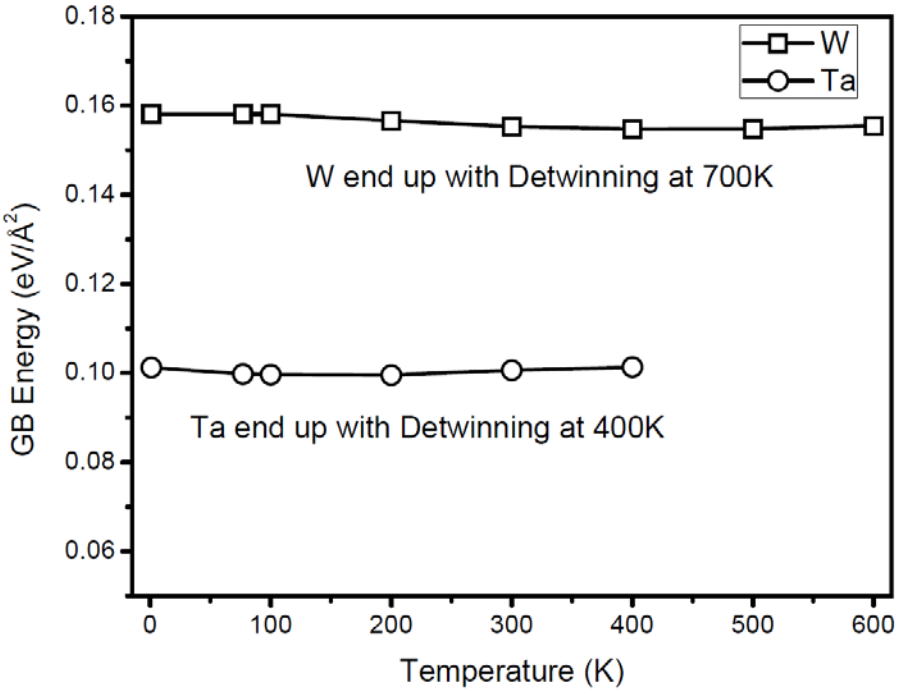

Figure 3-11: GB energy of the ∑3 STGB of tantalum and tungsten as a function of temperature.

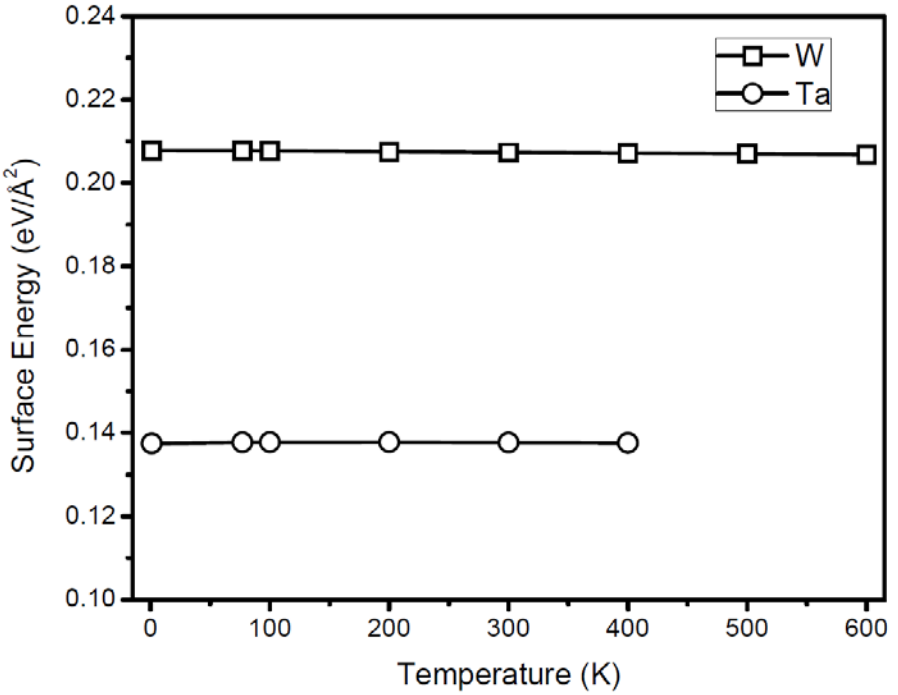

Figure 3-12: Surface energy of the ∑3 STGB of tantalum and tungsten as a function of temperature

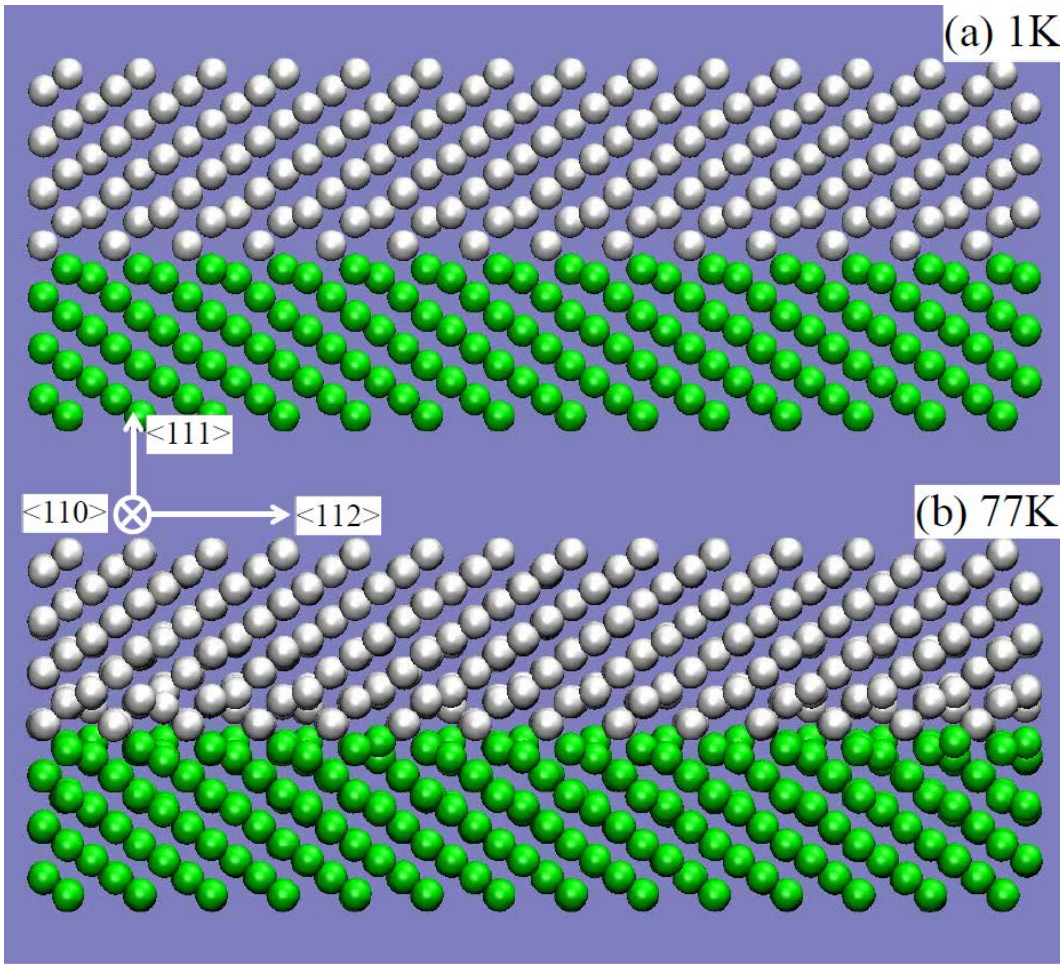

Figure 3-13: Equilibrium structures of ∑3 STGB of tantalum at 1K (a) and 77K (b) from MD simulations.

3.3.8 Impurity segregation energy

Impurity segregation energy determines where the impurity likes to stay: in the bulk, at the GB or on the FS. The higher the segregation energy, the more likely the impurity is segregated from a bulk site into some other sites, or in other words, the impurity is more likely to stay in other sites than within the bulk. It also determines whether the impurity has the chance to influence the GBs. The GB segregation energies of various impurities in tantalum and tungsten are calculated using Equation 3.11 and the results of

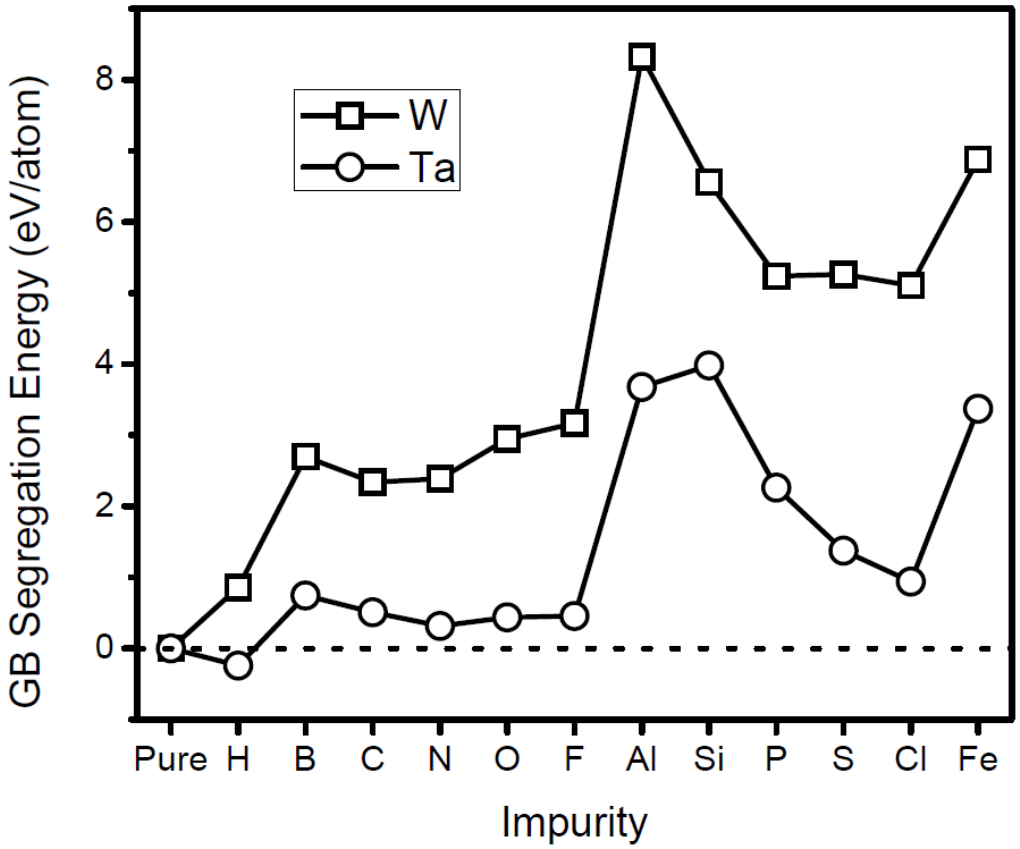

Figure 3-14: GB segregation energy of various impurities. The dotted line shows the position of zero segregation energy.

calculations are shown in Figure 3-14. Almost all the impurities have positive GB segregation energy and are likely segregated from bulk site into GBs, resulting in the change of GB separation energy. Hydrogen stands out to be an exception in that it has a negative GB segregation energy in tantalum, indicating that the bulk site is the energetically more favorable site for this impurity. Like the GB separation energy, the GB segregation energy of tantalum and tungsten against various impurities correlates with the group and period of these impurity elements in the Periodic Table. For the elements in the same group, the GB segregation energy of impurity elements with lower period is always lower than that of elements with higher period, indicating that impurities with higher

period are more likely to be segregated into GBs. Most importantly, for the same impurity element, the GB segregation energy in tungsten is always higher than that in tantalum. For the light impurity elements from hydrogen to fluorine, the GB segregation energy in tantalum is close to zero, but it has significant values in tungsten. This finding suggests that impurities in tungsten are much more likely to be segregated into GBs, and thus affecting (usually embrittling) the GBs significantly.

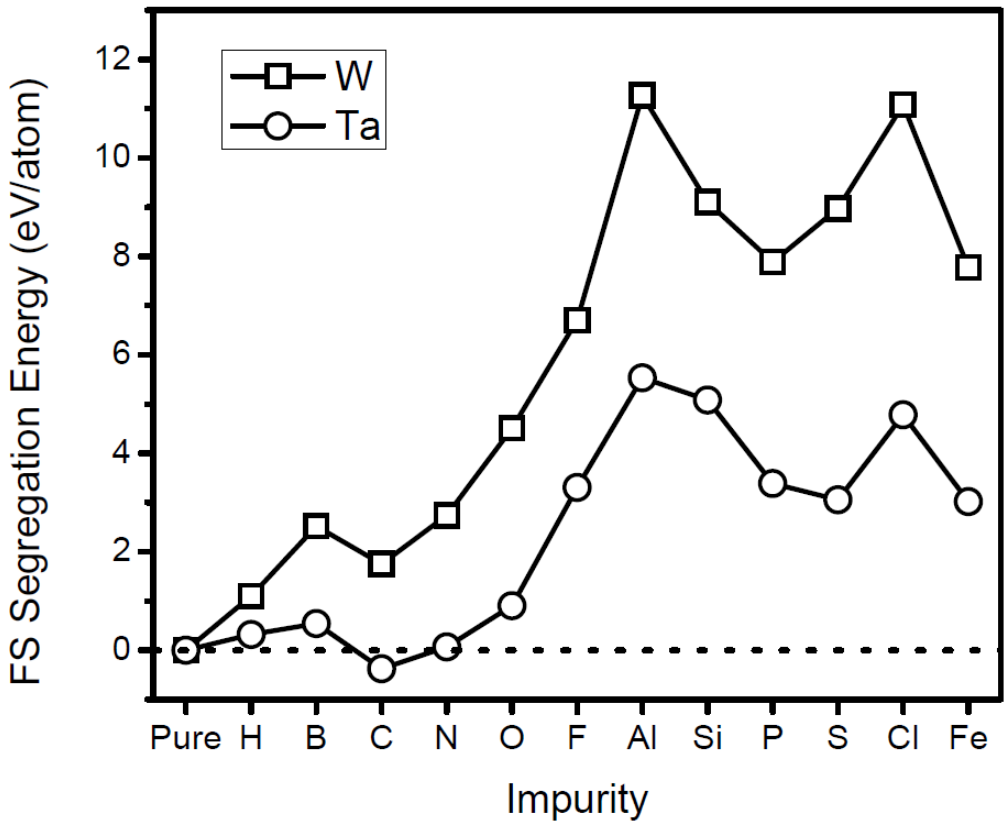

Figure 3-15: FS segregation energy of various impurities. The dotted line shows the position of zero segregation energy.

The FS segregation energy of impurities in tantalum and tungsten are calculated using Equation 3.12 and the results of calculations are shown in Figure 3-15. Almost all the

impurities have positive FS segregation energy except for carbon in tantalum, suggesting the possibility of being segregated from bulk site onto surface site. The FS segregation energy in both metals follows almost exactly the same trend and shows a stronger correlation with the period and group number of impurity elements than GB segregation energy. For the impurity elements in the same period, such as from boron to fluorine, and from aluminum to chlorine, the FS segregation energy first decreases and then increases with the increasing group number. While for impurity elements in the same group, the FS segregation energy of high period impurity elements is always higher than that of low period elements, indicating that the former elements have more possibility of being segregated onto surface sites. Compared with GB segregation energy, it is observed that impurities that embrittle the GB have higher FS segregation energy, whereas impurities such as carbon and boron that strengthen the GB such as carbon and boron in tungsten have higher GB segregation energy. Like GB segregation energy, the FS segregation energy in tungsten is always higher than that in tantalum.

3.4 Discussion

To understand why and how impurities influence GBs, we follow the common practice in the literature that divides the effect of impurities on GB separation and segregation energy into chemical effect and mechanical effect, respectively. In what follows, we will present calculation results and discussion on the results. The first two subsections in the following will about the chemical effect and mechanical effect, respectively. The relationship between chemical and mechanical effect and impurity concentration level effect are discussed in the subsequent subsections.

3.4.1 Chemical effect

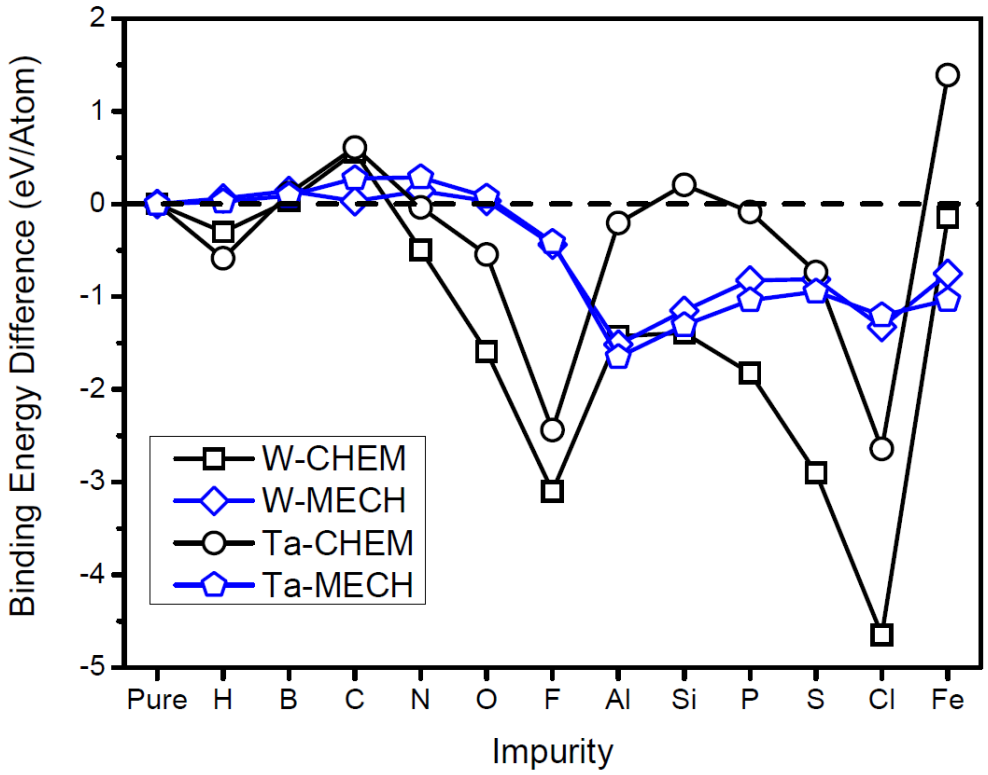

Figure 3-16: Chemical (black curves) and mechanical (blue curves) contributions of binding energy difference of impurity atoms in between GB and FS for tantalum and tungsten. The binding energy difference between clean GB and FS is set to be zero and is used as the reference value, the position of which is marked by the dashed line.

The chemical contribution of the binding energy difference of various impurities with tantalum and tungsten is calculated using Equations 3.18 and results of calculations are shown in Figure 3-16. The trend of the two curves is analogous to the total binding energy difference curves shown in Figure 3-6. Almost all the impurities have negative chemical binding energy difference for both tantalum and tungsten. Exceptions include for boron and carbon in both tantalum and tungsten and silicon and iron in tantalum. The

change in the chemical binding energy difference of both metals against various impurities follows the same trend and strongly correlates with the group and period of these impurity elements in the Periodic Table. The chemical binding energy difference first increases and then decreases with increasing group number for elements in the same period, showing strong group dependent behavior; whereas for the impurities in the same group, it decreases with increasing period. From hydrogen to carbon, the chemical effects on the two metals are close to each other; from nitrogen to iron, the chemical effect on tungsten is always higher than that on tantalum, and the difference between them increases with increasing period of impurity elements. Despite its detrimental total effect, silicon actually has a beneficial chemical effect on tantalum. As the only transition metal impurity in our study, iron has the best beneficial chemical effect on tantalum, and trivial effect on tungsten.

The chemical contributions of GB segregation energy of various impurities in tantalum and tungsten are shown in Figure 3-17. The overall trend of the two curves looks similar to that of the total GB segregation energy curves shown in Figure 3-14 despite some local discrepancies such as the position of the peak value. However, the correlation with period and group number of impurity element is not as prominent as that of the total GB segregation energy. For example, from hydrogen to fluorine, the chemical GB segregation energy of these impurities in tantalum is close to zero or even negative. In tungsten, however, the chemical GB segregation energy increases monotonically with increasing group number. For the impurities in the same group, the chemical GB segregation energy of low period impurity is not always lower than that of a high period impurity anymore. Examples are provided by comparison between oxygen and sulfur in tungsten and that

between fluorine and chlorine in tantalum. Analogous to the curves in Figure 3-14, the chemical GB segregation energy of each impurity in tungsten is almost always higher than that in tantalum, except for iron which has close chemical GB segregation energy in both metals.

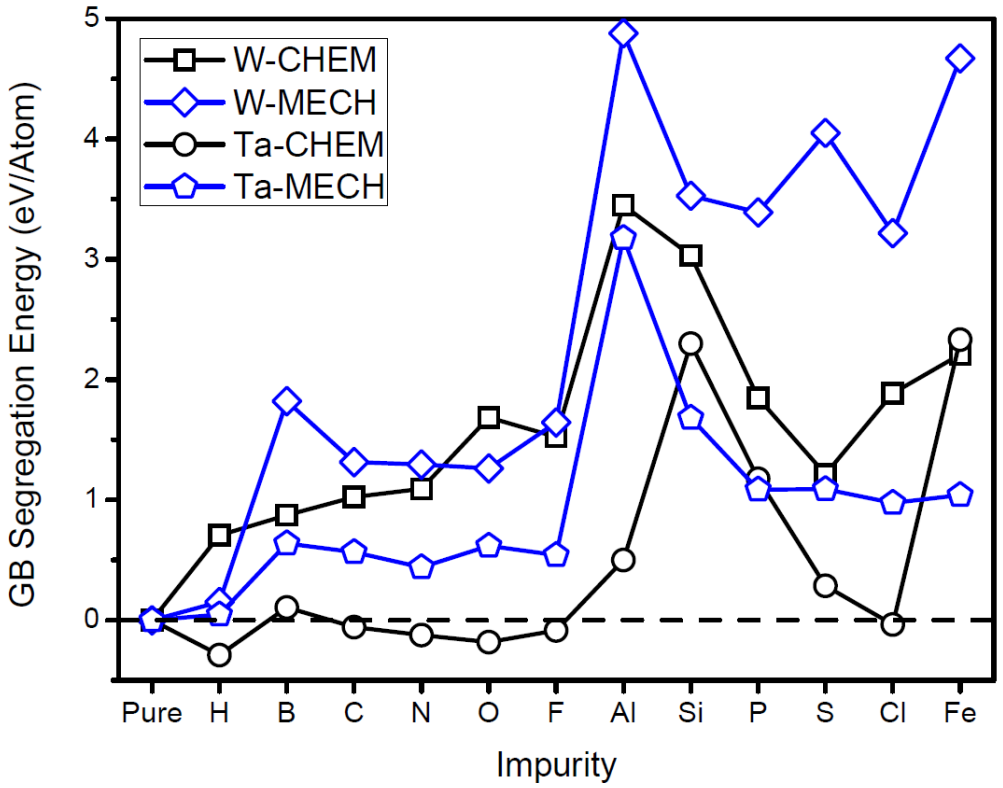

Figure 3-17: Chemical (black curves) and mechanical (blue curves) contributions of GB segregation energy of various impurities. The dashed line shows the position of zero segregation energy.

The chemical contributions of FS segregation energy of various impurities in both metals are shown in Figure 3-18. The trend of the curves is quite similar to that of the total FS segregation energy shown in Figure 3-15. For the impurity elements in the same period, the chemical FS segregation energy first decreases and then increases with increasing

group number of the impurity, whereas within the same group, the chemical FS segregation energy of a low period impurity is always lower than that of a high period impurity. The only exception is aluminum; when compared with fluorine and silicon, the chemical FS segregation energy of which reaches a local maximum value in tungsten. But a local minimum value is observed in tantalum. Analogous to the total FS segregation energy, the chemical FS segregation energy of each impurity in tungsten is always higher than that in tantalum.

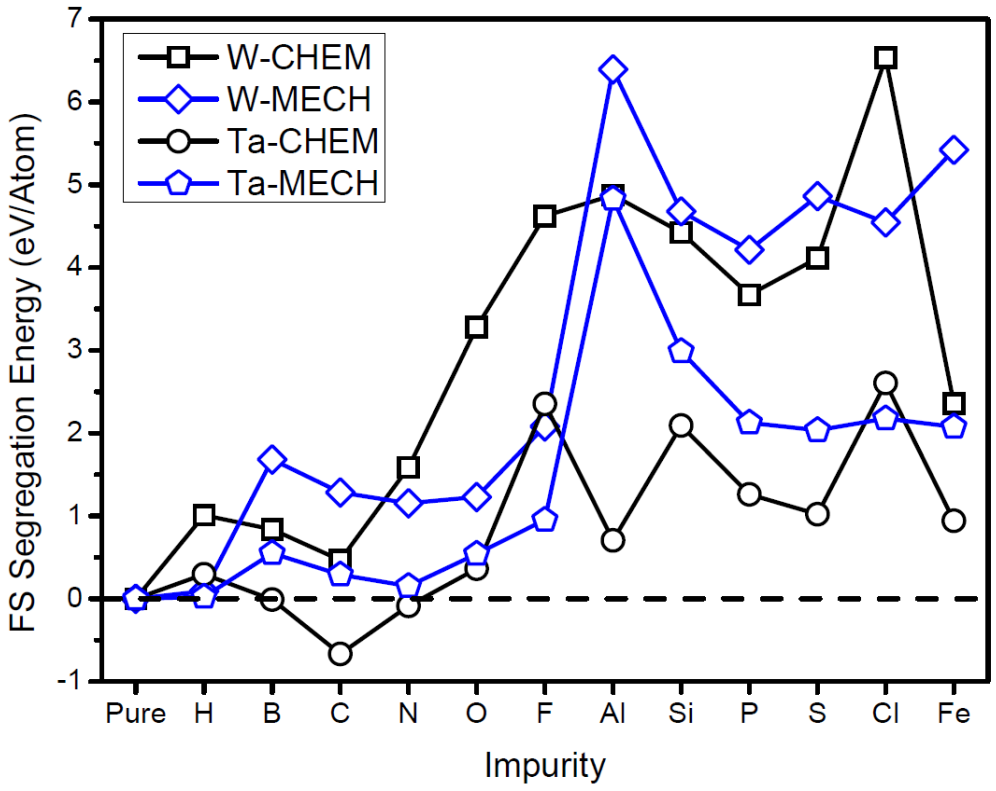

Figure 3-18: Chemical (black curves) and mechanical (blue curves) contributions of FS segregation energy of various impurities. The dashed line shows the position of zero segregation energy.

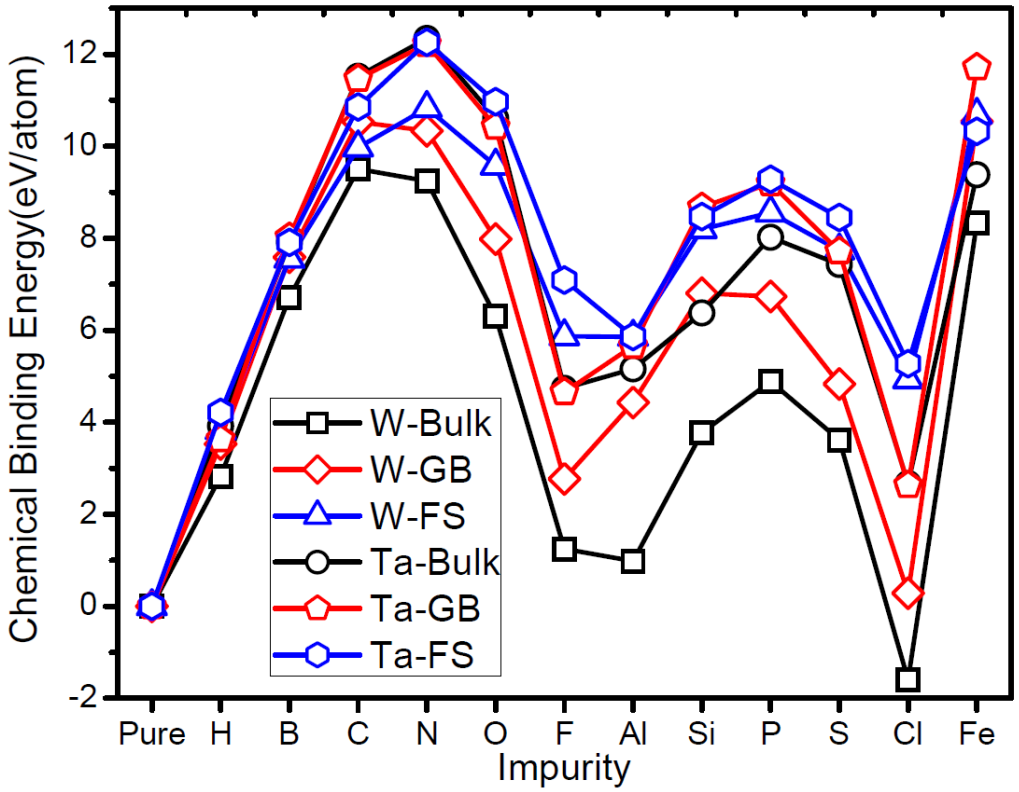

Figure 3-19: Chemical binding energy of various impurities siting at bulk, GB, and FS sites in tantalum and tungsten.

The chemical effect of various impurities is intimately related to the impurities themselves and the local atomic environment including the volume of and the host atom distribution around the interstitial site in their vicinity. It is difficult at this point to make a quantitative comparison between tantalum and tungsten. Qualitatively speaking, however, impurities that favor spatial network bonding prefer to stay in the bulk or GB sites that are surrounded by the matrix (host) atoms. These impurities have the potential to strengthen the matrix materials and usually sit in group IIIB, IVB, and VB in the Periodic Table. They are featured by the most famous element carbon. Impurities that do not favor spatial network bonding prefer to stay in the FS sites and have the potential to embrittle the matrix

materials. These impurities include but are not limited to the very high/low electronegativity elements and they usually sit in group IA, VIB, and VIIB in the Periodic Table. This is the origin of the group dependence of GB separation energy, GB segregation energy, and FS segregation energy in tantalum and tungsten. It can be further confirmed by the chemical binding energy of various impurities in both metals as shown in Figure 3-19. This figure shows that in both tantalum and tungsten, the FS binding energy of high electronegativity elements such as oxygen, fluorine, chlorine, and sulfur is always higher than their GB and bulk binding energy.

When impurity atoms form bonds with the neighboring host atoms, there is an equilibrium distance between them such that the binding energy reaches a local maximum value. Any deviation from the equilibrium distance will cause an increase in the binding energy. The actual distance in consideration is determined by the volume of the interstitial sites and also the impurity atomic size. Usually the volume of the bulk interstitial site is less than that of the GB sites and the FS sites, and the volume of the GB site is less than that of the FS site. The impurity atomic size of a low period element is less than that of a high period element. Under the circumstance that the actual volume is always smaller than that of the required volume for approaching the maximum binding energy, the binding energy usually decreases with decreasing interstitial site volume and increasing impurity atomic size. This can be confirmed by Figure 3-19 which shows that for both tantalum and tungsten, the binding energy of a specific impurity in bulk site is always lower than that of the impurity in the GB site, since the volume of the GB interstitial site is always larger than that of the bulk site. Another evidence is that the binding energy of each impurity in both the GB and the bulk site of tantalum is always higher than the corresponding binding

energy of tungsten, even for the FS site, most of the impurities have higher binding energy in tantalum than in tungsten. This is because the volume of the corresponding interstitial site in tantalum is always larger than that in tungsten since the latter has a smaller lattice constant. When the actual distance is less than the equilibrium distance, the force between the binding atoms is repulsive and increases rapidly with decreasing distance, indicating that the same amount of change of distance between binding atoms causes more binding energy change when the two binding atoms are closer. This is one possible reason why the binding energy difference of various impurities with tungsten between different sites is larger than that with tantalum. It then explains the fact that the chemical binding energy difference, GB segregation energy and FS segregation energy of tungsten are almost always higher than those of tantalum for each individual impurity.

For the elements in the same group of the Periodic Table, those with low period have smaller atomic size and thus smaller equilibrium distance from the host atoms than those with high period. This indicates that for the same interstitial site, the bonds formed between the host atoms and the low period impurity atoms are closer to equilibrium and thus have higher binding energy than the high period impurity. From Figure 3-19, we can see that, in both tantalum and tungsten, when sitting in the same kind of interstitial site, the binding energy of carbon, nitrogen, and oxygen etc. is always higher than that of silicon, phosphorus, and sulfur etc. respectively. Another example is that, both as metals, and although in different group and periods in the Period Table, the chemical binding energy of aluminum is always higher than that of iron. One possible reason for this can also be attributed to the impurity atomic size effect, since the radius of aluminum can be estimated

as ~1.43Å using the hard sphere model in FCC structure, which is clearly larger than the radius of iron estimated as ~1.24Å in BCC structure.

It is worth noting that the chemical binding energy of various impurities at all the investigated interstitial sites shows a strong correlation with the group number of the impurities in the Period Table. For the impurities in the same period, no matter where they sit, in the bulk or at the GB or on the FS site, those having the highest binding energy always have moderate group number, either group IVB or VB. This is also the origin of the group dependent behavior of GB separation energy, GB segregation energy and FS segregation energy. This behavior might be related to the ability of the impurity to form covalent bond with the host atoms through for example the *spd* hybridization.

3.4.2 Mechanical effect

Mechanical effect is the effect on the matrix materials due to the addition of impurities. It is actually the energy increase of the system or the introduction of strain energy into the matrix material due to impurity induced mechanical distortion inside the matrix. The mechanical contributions of GB separation energy, GB segregation energy and FS segregation energy for tantalum and tungsten are displayed in Figures 3-16, 3-17, and 3-18 respectively. The mechanical distortion energy due to the addition of impurities to different interstitial sites in both metals is also shown in Figure 3-20. According to Equations 3.16-3.18, the curves shown in Figures 3-16 to 3-18 are calculated based on the curves in Figure 3-20. From these figures we can see that the 12 blue curves shown thereof exhibit pretty similar trend, i.e. they all show a strong correlation to the period of the impurity in the Periodic Table. The mechanical distortion energy in both the bulk and the GB site induced by the impurity with low period is always higher than that induced by the

impurity with high period. For the binding energy difference between the GB and the FS sites, the mechanical contribution is close to zero for low period impurities, but it has considerable negative value for high period impurities. For the GB and FS segregation energies, the mechanical contribution of a low period impurity is always less than that of a high period impurity. Since the atomic size of the elements in the Period Table increases with their increasing period, it is reasonable to attribute this period dependent behavior to the atomic size effect. Impurities with large atomic sizes usually induce large mechanical distortion energy in the matrix. From Figure 3-20 we can also see that the correlation between the mechanical distortion energy and the group number of the impurities is not as strong as that between the chemical binding energy and the impurity group number. In both metals, aluminum is the one that induces the highest mechanical distortion energy among all the considered impurities. This most probably due to its large atomic size (1.43Å) compared with iron, another metallic impurity. If we compare tantalum and tungsten, we can find that, no matter where the impurities sit, the induced mechanical distortion energy of tantalum is almost always less than that in tungsten, in contrast to the mechanical binding energy. Noting that the lattice constant of tantalum is larger than that of tungsten, and thus the volume of corresponding interstitial site (bulk, GB, or FS) of tantalum is also larger than that of tungsten, it is then reasonable to attribute this difference to the interstitial site volume effect. Therefore, the mechanical distortion energy should be a strong function of the mismatch between the volume of the impurity size and that of interstitial site. This standpoint can also be supported by the fact that the mechanical distortion energy of the bulk site is higher than that of GB or FS site, since the former has the smallest site volume.

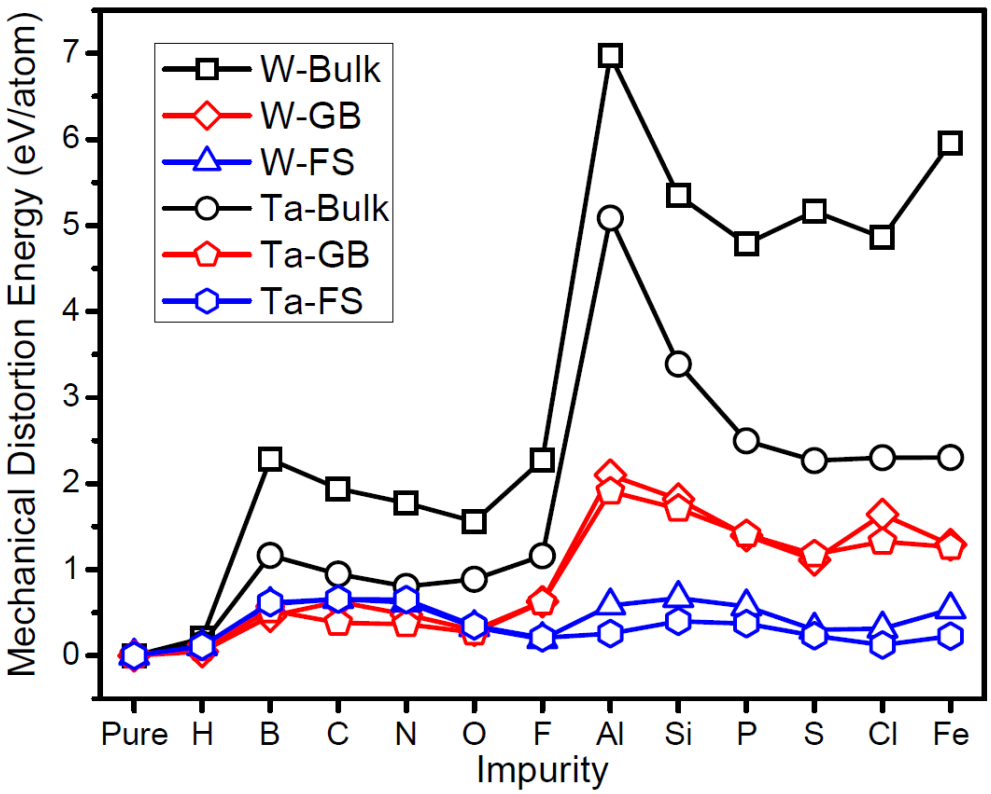

Figure 3-20: Mechanical distortion energy of tantalum and tungsten due to the addition of various impurities in bulk, GB and FS interstitial sites.

The mechanical effect is not only a strong function of the volume mismatch; it may also be related to other factors such as the topologic property of the bonds formed between the impurity atom and the host atoms, which can rearrange the host atoms surrounding the interstitial site to accommodate the impurity atom. This rearrangement will definitely contribute to the mechanical distortion energy, although the amount of which may not be as significant as that introduced by volume mismatch. However, this effect might manifest itself when the volume mismatch is not as large. For example, compared with other small impurity atoms inside tantalum, we can see from Figure 3-20 that carbon and nitrogen induce relatively low distortion energy when siting at a GB site, but they induce relatively high distortion energy when sitting at FS site. This is probably because carbon and nitrogen

prefer spatial networking bonding with the surrounding atoms, and they will try to form such topologic bond structure by rearranging the host atoms if the distribution of them is not favorable for this. Compared with GB site, FS site is less favorable to form spatial networking bond structure and thus more mechanical distortion energy is introduced during the accommodation process. The correlation between mechanical distortion energy and bond topology can also be reflected by the weak group number dependence of distortion energy induced by impurities in FS site, where the mismatch between an impurity atom and the interstitial site is not a big issue.

3.4.3 Relationship between the chemical effect and the mechanical effect

If we compare Figure 3-19 and 3-18, we can see that there is a strong correlation between the chemical binding energy and the mechanical distortion energy. A high chemical binding energy usually corresponds to a low mechanical distortion energy. For example, if the comparison is made between the GB and the bulk site, then in both metals, the chemical binding energy of each impurity in the GB site is always higher than that in the bulk site, whereas the mechanical distortion energy induced by this impurity in the GB site is always lower than that induced by the impurity in the bulk site. This correlation is also almost always true for impurities in the GB and the FS site. The only one prominent exception is the chemical binding energy of iron and the induced mechanical distortion energy in GB site of tantalum: the values of both energy terms are all higher than those in the FS site. As we have mentioned before, the binding energy of impurities with host atoms is sensitive to the local atomic environment in its vicinity, including the distance from the impurity to the host atoms and the spatial distribution of the host atoms around the interstitial site. When an impurity atom is introduced into the matrix material, the system

would accommodate itself to reach a minimum potential energy state, which will eventually generate mechanical distortion energy in the system. If the local atomic environment is in an optimum configuration such that the binding energy can have a maximum value, then the accommodation process becomes unnecessary and the induced mechanical distortion energy would reach a minimum value. However, if the local atomic environment deviates from the optimum configuration, the accommodation process will occur and will generate mechanical distortion energy. It should be noted that even the system accommodates to reach a minimum potential energy state, it is usually impossible for the chemical binding energy to revert to the maximum value; it will reach a value that is between the maximum and the value obtained without accommodation. The further away the local atomic environment is from the optimum configuration, the less the chemical binding energy is finally obtained and the more the mechanical distortion energy is induced. This is the fundamental reason that explains why high chemical effect usually points to low mechanical effect. Therefore, it is hard to decouple the chemical effect and the mechanical effect due to their strong correlations.

The correlations even exist if the comparison is made between tantalum and tungsten. From Figure 3-19 and Figure 3-20, we can see that the chemical binding energy of each impurity in the bulk site of tantalum is always higher than that of tungsten, whereas the mechanical distortion energy of the former is lower than that of the latter. This observation also holds for most of the impurities in the GB and the FS site. Only when the mechanical distortion energies induced by some impurities are close in both metals, then certain exceptions exist probably due to calculation error. In addition to indicating the correlation between the chemical and the mechanical effects, this finding also shows that

the maximum chemical binding energy in both metals should be close to each other, or at least not far away. This hypothesis is supported by the fact that the chemical binding energy of some impurities with tungsten can be close to or even higher than that in tantalum, when comparison is made between different interstitial sites. For example, the chemical binding energy of hydrogen in tungsten GB site is close to that in tantalum bulk or GB site; the chemical binding energy of fluorine in tungsten FS site is higher than that in tantalum bulk or GB site.

From the correlation between the chemical and the mechanical effects and the assumption that maximum binding energies in tantalum and tungsten are close to or at least not far away from each other, we may try to understand the differences of the GB separation energies, the GB and FS segregation energies between tantalum and tungsten in terms of volume mismatch. For a matrix system and a specific impurity, we denote the maximum chemical binding energy of this impurity in the matrix as μ_{CHEM}^{0} , the corresponding minimum mechanical distortion energy as μ_{MECH}^{0} . When the system deviates from its optimum configuration, the chemical binding energy and mechanical distortion energy are written as $\mu_{CHEM} = \mu_{CHEM}^{0} - \Delta\mu_{CHEM}$ and $\mu_{MECH} = \mu_{MECH}^{0} + \Delta\mu_{MECH}$, where $\Delta\mu_{CHEM}$ and $\Delta\mu_{MECH}$ are the reduction in the chemical binding energy and the increase in the mechanical distortion energy, respectively, due to the deviation of the matrix system from its optimum configuration. Then the total binding energy is

$$\begin{aligned} \mu &= \mu_{CHEM} - \mu_{MECH} \\ &= \mu_{CHEM}^{0} - \left(\Delta\mu_{CHEM} + \Delta\mu_{MECH}\right). \end{aligned} \tag{3.19}$$

We take the GB segregation energy as an example to interpret the effect of volume mismatch. The total binding energies in bulk and GB site are

$$\mu^{BULK} = \mu^{0}_{CHEM} - \left(\Delta\mu^{BULK}_{CHEM} + \Delta\mu^{BULK}_{MECH}\right)$$
$$\mu^{GB} = \mu^{0}_{CHEM} - \left(\Delta\mu^{GB}_{CHEM} + \Delta\mu^{GB}_{MECH}\right)$$

respectively. Then the GB segregation energy is

$$\begin{aligned}\Delta\mu^{GB}_{SEG} &= \mu^{GB} - \mu^{BULK} \\ &= \Delta\mu^{BULK}_{CHEM} - \Delta\mu^{GB}_{CHEM} + \Delta\mu^{BULK}_{MECH} - \Delta\mu^{GB}_{MECH}.\end{aligned} \tag{3.20}$$

Compared with Equation 3.16, we have

$$\begin{aligned}\Delta\mu^{I,Chem}_{GB} &= \Delta\mu^{BULK}_{CHEM} - \Delta\mu^{GB}_{CHEM} \\ \Delta\mu^{I,Mech}_{GB} &= \Delta\mu^{BULK}_{MECH} - \Delta\mu^{GB}_{MECH}.\end{aligned} \tag{3.21}$$

From the aforementioned correlation between the chemical effect and the mechanical effect, we have known that a low chemical binding energy usually means a high mechanical energy. This indicates that the increase in mechanical distortion energy $\Delta\mu_{MECH}$ increases with $\Delta\mu_{CHEM}$, the reduction in the chemical binding energy. The relationship between the chemical binding energy and the atomic distance can be illustrated using Figure 3-21. The heights of the three shaded rectangles are marked out and represent the binding energy difference between two atomic distances, the difference between which is $0.03r_0$. If the atomic distance corresponding to the lower bound value of the rectangle is the length of bond formed between the impurity and the host atoms in the GB site, and the atomic distance corresponding to the upper bound value is the length of bond formed in the bulk site, the height of the shaded rectangle actually represents the chemical contribution of GB segregation energy. Similarly, it can also be used to represent the chemical contribution of the FS segregation energy and GB separation energy. From this figure, we can see that when the distance between bonding atoms is less than the equilibrium distance, the reduction in the binding energy $\Delta\mu_{CHEM}$ increases rapidly with the decreasing distance. Such is the case for the binding energy difference shown by the

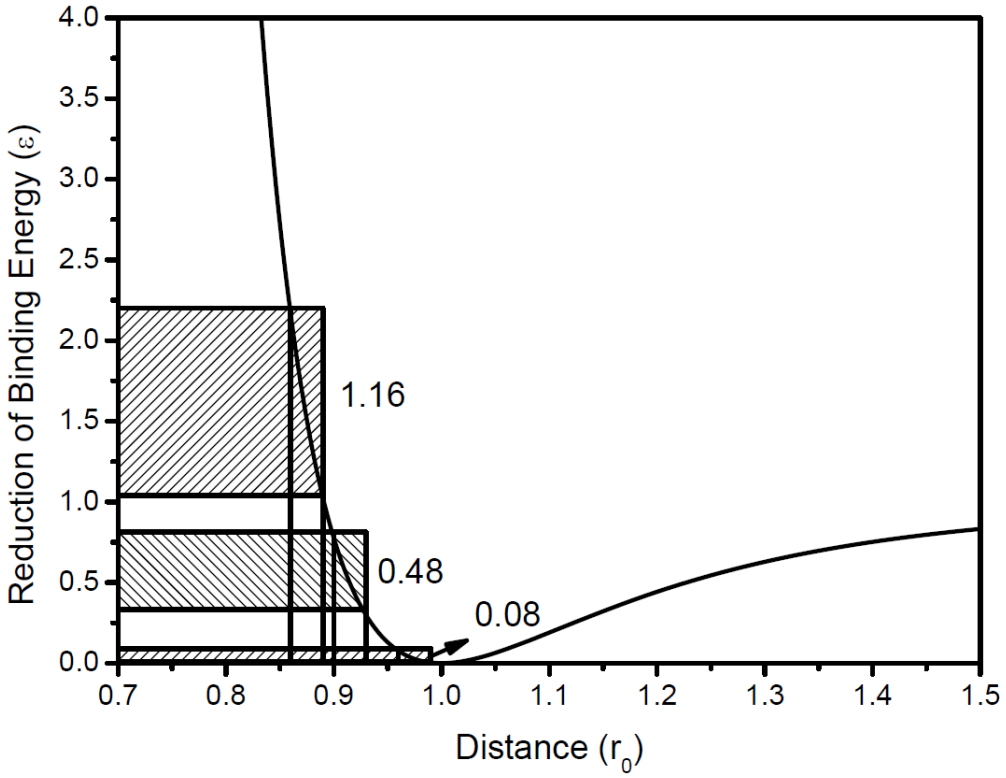

Figure 3-21: Sketch of the reduction in the binding energy versus distance curve plotted based on the Lenard-Jones (LJ) potential [200]. The unit of binding energy is the depth of the LJ potential well, and the unit of distance is the equilibrium distance.

heights of the shaded rectangles. Noting that the lattice constant of BCC tungsten is lower than that of tantalum, it is reasonable to assume that the actual bonds formed between the impurity and the tungsten atoms is shorter than that formed between the impurity and tantalum atoms. Even if the bond length difference between the GB and bulk sites formed in tungsten is smaller than that formed in tantalum, it is still reasonable to assume that the chemical effect of impurities in tungsten should be stronger than that in tantalum. Another scenario is when the bond is formed with a larger impurity atom. In this case, the equilibrium distance between the host and impurity atoms becomes larger, leading to the decrease of the relative distance, since the actual distance is determined by the matrix

materials and thus does not change much with the impurity size. This will also increase the chemical effect. From the correlation between the chemical and the mechanical effects, it is also reasonable to assume that the mechanical effect of tungsten is also higher than that of tantalum, and that induced by a large impurity is higher than that induced by a small one. These predictions actually have been confirmed by results presented in Figures 3-16 to 3-18.

Actually, even without first principles calculations but only based on intuitive judgement, we can attribute the stronger mechanical effect of tungsten to its small lattice constant and large bulk modulus which should be a consequence of its high cohesive energy and small lattice constant. For the same kind of interstitial site, the introduction of impurities will cause more volumetric strain in tungsten than in tantalum, leading to more mechanical distortion energy. However, even if the strain are the same for the two metals, due to the higher bulk modulus of tungsten, the induced mechanical distortion energy in tungsten would be still higher than that in tantalum. When the mechanical effect of the segregation energy is strong, such as when the impurity size is large, or when interstitial site (for example, in tungsten) is very small, the impurities seem to be squeezed out from the small bulk site into relatively open sites such as the GB or the FS sites. This is consistent with the fact that large dopants tend to be segregated into GB sites. It is also why McLean has used the elastic strain energy to evaluate the segregation energy in the Langmuir-McLean equation [201].

The effect of impurities on GB separation can also be estimated from the mechanical properties of the compound formed between the impurities and the host metals. The impurities that form strong compound with tantalum and tungsten have the potential to

increase their GB separation energy. For example, both boron and carbon can form strong ceramic compound with tungsten and tantalum, and they have been proved in our calculations to have beneficial effect on the GBs of both metals.

In summary, to influence the GBs, the impurity must first have a chance to segregate into the GB region which requires that it has considerable segregation energy in the matrix. To have a beneficial effect on the matrix material, the impurity must also have a positive binding energy difference between GB and FS sites. Both the segregation energy and binding energy differences are intimately related to the favorite bonding properties of the impurities with the host atoms and the volume mismatch between them. Usually almost all the elements have opportunities to segregate into GB region due to the very limited volume of the bulk interstitial site when compared with GB or FS sites, except for some extremely small elements such as hydrogen. Impurity elements that favor spatial networking bonding and have the ability to form strong covalent bond with the matrix atoms are possible GB enhancers, including group IIIB, IVB, and VB elements and some transition metals. Another requirement for GB enhancers is that the impurity should have small size and this rules out most of the elements in the main group of the Periodic Table and leaves only boron, carbon and nitrogen as the potential candidates for this effect. For impurities that belong to the transition group, the favorable segregation site is usually not interstitial but substitutional, which has relaxed requirements to the atomic size due to its larger volume when compared with the interstitial site. It should be noted that the two proposed requirements are necessary but not sufficient to improve the GB properties, since it is possible that both the matrix materials and the impurities are selective to each other (or they are inter-preclusive), and other aspects should also be taken into account.

3.4.4 Impurity concentration effect

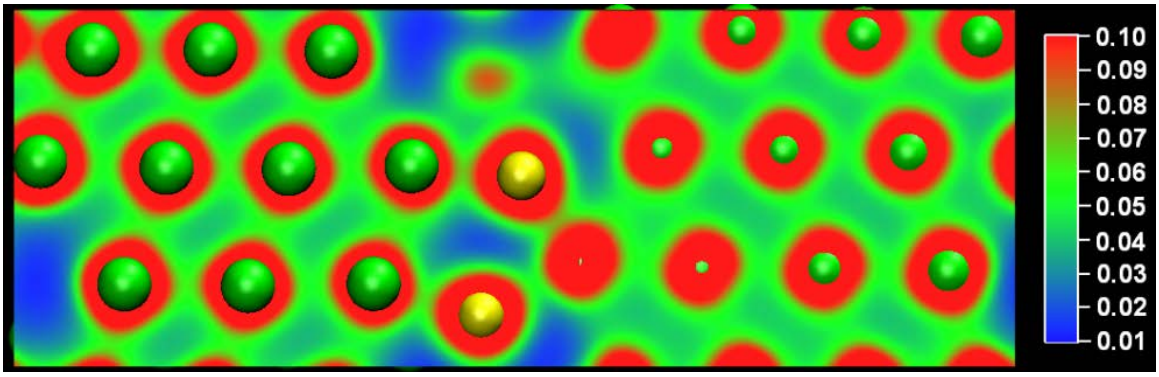

Figure 3-22: Electron density map of tungsten ∑3(111) GB contaminated with 8 substitutional sulfur atoms. The volume slice is taken along the yz plane shown in Figure 3-2. Green atoms are tungsten, and yellow atoms are sulfur.

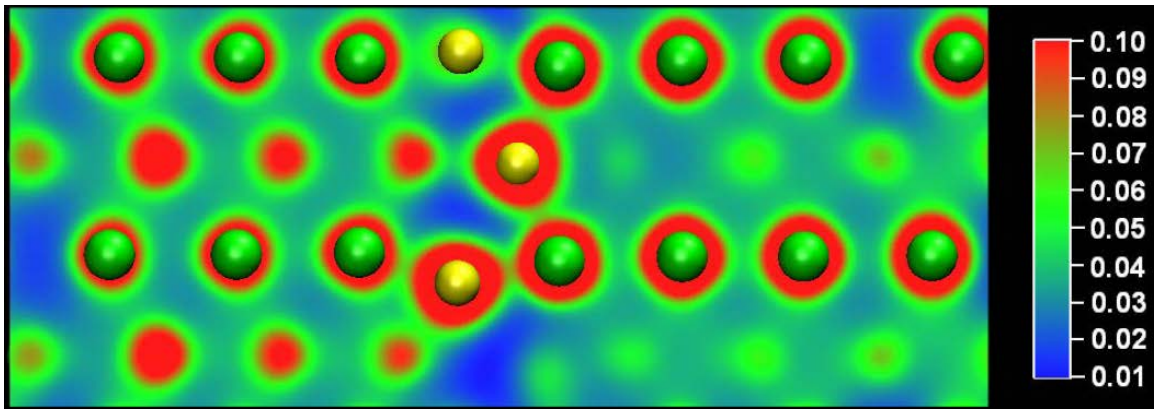

Figure 3-23: Electron density map of tantalum ∑3(111) GB contaminated with 8 substitutional sulfur atoms. The volume slice is taken along the xz plane shown in Figure 3-2. Green atoms are tungsten, and yellow atoms are sulfur.

We have figured out some possible reasons that are responsible for the beneficial or detrimental effects of the impurities on GBs based only on the interactions between the impurity and the host atoms. However, nothing has been considered regarding the interactions between the impurity atoms themselves. This should be an appropriate treatment for low concentration level where the diluted impurities are sparsely distributed

inside the matrix and are too far away from each other to have strong interactions with each other. However, when the impurity concentration level is high enough, this treatment is no longer appropriate and the understanding based on the dilute impurities becomes incomplete. So we have calculated the concentration effect of sulfur in both tantalum and tungsten. The results of calculations are provided in Figure 3-8. The results show that the GB separation energy of both tantalum and tungsten decreases monotonically with increasing concentration level, if we disregard the GB annihilation happened at some concentration level in tantalum. To understand this effect, we plot the electron density map near the GB region in Figure 3-22. It shows that the electron density between the sulfur atoms and the tungsten atoms are relatively high. However the electron density between the two sulfur atoms has become extremely low. This indicates that sulfur atoms form strong bonds with neighboring tungsten atoms, but they do not bond strongly with each other. This can also be found in tantalum according to the electron density map which is shown in Figure 3-23. If we check the equilibrium atomic configuration, we can observe that the contaminated GB structure has a shift along the x direction compared with the clean GB structure and the eight sulfur atoms are pushed apart when compared with their initial position, suggesting a strong repulsive force between the sulfur atoms. We believe this must be responsible for the weakened GBs. This repulsive effect has been identified in nickel GB segregated with sulfur atoms where the authors suggested that this short-range repulsion between the sulfur atoms plays a dominant role in reducing the GB separation energy [37], although higher concentration level of sulfur atoms also have more deleterious effect on the GBs without even considering the repulsion.

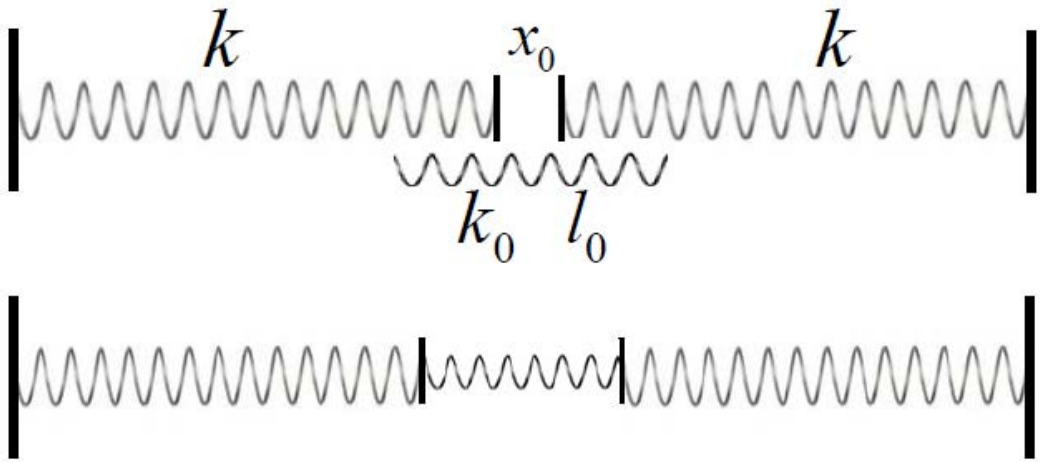

Figure 3-24: A spring model used to illustrate the effect of repulsive force between impurities. The top sketch is the unassembled state; the bottom sketch shows the assembled state. The out boundaries of the two large springs with spring constant *k* are fixed.

Figure 3-8 also shows that the GB separation energy of tungsten decreases more rapidly than that of tantalum with increasing sulfur concentration level. If we assume the repulsion between the sulfur atoms are the same for both in tantalum and tungsten, then the same amount of volume change due to the repulsion effect will result in more energy change in tungsten, since it has a smaller lattice constant and a much higher bulk modulus than tantalum. We can use a spring model to roughly show this effect. As shown in Figure 3-24, we use two springs with stiffness k to represent the matrix and its bulk modulus, another spring with stiffness k_0 and length l_0 to represent the repulsion between the sulfur atoms, and x_0 represent the interstitial size. Then after inserting the spring k_0 into to the interstitial site, the spring k is compressed by Δx. The length of the spring k_0 becomes $x_0+2\Delta x$. Therefore, the spring k_0 is compressed by $l_0-(x_0+2\Delta x)$. According to the force balance principle, we have

$$k\Delta x = k_0\left(l_0 - x_0 - 2\Delta x\right).$$

From this equation, Δx is calculated as

$$\Delta x = \frac{k_0 \left(l_0 - x_0 \right)}{k + 2k_0}.$$

The potential energy increase of the system is

$$V_{pot} = 2\left(\frac{1}{2} k \left(\Delta x \right)^2 \right) + \frac{1}{2} k_0 \left(l_0 - x_0 - 2\Delta x \right)^2 .$$

After substituting Δx with its expression and simplifying the equation, we obtain

$$V_{pot} = \frac{1}{2} k_0 \left(l_0 - x_0 \right)^2 \left(1 - \frac{2k_0}{k + 2k_0} \right). \tag{3.22}$$

We can see that the potential energy V_{pot} increases with increasing k_0, k, and l_0 and decreasing x_0. This indicates that high bulk modulus, strong repulsion, long repulsive interaction distance, and small interstitial site lead to high potential energy increase or low GB separation energy. Therefore, compared with tantalum, the high sensitivity of tungsten to the impurity concentration level can be attributed to its relatively small lattice constant and high bulk modulus. In fact, Equation 3.22 can also be used to understand the mechanical effect due to volume mismatch between the interstitial site of the host lattice and the impurity atom, if we use x_0 to represent the size of impurity atoms.

So far, we have only investigated the interactions between sulfur atoms when concentration level is high. We have known nothing about the interactions between other impurity atoms. However, we can make a reasonable hypothesis here that the impurities such as boron and carbon that can form strong spatial networking bonding with themselves and with the host atoms and thus prefer to stay inside the GB sites may not have this kind of strong repulsive effect. Instead they will eventually enhance the GB even at high concentration levels, whereas other impurities such as oxygen, fluorine and chlorine that prefer to stay in the FS sites will embrittle the GB through the strong repulsive effect

between impurities themselves when the concentration level is high. This hypothesis is actually partly corroborated by the experimental result that higher concentration level of boron in tungsten can result in more decrease in the DBTT of tungsten [14].

3.4.5 Necessity to consider dislocation properties.

Most of the work has concentrated on the effect of impurities on GB separation energy based on the argument that a high GB separation energy favors high ductility. Figure 3-8 shows that a high concentration level of sulfur impurity can make the GB separation energy of tungsten lower than that of tantalum. However, from Figures 3-7 and 3-10 we can see that for both pure and contaminated conditions by each impurity, the GB separation energy of tungsten is always higher than that of tantalum. This suggests that is only GB properties are considered, the ductility of tungsten should be better than that of tantalum based on such an argument. This, however, clearly contradicts experimental observations in the literature. This indicates that considerations of the GB properties per se are at the best incomplete and will not give a consistent explanation for the significant difference in ductility between the two metals. Therefore, we believe that based on the understanding that the ductility of a metal is controlled by the competition between dislocation activities and GB separation, the comparison on dislocation properties must be made between tantalum and tungsten to obtain a deeper and more complete understanding of this issue. More specifically, when segregated into the GB regions, the impurities will affect the GB properties by for example reducing the GB separation energy; however, the impurities should also have opportunities to segregate into the vicinity of dislocation cores and thus have a chance to influence the dislocation properties such as dislocation mobility. Therefore, we need to calculate the dislocation core segregation energy of various

impurities and their effect on the dislocation mobility in tantalum and tungsten. This is the primary content of next chapter.

3.5 Conclusion

From the above argument and the various results of calculations, and based on the role of GBs in determining the ductility of materials, we can conclude that commercial purity polycrystalline tungsten is more brittle than tantalum because tungsten has a relatively high GB segregation energy. This makes more probable for the impurities to segregate into the GB regions and thus the impurities have more chance to influence GB. Also the relatively low binding energy difference between the GB and the FS sites entails the deleterious effect from the impurities since they contribute more to the reduction in the GB separation energy of tungsten, leading to high sensitivity of tungsten to the impurity concentration level. All these adverse factors can be attributed to tungsten's relatively small lattice constant and high bulk modulus. In contrast, tantalum has a relatively low GB segregation energy, higher binding energy difference between the GB and the FS sites, and low sensitivity to the impurity concentration level due to its relatively large lattice constant and lower bulk modulus. This conclusion is drawn based on the analysis of the effect of volume mismatch between the impurity atoms and the interstitial site on the chemical binding energy and mechanical distortion energy, although other factors not discussed here might also contribute.

3.6 Deficiency of the calculations and some open-ended questions

According to Equation 3.1, to calculate the binding energy of the system, we need to know the energies of isolated atoms that are usually calculated using DFT that considers the spin polarization [202, 203] and is known as spin-DFT (SDFT), since most of the

isolated atoms have open shell configurations. However, the spin density approximation associated with the GGA exchange-correlation functional has not been implemented in CPMD. Therefore we have to calculate the energy of isolated atoms without considering electron spin, and this alternative approach will definitely underestimate the total energy of isolated atoms and introduce a systematic error to the binding energy calculation. According to Equations 3.2 and 3.4, this error will not influence the calculation of clean GB, FS, and GB separation energies, since the total energy of the isolated atoms in the two configurations have canceled each other out. This systematic error only influences the accuracy of the calculations of contaminated GB and FS energies, but does not influence the GB separation energy and comparison result of GB and FS energy between tantalum and tungsten. This is because the total energy of impurity atoms will also cancel each other out during the calculation. From Equations 3.11 and 3.12, we can see that the GB/FS segregation energies of the impurity will not be influenced by the total energy of isolated atoms either.

When we perform the geometry optimization calculations using DFT, we fix the shape and volume of the super cell, and have thus disregarded the effect of pressure, because the calculation of stress cell size optimization is computationally very expensive. This is actually a very common problem in other work in the literature. In addition, CPMD does not support stress calculation when using ultrasoft pseudopotentials. Therefore, the GBs and FSs in our DFT calculations are actually in a constrained state, which will definitely influence the calculation results.

In MD simulations, we use NPT MD to relax the sample, and have thus averted the non-zero stress problem that is almost inescapable in DFT calculations. However, we use

the EAM potentials to describe the interatomic interactions in MD simulations. Although the EAM potentials were developed from the output of first principles calculations through force matching method, approximations and simplifications have to be introduced for practical reasons and such will make MD results deviate from DFT results. This is one possible reason why the results from MD and DFT are different in our work; though both results are consistent when making comparisons between tantalum and tungsten.

When we analyze the effect of the volume mismatch on the chemical binding energy and the mechanical distortion energy, we presume that the maximum chemical binding energy of each impurity with tantalum is the same with tungsten based on Figure 3-19. Although the proposed volume mismatch mechanism is consistent, the assumption is too strong to be appropriate enough since we have actually ignored many possible effects because of some technical or practical issues. Due to the individual difference in the electronic structures between tantalum and tungsten, the maximum chemical binding energy of each impurity with the two metals should be different, although the difference might be insignificant. Similarly, due to the individual difference between various impurities, even some impurities might have the same maximum chemical binding energy with tantalum and tungsten, some others might not. The relationship between the maximum chemical binding energy of various impurities with tantalum and that with tungsten can only be elaborated if more systematic calculations are performed. Probably the best way to do this is to investigate the influence of the local atomic environment on the chemical binding by gradually changing the distance between the host atoms and the impurity atom and the spatial distribution of host atoms surrounding the interstitial site.

Following the practice in literature, we should also figure out the underlying fundamental reasons such as the orbital hybridization that leads to strong covalent bonding.

CHAPTER 4: CALCULATIONS OF DISLOCATION PROPERTIES

The plastic deformation of metals is dominated by the process of slip which occurs on the most densely packed crystallographic planes and along the directions that have the highest linear density. In BCC crystal structure, the most densely packed planes are {110} and {112} planes; the directions that have the highest linear density are <111> directions. Both {110} and {112} planes contain <111> direction. Three non-parallel {110} planes and three non-parallel {112} planes can form a three-fold symmetry configuration with <111> direction being the triad axis, different with FCC structure where only two non-parallel close packed {111} planes can contain the same <110> direction, the greatest atomic packing direction. The three-fold symmetry configuration in BCC structures makes it possible for screw dislocations to form a low-energy nonplanar configuration. The 3D core structure renders the low mobility of the screw dislocation in BCC metals at low homologous temperature. Because the edge dislocation moves much faster than the screw dislocation, the plastic deformation of BCC metals is dominated by the motion of screw dislocations through the thermally assisted double-kink formation mechanism [204].

In this chapter, we try to address the issue regarding the ductility of tantalum and tungsten in terms of the plastic deformation properties that are dominated by screw dislocations in BCC metals at low homologous temperatures ($T/T_m<0.25$) [204]. We use DFT to calculate the generalized stacking fault (GSF) energy and the Peierls energy barrier of screw dislocations and try to compare the ductility between tantalum and tungsten in

terms of the dislocation properties. Method of molecular dynamics (MD) simulations with LAMMPS is also used to prepare the atomic configurations for screw dislocations. The organization of this chapter is as follows. First, we describe the atomic configurations for GSF energy calculations and for screw dislocation calculations in the first section of this chapter; then we develop the formulas to calculate the GSF energy and the Peierls energy for dislocation movement from the output of DFT calculations. The results of calculations and simulations are given in the third section. In the fourth section, we talk about why and how impurity atoms influence dislocation mobility. Finally, we discuss the impurity sensitivity of dislocations, the influence of impurity segregation energy inside or close to the dislocation core and the issues associated with the selection of reaction path during the calculations.

4.1 Calculation set up

4.1.1 Atomic configurations

We use three atomic configurations to calculate the GSF energy with and without tetrahedral interstitial impurities, and two atomic configurations to perform screw dislocation calculations using MD simulations and DFT calculations respectively. The details about how to calculate them will be discussed in Section 4.2. In this section, we only give descriptions of these atomic configurations.

Figure 4-1 gives the atomic configuration for {110} plane GSF energy calculation. The dimensions of the orthorhombic super cell are $2\sqrt{2}a_0$, $3a_0$, and $4\sqrt{2}a_0$, respectively, along the x, y, and z directions, where the lattice constant a_0 is 3.30Å for tantalum and 3.18Å for tungsten, respectively. The white atoms near the cutting plane stand for impurity (B, C, O, and S) atoms, and will be removed if we are calculating the clean GSF energy.

The super cell consists of 96 matrix atoms and one impurity atom. Since periodic boundary conditions are applied in the three orthogonal directions, the super cell actually contains two GSF if we move the atoms in the right part of step by step along the direction shown in (b). One GSF is along the cutting plane, and the other one is shared by the super cell and its periodic image. The stacking sequence of a BCC crystal along the <110> direction is ABABAB. Therefore, a BCC crystal is symmetric about a {110} plane, which indicates that the two GSFs are identical and the GSF energy-displacement curve is symmetric.

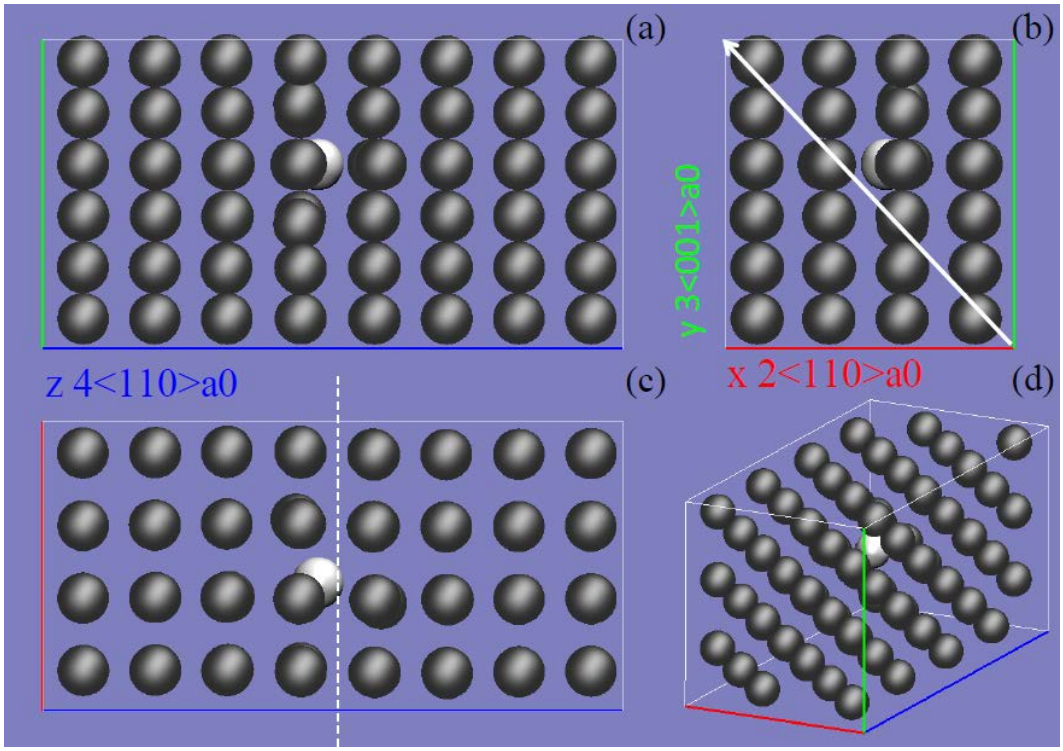

Figure 4-1: Standard views of the atomic configuration for {110} plane GSF energy calculation. The dashed line in (c) shows the position of the cutting plane along which the atoms of the right part of the crystal will be moved along the direction of the arrow shown in (b) to generate a GSF. The white atom is the tetrahedral interstitial impurity sitting in the cutting plane.

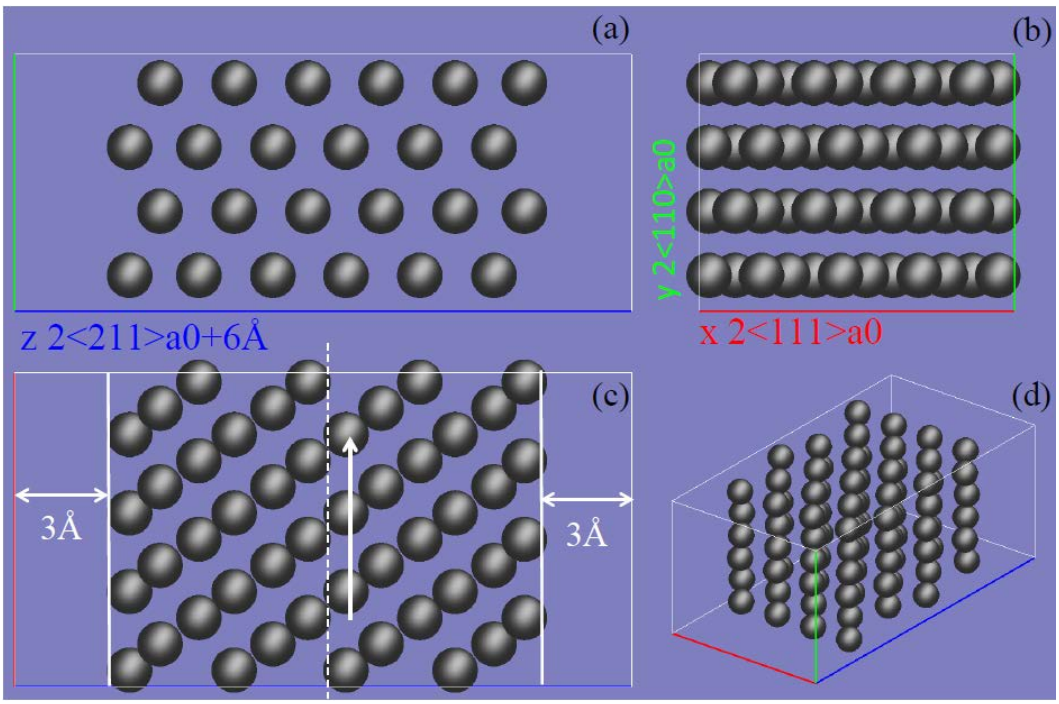

Figure 4-2: Standard views of the atomic configuration for the GSF energy calculations of clean {211} planes. The dashed line in (c) shows the position of the cutting plane along which the atoms of the right part of the crystal will be moved in the direction of the arrow near the dashed line to generate a GSF.

Figure 4-2 gives the atomic configuration for the GSF energy calculations of clean {211} plane. The dimensions of the super cell in the x and y directions are $2\sqrt{3}a_0$ and $2\sqrt{2}a_0$, respectively. The stacking sequence of a BCC crystal along a <211> direction is ABCDEF, indicating the crystal is asymmetric about the {211} plane. Therefore, if we apply boundary conditions in the z direction that is similar to that used in Figure 4-1, when shifting the atoms in the right part of the crystalprogressively along the specified direction, the two generated GSFs are not identical, and the corresponding GSF energy-displacement curve is also asymmetric. This is a typical feature of the twin plane GSF energy and it makes it impossible to derive the GSF energy, since the two different GSF energies are coupled with each other. So we insert a space of 3Å between the outmost atomic plane and

the super cell boundary in the z direction so as to create an FS. We then apply periodic boundary conditions in all three directions, resulting in a super cell with a length of $2\sqrt{6}a_0 + 6\text{Å}$ in the z direction that contains only one GSF and two FS inside, thus removing the coupling effect.

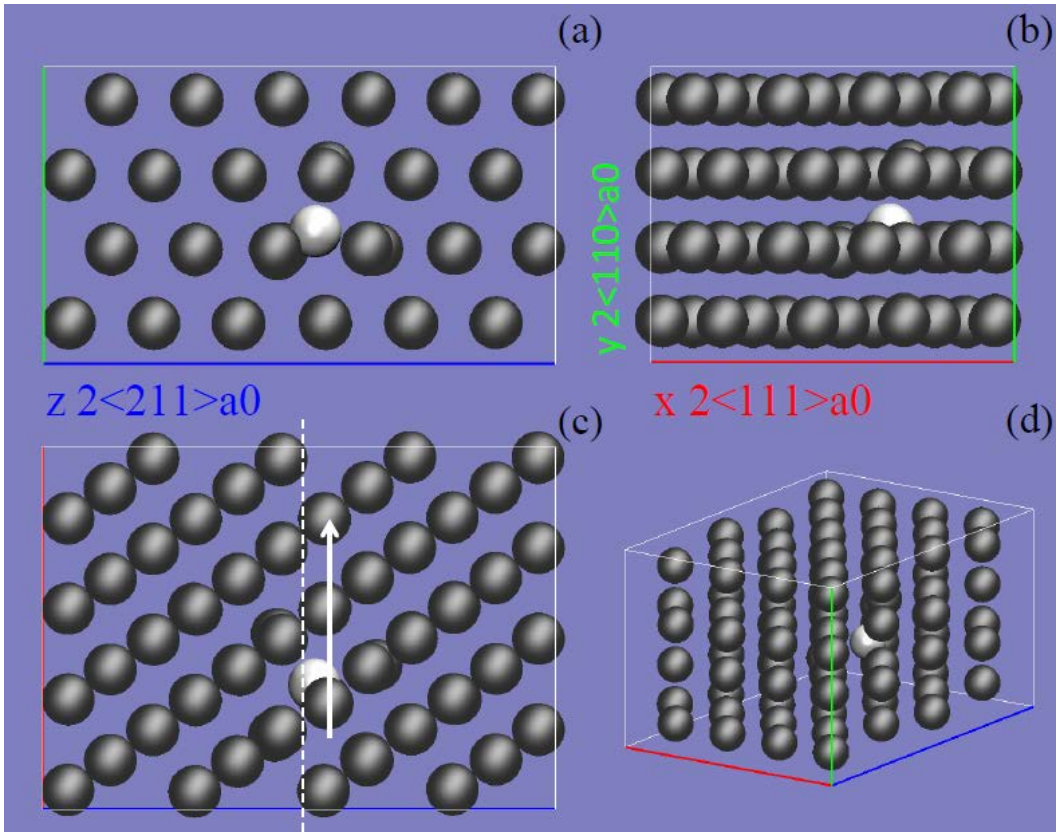

Figure 4-3: Standard views of the atomic configuration for the GSF energy calculations of contaminated {211} planes. The dashed line in (c) shows the position of the cutting plane along which the atoms of the right part of the crystal will be moved in the direction of the arrow near the dashed line to generate a GSF.

Figure 4-3 gives the atomic configuration for the GSF energy calculations of contaminated {211} planes. The dimensions of the super cell in the x and y directions are the same as the one shown in Figure 4-2. But we do not introduce an FS in this super cell,

so the dimension in the z direction is $2\sqrt{6}a_0$. Periodic boundary conditions are applied in all three directions. Therefore, after moving the atoms of the right part of the crystal in the specified direction shown in Figure 4-3 (c), we create two GSFs: the first one is the contaminated GSF in the middle of the super cell; the second one is a clean GSF and is shared by the super cell and its periodic image in the z direction.

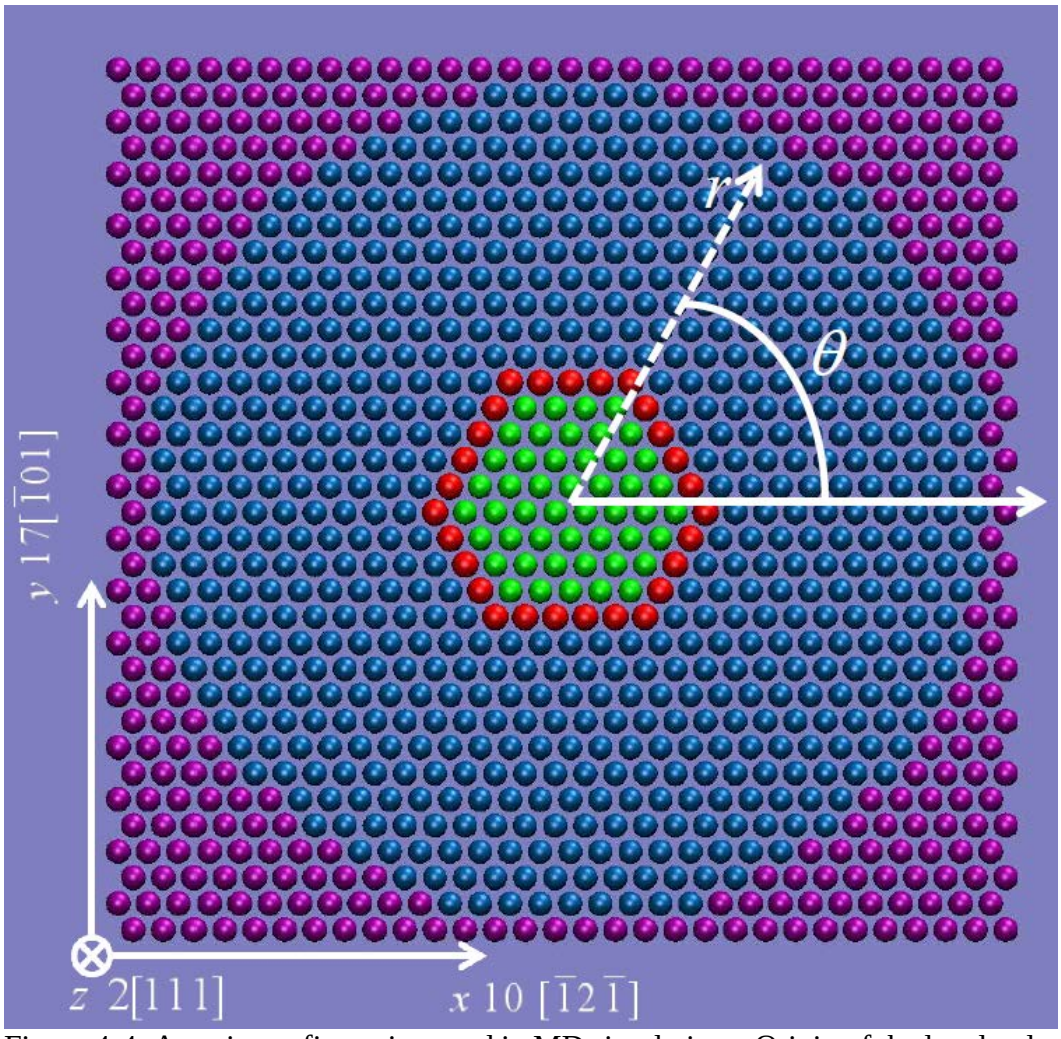

Figure 4-4: Atomic configuration used in MD simulations. Origin of the local polar coordinate system is the position of the core of the screw dislocation. The computational cell contains 4080 atoms and is divided into four regions. The purple atoms are fixed during the MD simulations, while the rest of the atoms are fully relaxed.

Figure 4-4 gives the atomic configuration for the preparation of the core structure of a screw dislocation using MD simulations. We first create a single crystal slab, and then we displace all the atoms in the z direction according to the displacement field [100] determined by theory of elasticity,

$$u_z(r,\theta) = b\frac{\theta}{2\pi}, \tag{4.1}$$

where the polar coordinate (r,θ) is defined in Figure 4-4. In this case, the computational cell is divided into four regions. The purple atoms are fixed in the MD simulations; the blue atoms are in the transition area between MD simulations and DFT calculations; the red and green atoms are taken out after MD calculation as the atomic configuration for DFT calculations, as shown in Figure 4-5. Periodic boundary conditions are applied in the z direction to simulate an infinitely long screw dislocation.

Figure 4-5 displays the atomic configurations used in DFT calculations. A monoclinic super cell is used in this case. The base unit vectors are $C_1 = 5\left[01\bar{1}\right]a_0$, $C_2 = 5\left[\bar{1}10\right]a_0$, and $C_3 = 2[111]a_0$, where a_0 is the lattice constant. Periodic boundary conditions are applied in all three directions. However, the outmost red atoms are fixed during the calculations for geometry optimization, and only the green atoms inside the super cell are allowed to move. The screw dislocation is right handed and has an easy core structure, which is more stable than a hard core [114]. When calculating the properties of the contaminated dislocation core, we insert a tetrahedral interstitial impurity atom into a position in the vicinity of the dislocation core as indicated by the white spot in Figure 4-5 (a), since our pilot calculations have shown that the center of the screw dislocation core is

not a stable site for the impurity atom and it will eventually push the impurity into its vicinity.

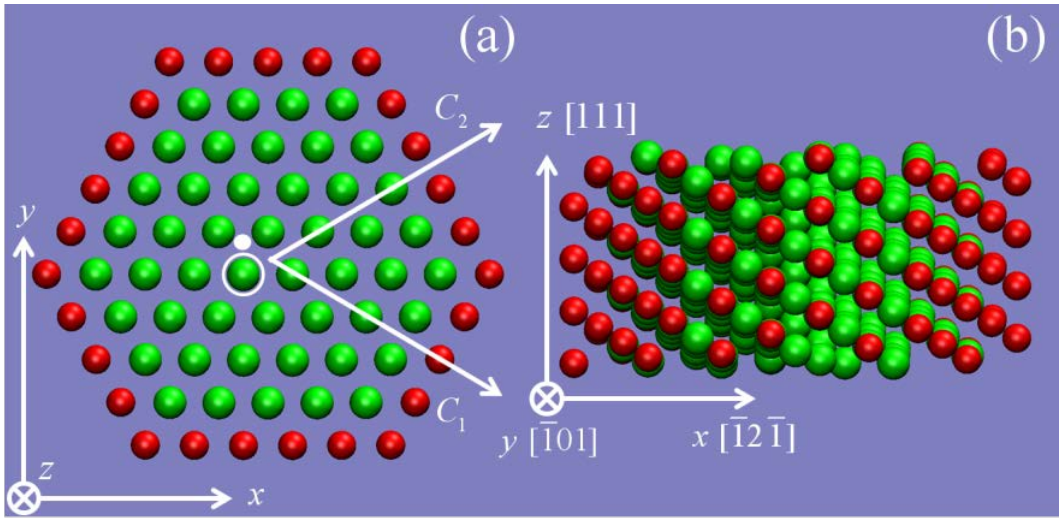

Figure 4-5: Atomic configuration of a right-handed screw dislocation. (a) the xy plane, and the (b)xz plane. The red atoms are fixed during DFT calculations. The green atoms are fully relaxed. C_1 and C_2 are the base vector of the monoclinic super cell used in DFT calculations. The white spot indicates the position of an interstitial impurity atom (B, C, O, and S). The row of atoms marked by the white circle will be marched out of the page to simulate the movement of a straight dislocation.

4.1.2 DFT and MD settings

The DFT settings for the calculations of the GSF energy and Peierls energy barrier are nearly the same with those used in the GB separation energy calculations. They include the cutoff energy of 503eV for the plane wave basis set, the GGA(PW91) exchange-correlation functional, the Vanderbilt ultrasoft pseudopotentials, the convergence criterion of 0.026eV/Å for geometry optimization and the adaptive gradient criterion. The difference from the previous settings includes some constraints and manipulations imposed on some atoms in the calculations described herein. For the GSF

energy calculations, we first relax the samples shown in Figures 4-1, 4-2, and 4-3, to their minimum potential configuration through geometry optimization. Then we gradually move the right portion of the sample in the <111> direction as shown by the arrow by a distance of b/20 each step, where b is Burgers vector. After each movement, we relax the sample to its minimum potential through geometry optimization calculations, in which all the atoms are only allowed to move in the direction that perpendicular to the cutting plane. However, the impurity atom, if present, can move in any direction. We make 20 movements, resulting in a total displacement of b, which is one periodic length in the <111> direction for the BCC crystals.

For the Peierls energy calculations, we first relax the sample obtained from MD simulations to its minimum potential energy state with the outmost atoms fixed. Then we gradually march the marked row of atoms (marked by the white circle in Figure 4-5 (a)) out of the page by a distance of b/60 for each step. After each movement, geometry optimization is performed to obtain the structure of minimum potential, in which all the marched atoms are only allowed to move in the direction perpendicular to dislocation line. The total displacement is b/3. This corresponds to the movement of a straight dislocation.

As indicated by Equation 4.1 which has been developed from the theory of elasticity, the displacement field of a screw dislocation is only a function of θ. This is true when the atoms are far from the dislocation core, but not so when the atoms are close to the core of the dislocation. When investigating the properties of the dislocation core, people usually use the elasticity solution to create the initial displacement field. They then use atomistic simulations or first principles calculations to optimize the core structure with periodic or fixed boundary conditions. The former are applied to simulation cells

containing screw dislocation dipoles or quadrupoles [102, 134]. The latter are applied to single screw dislocation core with the elasticity solution as boundary conditions [105, 115]. It is appropriate if the simulation cell is large enough and the boundaries are far from the dislocation core. However, it is not good enough for small simulation cells, such as those that used in DFT calculations. One way to improve the conditions is to use the so-called flexible boundary condition method which updates the boundary atomic positions according to the Greens function solution and at the same time employs the interatomic forces from DFT calculations [112, 205]. Another possible way is the multi-scale modeling in which the boundary atomic positions are determined by theory of elasticity. The atomic positions around the dislocation core are modeled using DFT calculations, while the atomic positions in the region between the boundary and the dislocation core are modeled by MD simulations [206, 207]. In our model shown in Figure 4-4, we first create a screw dislocation structure based on the solution of the theory of elasticity. We then minimize the potential energy of the system with the purple atoms fixed as the boundary region using the aforementioned MD code LAMMPS. After MD simulation, the red and green atoms are taken out as the input for DFT calculations. In other words, we use the result of the theory of elasticity to model the boundary for MD simulations, and the result of MD simulations to model the boundary of DFT calculations. This scheme first appears similar to the multi-scale modeling, but as a matter of fact it is essentially different. This is because we have not considered the interaction energy between different regions which is indispensable in multiscale simulations.

During the potential energy minimization of the system, we iteratively adjust the atomic positions until the maximum force between them is less than 10^{-8} eV/Å. The EAM

potential developed by Li and co-workers [195] is used to describe the interatomic interactions for tantalum and the Finnis-Sinclair potential [103, 208] is used to describe the interatomic interactions between tungsten atoms.

4.2 Calculations of the GSF energy and the Peierls energy

The GSF energy is defined as the energy difference per unit GSF area between the reference configuration which is a perfect, ideal single crystal and the configuration that contains a GSF due to the shifting of the atoms of one part of the crystal in the reference configuration. For the clean {110} plane GSF shown in Figure 4-1, after movement along the cutting plane, two identical GSFs are created in the super cell. Then the GSF energy of the clean {110} plane is

$$\gamma_{\{110\}}(x) = \frac{E_{GSF}^{DFT}(x) - E_{SGL}^{DFT}}{2A}, \tag{4.2}$$

where $x \in (0, b)$ is the displacement along the {111} direction; A is the area of the GSF; $E_{SGL}^{DFT} = E_{GSF}^{DFT}(0)$ is the total energy of the reference configuration (of the perfect, ideal single crystal); $E_{GSF}^{DFT}(x)$ is the total energy of the configuration after moving the right part of the single crystal along the specified direction by a distance of x. When an impurity atom is included in the calculations, the two GSFs are not identical any more. One of the GSFs becomes contaminated and the GSF energy is calculated using the following formula

$$\gamma_{\{110\}}^{I}(x) = \frac{E_{GSF}^{DFT,I}(x) - E_{SGL}^{DFT,I}}{A} - \gamma_{\{110\}}(x), \tag{4.3}$$

where the super script I represents the impurity atom.

For the clean {211} plane GSF shown in Figure 4-2, only one GSF is created inside the super cell after the movement. Then the GSF energy of the clean {211} plane is

$$\gamma_{\{211\}}(x) = \frac{E_{GSF}^{DFT}(x) - E_{SGL}^{DFT}}{A}. \tag{4.4}$$

When we were first calculating the GSF energy of a {211} plane, we did not realize that the asymmetry of this plane will introduce two different GSFs when half of the atoms in the super cell are displaced. So we simply use the configuration shown in Figure 4-3 to do the calculation. Since the two GSFs are not identical, it is impossible to calculate the individual GSF energy based only on the energy difference between the reference and the displaced configurations, because in this case the GSF energy is in fact the sum of the two GSF energies. Due to limited time, it is impossible to recalculate all the GSF energies using the super cell shown in Figure 4-2. We have therefore corrected our results by introducing a makeup strategy and this of course leads to an unnecessary complexity. For convenience, we use $\mathrm{GSF}\left(\mathrm{A}\middle|\uparrow \mathrm{B}\right)$ to represent the GSF generated between atomic layers A and B by displacing atomic layers on the right in the positive direction indicated by the upward arrow. Because the stacking sequence of the {211} planes is ABCDEF, then $\mathrm{GSF}\left(\mathrm{A}\middle|\uparrow \mathrm{B}\right)$, $\mathrm{GSF}\left(\mathrm{B}\middle|\uparrow \mathrm{C}\right)\ldots\mathrm{GSF}\left(\mathrm{F}\middle|\uparrow \mathrm{A}\right)$ are identical, and have the same GSF energy as a function of the displacement. $\mathrm{GSF}\left(\mathrm{A}\middle|\uparrow \mathrm{B}\right)$ and $\mathrm{GSF}\left(\mathrm{A}\downarrow\middle|\mathrm{B}\right)$ are also identical. The stacking sequence of the atomic configuration shown in Figure 4-3 is ABCDEF|ABCDEF, here "|" represent the cutting plane. After we displace the right part of the sample upward, the GSF in the middle of the super cell is $\mathrm{GSF}\left(\mathrm{F}\middle|\uparrow \mathrm{A}\right)$, whereas the one shared with its periodic image is $\mathrm{GSF}\left(\mathrm{F}\uparrow\middle|\mathrm{A}\right)$ or $\mathrm{GSF}\left(\mathrm{F}\middle|\downarrow \mathrm{A}\right)$. If the energy of the middle GSF is $\gamma_{\{211\}}(x)$, the one for the shared GSF is actually $\gamma_{\{211\}}(-x)$. Note that $\gamma_{\{211\}}(x)$ is a periodic function with the period of the Burgers vector b, i.e. $\gamma_{\{211\}}(x+b)=\gamma_{\{211\}}(x)$. Then we have

$$\gamma_{\{211\}}(-x)=\gamma_{\{211\}}(b-x), \tag{4.5}$$

where $\gamma_{\{211\}}(x)$ can be calculated using Equation 4.4 from the configurations shown in Figure 4-2. Since the configuration shown in Figure 4-3 contains one contaminated $\mathrm{GSF}\left(\mathrm{F}\middle|\uparrow \mathrm{A}\right)$ in the middle and one clean $\mathrm{GSF}\left(\mathrm{F}\middle|\downarrow \mathrm{A}\right)$, the contaminated GSF energy is then

$$\gamma_{\{211\}}^{I}(x) = \frac{E_{GSF}^{DFT,I}(x) - E_{SGL}^{DFT,I}}{A} - \gamma_{\{211\}}(b-x). \qquad (4.6)$$

This is the formula we used to correct the results.

The calculation of the Peierls energy of a screw dislocation is very simple. Assume the total energy of the equilibrium configuration shown in Figure 4-5 is $E_{SCREW}^{DFT}(0)$, and the total energy of the displaced configuration by a distance of x in the [111] direction is $E_{SCREW}^{DFT}(x)$, then the Peierls energy per unit length of screw dislocation is

$$\Delta E(x) = \frac{E_{SCREW}^{DFT}(x) - E_{SCREW}^{DFT}(0)}{N}, \qquad (4.7)$$

where N is the length of the screw dislocation with the unit of the Burgers vector b. It equals 4 in our configuration.

4.3 Results of calculations

4.3.1 GSF energy

The {110} plane GSF energy of tantalum with and without the impurity is calculated using Equation 4.2 and 4.3. The results of calculations are shown in Figure 4-6. From the results we can see that the clean {110} plane GSF energy is symmetric with respect to the displacement of 0.5b. However, the addition of an impurity atom into the GSF breaks the symmetry. All the impurities decrease the pure shear energy barrier. Among all the impurity atoms investigated, sulfur has the most prominent softening effect,

and oxygen has the least effect. At the beginning of the pure shear, the carbon contaminated GSF energy curve first goes down a little bit, and then increases with increasing shear displacement. At the end of the shear, the carbon and oxygen contaminated GSF energy curves do not return to the zero level, but instead rise to a higher value. These findings indicate that the introduction of impurity atoms not only breaks the symmetric nature of the GSF energy of a pure and perfect crystal, but also breaks the periodicity, or at least change the period of the GSF energy curve.

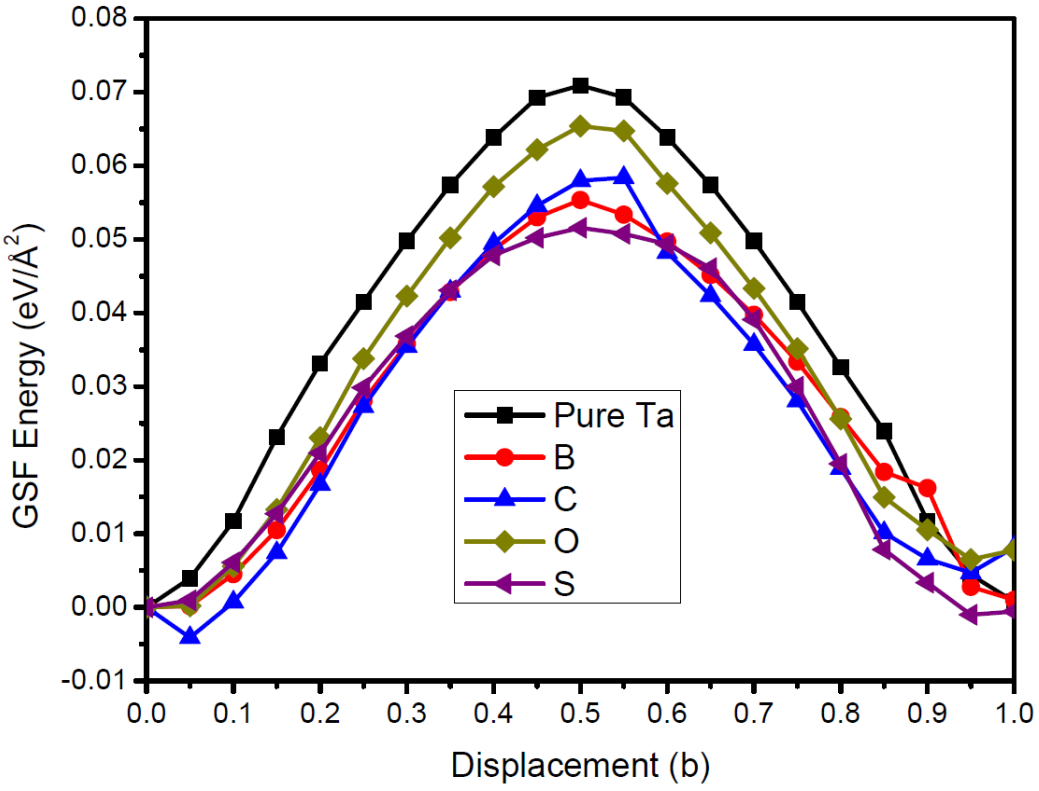

Figure 4-6: The {110} GSF energy curves of tantalum with and without an impurity atom near the cutting plane based on the DFT calculations (see Figure 4-1 for the atomic configurations for the DFT calculations).

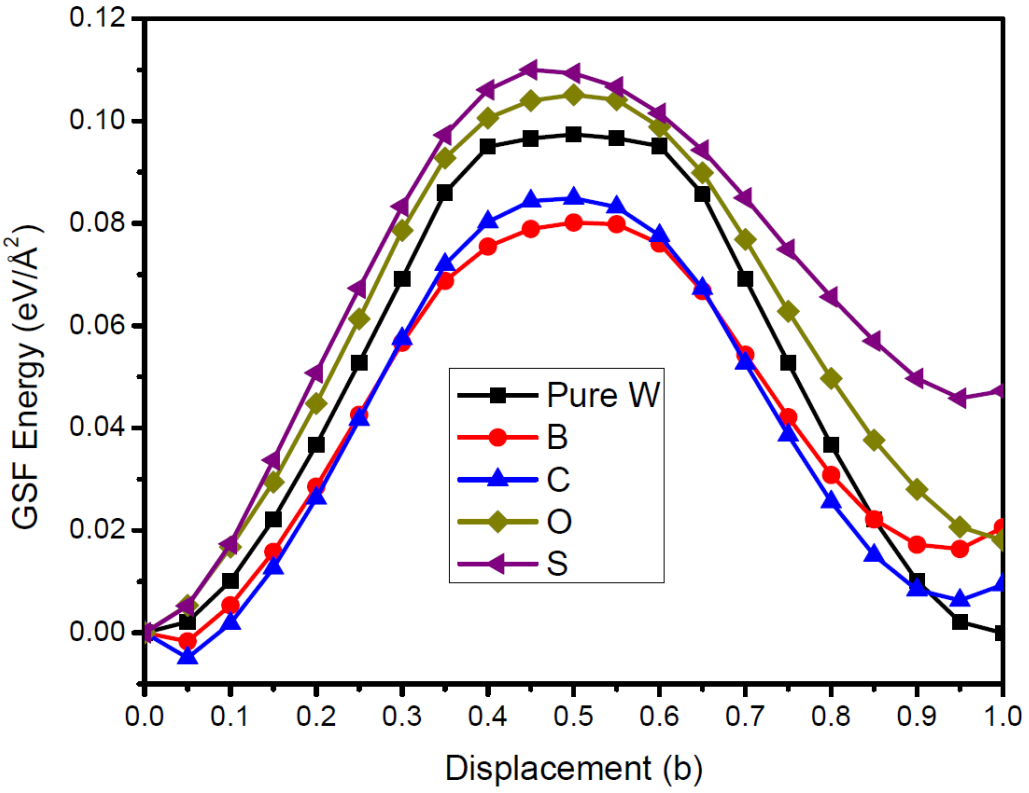

Figure 4-7: The {110} GSF energy curves of tungsten with and without an impurity atom near the cutting plane based on the DFT calculations (see Figure 4-1 for the atomic configurations for the DFT calculations).

The {110} plane GSF energy of tungsten with and without an impurity atom is shown in Figure 4-7. Bearing a close resemblance to the results for tantalum, the clean GSF energy curve of tungsten is also symmetric, and the addition of an impurity atom breaks the symmetry of the curve. However, different from tantalum, among the impurities investigated, only boron and carbon decrease the pure shear energy barrier significantly, while oxygen and sulfur increase the energy barrier instead. When compared with tantalum, the lowest energy barrier of tungsten is still higher than the highest energy barrier of tantalum. The effects of boron and carbon on the GSF energy are similar. The contaminated GSF energy curves of both impurities decrease slightly at the beginning of

the shearing process, and then increase slightly at the end of pure shear process. For tungsten, none of the contaminated GSF energy curves returns to the zero level, indicating the change of periodicity of the GSF energy in this metal.

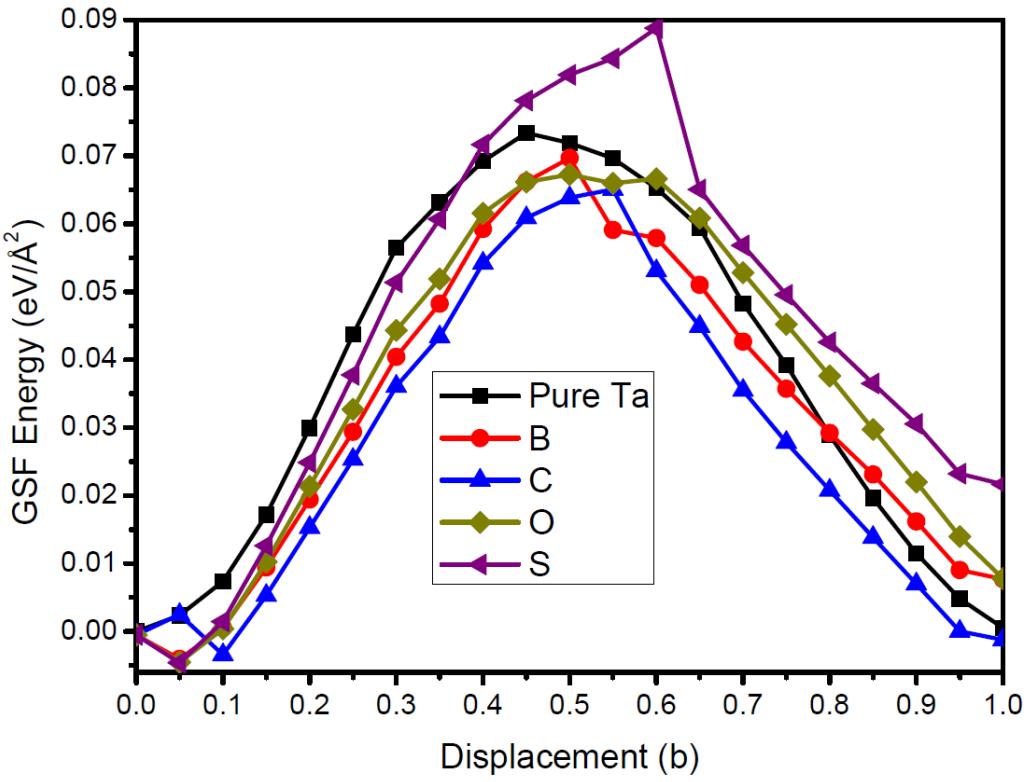

Figure 4-8: The {211} GSF energy curves of tantalum with and without an impurity near the cutting plane based on DFT calculations (see Figure 4-2 for the atomic configurations for DFT calculations).

The {211} plane GSF energy of tantalum with and without an impurity is calculated using Equations 4.4 and 4.6 with input from DFT calculations. The results of calculations are presented in Figure 4-6. It is found that the clean {211} plane GSF energy curve is not symmetric, unlike the results for the {110} planes. This is because, as we have pointed out previously, the {211} plane is not a symmetric plane for a BCC crystal. This is

a general feature of twin plane in the BCC lattice, similar to the {111} plane in an FCC crystal. Among the impurities investigated in this work, the addition of boron, carbon, and oxygen decreases the pure shear energy barrier, whereas only sulfur increases the energy barrier significantly. Analogous to the {110} plane GSF energy of tantalum (see Figure 4-6), the impurity atoms change the periodicity of the {211} plane GSF energy curve.

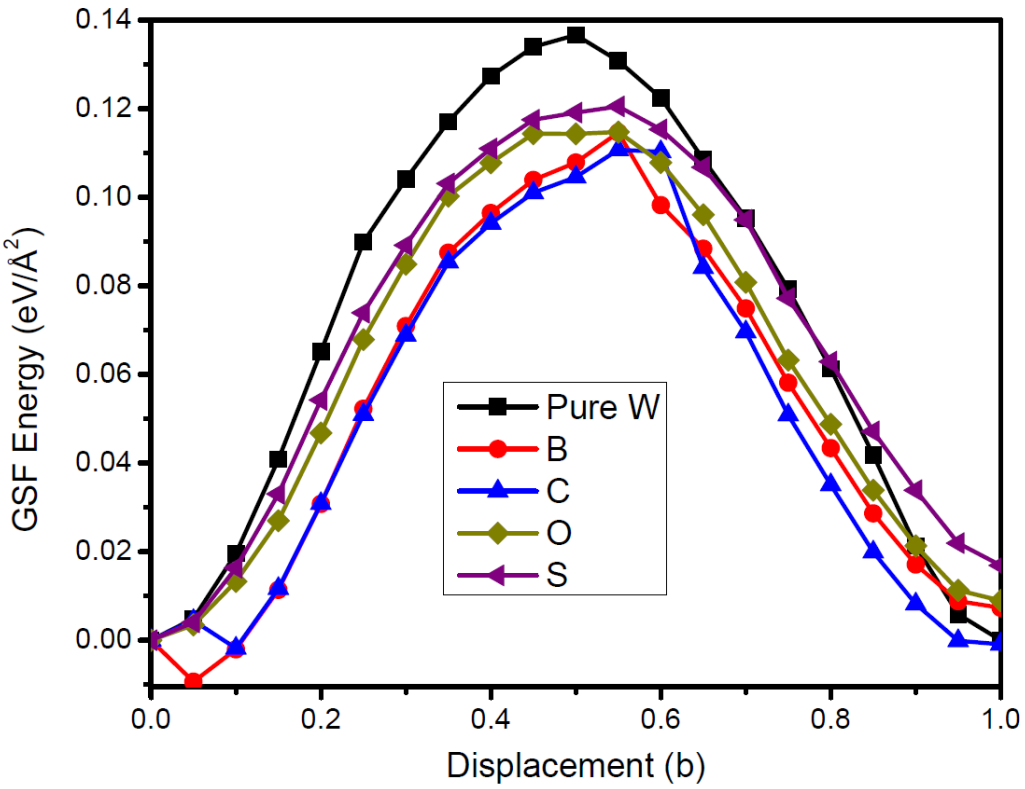

Figure 4-9: The {211} GSF energy curves of tungsten with and without an impurity near the cutting plane based on DFT calculations (see Figure 4-2 for the atomic configurations for DFT calculations).

Figure 4-9 shows the {211} plane GSF energy curves of tungsten with and without impurities based on DFT calculations. Similar to the results for tantalum, the clean {211} plane GSF energy curve of tungsten is not symmetric. The addition of all kinds of

impurities investigated in this work decreases the pure shear energy barrier. Analogous to what has been observed in Figure 4-7, the effects of boron and carbon resemble each other, whereas oxygen and sulfur have similar effect. Compared with tantalum, the lowest GSF energy barrier of tungsten is higher than that of the highest of tantalum, which is also true for the {110} plane GSF energy curves of the two metals.

From the results presented in Figures 4-6 to 4-9, it is also observed that boron and carbon always have a good, if not the best, softening effect on the pure shear along both {110} and {211} planes for both tantalum and tungsten; whereas the effects of oxygen and sulfur depend on the slip plane and the matrix material. For example, on the one hand, sulfur in tantalum has the best softening effect on the {110} plane GSF energy, but the best hardening effect on the {211} plane GSF energy. On the other hand, sulfur in tungsten has the best hardening effect on the {110} plane GSF energy, but the worst softening effect on {211} plane GSF energy.

4.3.2 The core structure of screw dislocations in BCC metals

The screw dislocation core structure of a BCC lattice is usually visualized using the differential displacement (DD) map first proposed by Vitek [104, 209]. This map is dedicated to showing the relative displacement field of atoms in a periodic crystal after deformation. It displays the projection of the atoms in a period of atomic layers on a two dimensional plot where atoms from different layers are marked differently. The change of distance between neighboring atoms relative to the ideal crystal, or the so-called differential displacement is described using an arrow whose midpoint coincides with that of the line that connect the two neighboring atoms. The length of the arrowed line is proportional to the value of the differential displacement. If the direction of the

displacement is perpendicular to the atomic layer, the arrow points from one atom to its neighbor. Otherwise if the displacement is inside the atomic layer, the arrow points to the

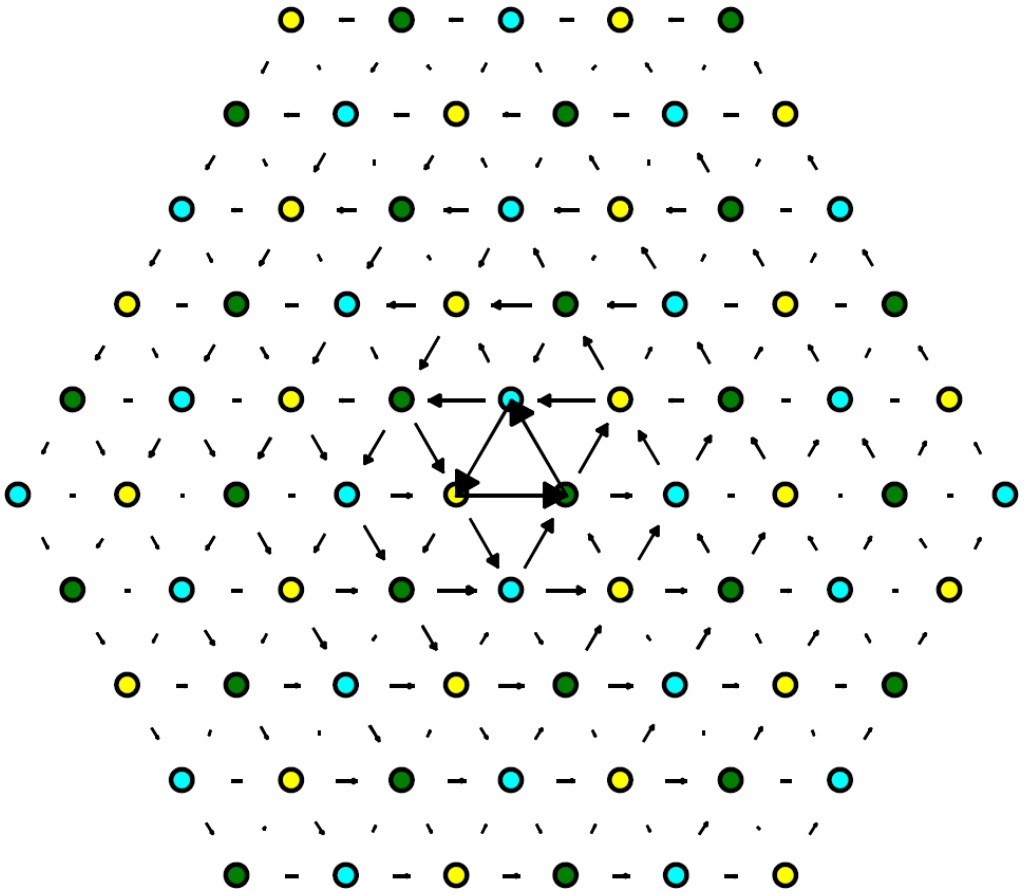

Figure 4-10: Differential displacement map of ½a<111> screw dislocation core structure in tungsten after geometry optimization.

direction of the displacement. Figure 4-10 gives the differential displacement map of ½a<111> screw dislocation core structure in tungsten. The longest arrow that connects two neighboring atoms inside the dislocation core corresponds to a displacement of b/3, where b=½a<111> is the Burgers vector of screw dislocations in the lattice. Obviously, Figure 4-10 shows a non-degenerate symmetric screw dislocation core which can also be

observed in tantalum according to the DD map not shown here. This result is in agreement with that from other DFT calculations [102, 113, 134] and some MD simulations [105, 109] of BCC metals. It is also consistent with the prediction from the Duesbery-Vitek criterion [105] which states that the screw dislocation core is symmetric if $\gamma(b/3) > 2\gamma(b/6)$, and asymmetric if otherwise. In this criterion, $\gamma(b/6)$ and $\gamma(b/3)$ are the {110} plane GSF energy at displacement of $b/6$ and $b/3$ respectively. In fact, according to the {110} plane GSF energy curves of tantalum and tungsten shown in Figure 4-6 and 4-7 respectively, $\gamma(b/6) = 0.026$ and $\gamma(b/3) = 0.055$ for tantalum, and $\gamma(b/6) = 0.027$ and $\gamma(b/3) = 0.08$ for tungsten. Therefore, $\gamma(b/3) > 2\gamma(b/6)$ holds for both metals, suggesting that it should be energetically more favorable for the core to spread into six identical <112> directions, resulting in a symmetric core structure.

4.3.3 Dislocation core segregation energy

The dislocation core segregation energy of various impurities in tantalum and tungsten are calculated using DFT. The results of calculations are provided in Figure 4-11. It can be seen from the results of DFT calculations that the impurity segregation energies of various impurities follow trend a similar to the GB segregation energy shown in Figure 3-14 of the previous chapter. Almost all the investigated impurities have a positive value of segregation energy in both metals. Therefore those impurities are likely to be segregated from bulk, defect free region into the vicinity of dislocation core, leading to a change in the dislocation properties. However, hydrogen stands out as an exception in that it has a negative value of dislocation core segregation energy in tantalum, indicating that the bulk, dislocation free region is the energetically most favorable site for hydrogen when compared with the GB and dislocation core interstitial sites. For impurities in the same

group, the core segregation energy of the impurity with a high period is always higher than that of the impurity with a low period, indicative of strong correlation with the period of impurities in the Periodic Table. Like the GB and FS segregation energies, the dislocation core segregation energy of each impurity in tungsten is always higher than that in tantalum.

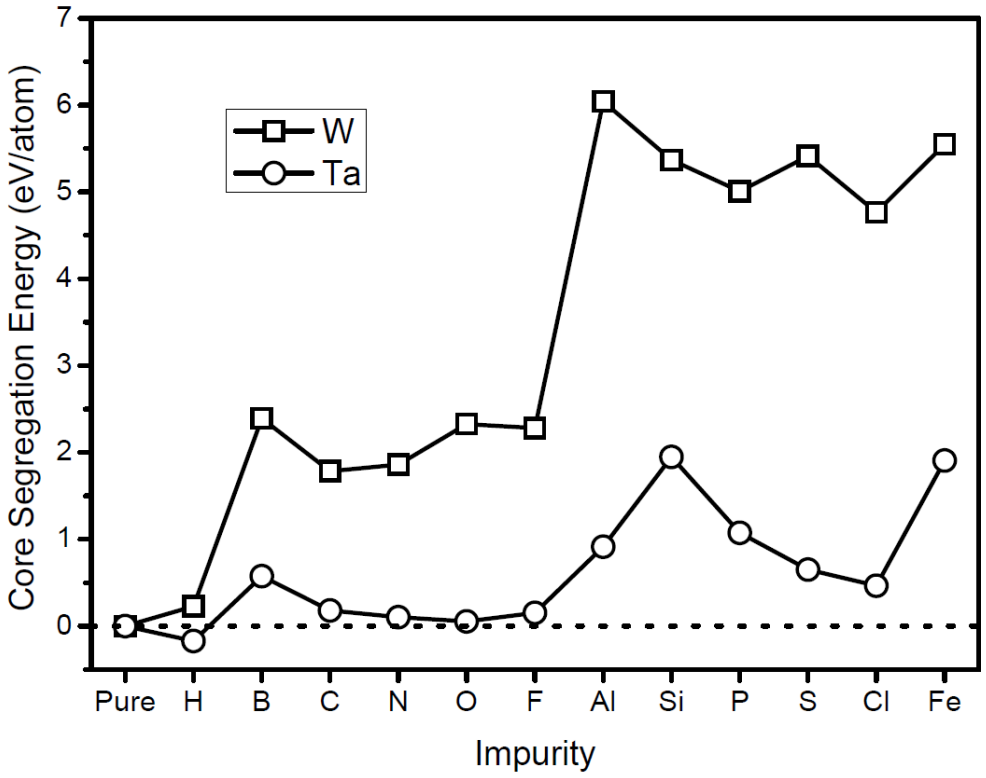

Figure 4-11: Screw dislocation core segregation energy for various impurities in tantalum and tungsten based on DFT calculations. The dotted horizontal line marks the position of zero segregation energy.

For the light impurity atoms such as from hydrogen to fluorine, the core segregation energy is close to zero in tantalum, but has appreciable values in tungsten, suggesting that impurities in tungsten are more likely to be segregated into the vicinity of the dislocation core. As a consequence, they should show relatively strong potential to influence the

dislocation properties. When compared with Figure 3-14, it is found that the core segregation energy of most of the impurities is slightly lower than their GB segregation energy in each individual metal.

4.3.4 The Peierls energy for screw dislocations in tantalum and tungsten

Figure 4-12 displays the Peierls energy of a screw dislocation in tantalum. The addition of all the investigated impurities increases the Peierls energy associated with the motion of a screw dislocation in tantalum, but with different extent depending on the specific impurity. The effect of oxygen and carbon seems to be the strongest, whereas the effect of boron and sulfur is moderate. At the beginning of the dislocation movement, the Peierls energy of pure tantalum and that with an oxygen impurity first decreases slightly, and it then increases with increasing displacement due to an unknown reason that calls for further investigation.

The Peierls energy associated with the motion of a screw dislocation in tungsten is shown in Figure 4-13. We can find that the results of tungsten are different from those of tantalum. All the investigated impurities first decrease the Peierls energy at the early stage of dislocation movement, and they then increase the energy significantly afterwards. Contrary to what is observed in Figure 4-12, sulfur first has the strongest softening effect but is then followed by the strongest obstructive effect to the screw dislocation movement in tungsten. The Peierls energies of the screw dislocation contaminated by carbon, oxygen, and boron first increase monotonically with increasing displacement; they then exhibit an abrupt drop at a displacement of around b/3. From Figures 4-12 and 4-13 we can see that the Peierls energy barrier of pure tungsten is higher than that of tantalum. However, the Peierls energy barrier of the contaminated dislocation core of tungsten is not always higher

than that of tantalum. For example, within the range of the investigated displacement, for the dislocation core contaminated by boron and sulfur, the Peierls energy of tungsten is ultimately higher than that of tantalum when the displacement is large enough, despite the fact that the former is sometimes lower than the latter at some moderate displacement. However, for the dislocation core contaminated by carbon and oxygen , the Peierls energy of tungsten is lower than that of tantalum for almost the entire investigated displacement range. This means that for tantalum and tungsten, the effect of impurities on their dislocation properties is not as distinct as that on their GB properties as one attempts to make a direct comparison between the two metals.

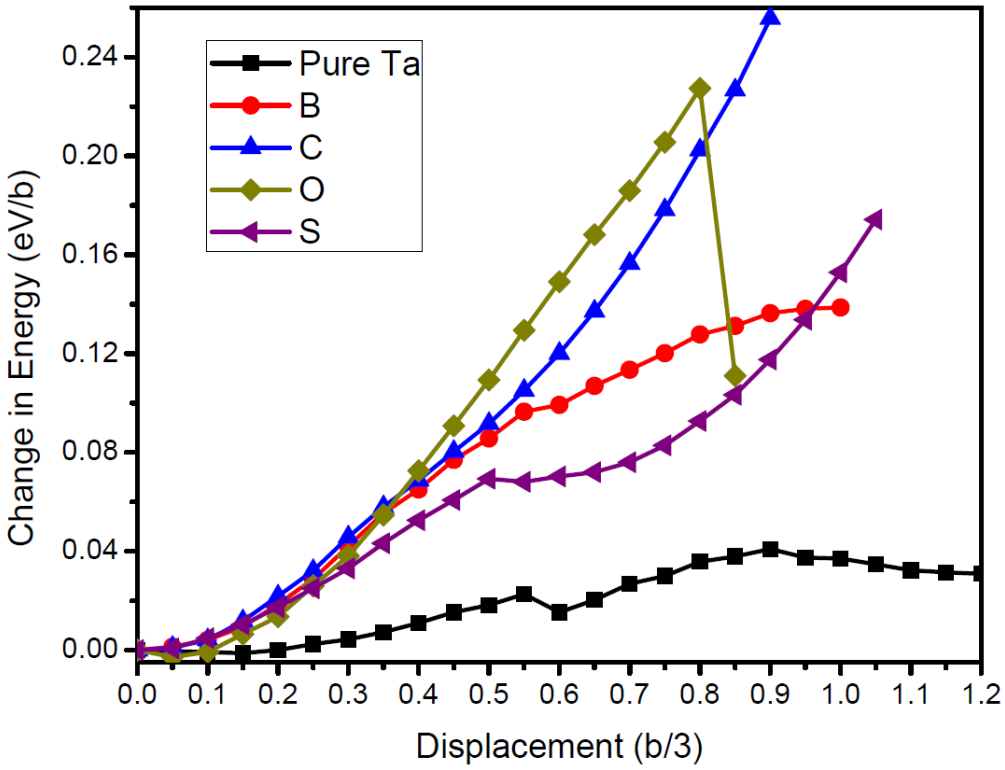

Figure 4-12: Peierls energy associated with the motion of a straight screw dislocation in tantalum with and without impurities in the vicinity of dislocation core.

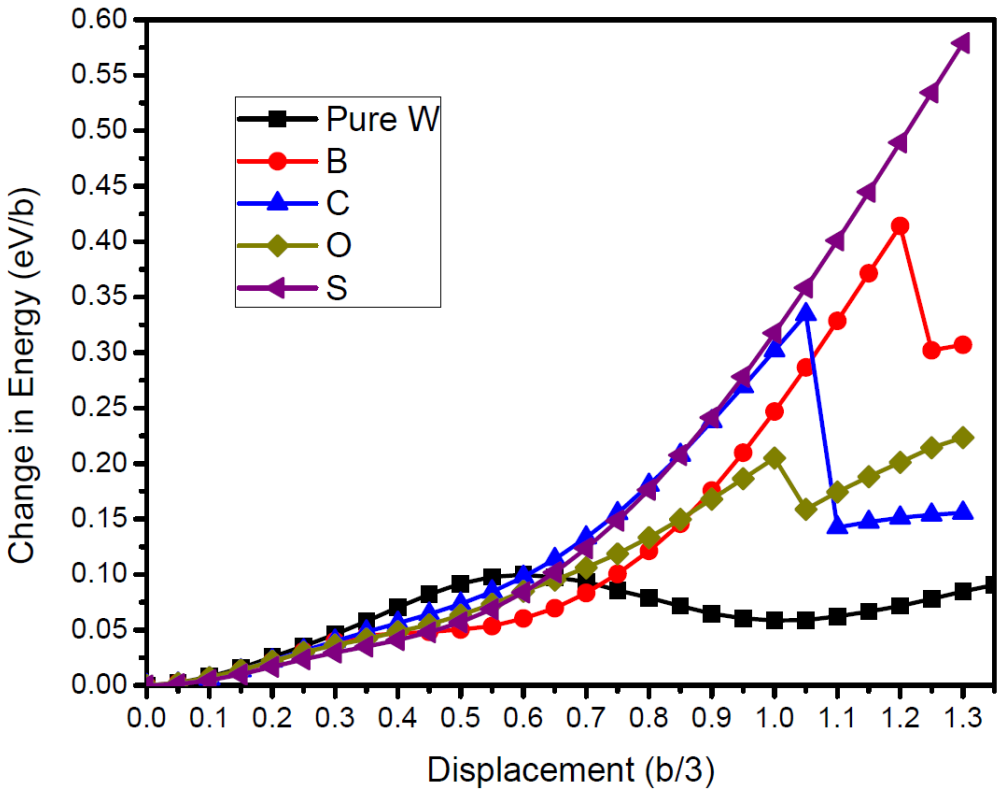

Figure 4-13: Peierls energy associated with the motion of a straight screw dislocation in tungsten with and without impurities in the vicinity of the dislocation core.

4.4 Discussion

4.4.1 Why and how impurities influence the mobility of dislocations

From the results we have shown, we can observe that the dislocation core segregation energy of various impurities resembles the GB segregation energy in both tantalum and tungsten. This observation suggests that the local atomic environment of core site of a screw dislocation is similar to that of a GB interstitial site. Naturally, then, similar factors such as volume mismatch and ability to form spatial networking bonding between the impurity and the surrounding host atoms, should be responsible for this observed behavior. As such, when considering the GB and the core segregation energies, we need to

calculate the binding energy of the impurities with the host atoms in the GB, near the dislocation core, and in the bulk, respectively. Since all these three types of interstitial sites are surrounded by the host atoms and are able to form spatial networking bonds with the impurities, probably the effect of volume mismatch between the host and the impurity atoms are more important in determining the difference in the binding energy between the various sites. From the results that the dislocation core segregation energy is a little bit lower than the GB segregation energy for a specific impurity, it is reasonable to hypothesize that the volume of the screw dislocation core interstitial site is a little bit smaller than that of a GB interstitial site. However, both should be larger than the volume bulk interstitial site. Since the lattice constant of tungsten is smaller than that of tantalum, the volume of the dislocation core interstitial site of tungsten should also be smaller than that of tantalum. Consequently, it should be reasonable to attribute the high dislocation core segregation energy of tungsten partly to its relatively small lattice constant or its relatively small interstitial site.

We can also try to understand why impurities influence the Peierls energy of screw dislocations in BCC structures in terms of the change in the local atomic environment caused by the movement of screw dislocations. When a dislocation moves away from its equilibrium position, both the host atom distribution and the volume of the interstitial site should also change accordingly, which eventually changes the binding energy between the impurity atom and the host atom. This will in turn lead to the change in the Peierls energy. Impurities that are more sensitive to the local atomic environment will introduce more increase in the Peierls energy. However, it still remains elusive as to whether impurities always have a hardening effect on the dislocation mobility, although the experimental

results in the literature appear to affirm this. The fundamental mechanism underlying this is still waiting to be revealed yet.

4.4.2 Impurity sensitivity of the mobility of screw dislocations

To influence the ductility of the matrix material by influencing the dislocation movement, the impurity must first have a chance to segregate into the vicinity of the core of the dislocation. This is determined by its dislocation core segregation energy. It is worth to recall that the segregation energy of an impurity atom associated with a certain site such as the GB, the dislocation core, etc., of a crystal is defined as the difference in the binding energies between that site vis a vis the perfect bulk site. This translates to the following: the higher the segregation energy of an impurity atom associated with a specific site, the greater the tendency that the impurity atom will settle at that site. The fact that the dislocation core segregation energy of most impurities in tungsten is much higher than that in tantalum implies that in tungsten the impurities are more likely to be segregated into the vicinity of the dislocation, and thus they tend to block the dislocation movement and decrease the mobility of dislocations in tungsten. We believe this is partly responsible for the brittleness of commercial purity tungsten. Furthermore, it is consistent with the fact that commercial purity polycrystalline tungsten is more sensitive to (interstitial) impurities. Whereas for tantalum, due to their lower segregation energy, the impurities have higher possibility to stay inside the bulk site and thus have less chance to block the motion of dislocation directly.

When sitting in an interstitial site near a dislocation core, whether or not the impurity reduces the ductility of the matrix metal is determined by its effect on the plastic deformation mode. In the calculations of the GSF energy, the results show that almost all

the investigated impurities reduce the energy barrier of both {110}/<111> and {211}/<111> ideal shear deformation in tantalum and tungsten. Exception include sulfur that increases the energy barrier of the {211}/<111> shear in tantalum, and oxygen and sulfur that increase the energy barrier of the {110}/<111> ideal shear in tungsten. From these results it seems that almost all the impurities under interrogation in this work have the potential to increase the ductility of tantalum and tungsten, since they make the plastic deformation much easier. However, the results from the calculations of the Peierls energy show that all the investigated impurities increase the Peierls energy of both metals and thus will impede the movement of dislocations and reduce the ductility of matrix metals. This finding is clearly inconsistent with that from GSF energy calculations, but it is indeed consistent with experimental results. It should be noted that even if the impurity stays inside the bulk site and is not segregated into the dislocation core, it can still have a chance to affect the dislocation movement by for example introducing lattice distortion and changing the stress filed around the dislocations, although such effect is of near-field nature. Unfortunately, based on these results, it is not yet quite adequate to address the issue as to which metal is more sensitive to the impurities. We will show that this is mostly due to the reason discussed in the next section.

4.4.3 Influence of prescribed reaction path

As we have mentioned earlier, among the many different possible ways, materials always choose the easiest way to deform. The practical way of deformation is determined by their intrinsic and extrinsic properties and the loading conditions. For plastic deformation, the possible way of deformation, or in other words, the possible reaction path can be the ideal shear along a certain atomic plane, the motion of straight dislocations,

dislocation nucleation, double kink mechanism, etc.. Among these possible reaction paths, for BCC metals a relatively low homologous temperatures ($T/T_m < \sim 0.25$) motion of screw dislocations through the double kink mechanism usually is the energetically most favorable reaction path. This is because it has been concluded that the mobility of edge dislocations in BCC metals is about 100 times greater than that of screw dislocations, and thus the edges are exhausted quickly as the plastic deformation begins, which renders edge dislocation to be an unsustainable mechanism in BCC metals [210]. When dealing with pure metals or alloys and investigating their plastic deformation related properties using atomistic or first-principles calculations, due to the limited number of atoms that can be handled in the computational model, people usually choose the ideal shear or straight dislocation movement as the reaction paths based on the assumption that the performance of the investigated reaction paths should be consistent with that of the practical reaction paths. For example, in our work, the energy barrier of ideal shear in pure tantalum is lower than that in pure tungsten; the Peierls energy barrier of pure tantalum is also lower than that of tungsten. Although the practical reaction path in the two metals at relatively low homologous temperature is usually the double kink mechanism and which has not been investigated here, we still feel confident to assume that the Peierls energy barrier of tantalum is lower than that tungsten if the reaction path is the double-kink mechanism. As a consequence, tantalum should be more ductile than tungsten.

However, this practice becomes problematic when dealing with commercial purity metals the effect of impurities become significant and cannot be ruled out. First of all, the effect of impurities on the matrix metals depends on the choice of the reaction path. As shown in Figures 4-6 to 4-9, almost all the impurities decrease the GSF energies of both

tantalum and tungsten, and thus should seemingly have a softening effect on these two metal, viz. they should increase their ductility; however, for the deformation mode of straight dislocation movement, all the investigated impurities increase the Peierls energy of both metals. This indicates that we cannot use the effect of impurities on the GSF energy and the Peierls energy to speculate how the impurities affect the practical reaction paths such as double kink mechanism. Second, the addition of impurities might change the practical reaction paths that dominate the plastic deformation. This can happen in many cases. Suppose we have two possible reaction paths, I and II, where path I is easier to occur and is sustainable, and is thus the practical path. The addition of impurities will change the energy barrier of the two reaction paths but usually with different extent of influence. If the impurity atom softens path I and/or hardens path II, there will be no change of the practical reaction path and the material is softened or becomes more ductile; otherwise, if the impurity hardens path I and/or soften path II, or hardens/softens both paths but has stronger effect on path I/II, it is possible that path II may eventually become easier to occur than path I, leading to a switch of the practical reaction path. For example, if the dislocations inside a metal are all strongly pinned by the impurities or the impurity induced pinning centers, it is possible for dislocation nucleation or multiplication to occur. Third, the addition of impurities can change the number of favorable reaction paths. As we have discussed before, it is possible for materials to deform through several possible reaction paths and the ability to deform increases with the increasing number of reaction paths available. When the impurities change the energy barrier of various reaction paths to different extents, it is highly possible that some reaction paths are excluded from the favorable paths due to their increased energy barrier, and at the same time certain other

reaction paths are driven into operation as the favorable paths due to their decreased energy barrier.

In our calculations, we have only considered two possible reaction paths, i.e., the ideal shear and straight dislocation movement. However, apparently none of them is the practical reaction path in the plastic deformation processes of BCC metals at relatively low homologous temperatures. Therefore the results we have obtained are not as adequate to answer the question of which one between tantalum and tungsten is more sensitive to impurities in terms of their effect on the plastic deformation ability. Even if we choose the more practical path such as double kink mechanism, we have to assume that the kink formation process is the same as in a clean dislocation core and move the relevant atoms to create kinks in a way by which we create kinks from a clean dislocation. This reaction path in a clean dislocation still deviates from that in a contaminated dislocation. In addition, it is not practical to create double kinks in first-principles calculations, since we need more atoms to ensure a long enough separation distance between the two kinks than the first-principles calculations can handle at the present time. However, despite the difficulty in choosing the authentic reaction path, we have reason to believe that if a more practical reaction path in pure metals used to investigate the impurity effect, it should tend to produce results more consistent with those from experiments, but mostly still in a qualitative sense. For example, the ideal shear is the most impractical reaction path for the plastic deformation of metals, the failure of which to predict the strength of materials gave rise to the advent of dislocation concept; whereas straight dislocation motion is more authentic in pure metals. Therefore, the effect of impurities on the Peierls energy of straight dislocation motion is more consistent with experimental results that interstitial impurities

usually harden and embrittle ductile materials. The direction to obtaining the reaction path that is close to the practical one is to control the least possible degree of freedom (DOF) of the atoms. For example, in our calculations, we can just move one atom in the dislocation core upward, instead of marching the whole row of atoms, and let the system accommodate the rest of the atoms. Probably the best way is to completely let the material choose the reaction path on its own, and we only prescribe the boundary conditions. In this case, large samples should tend to give more consistent results catching the properties of real materials.

4.5 Conclusion

From the aforementioned argument and based on the role of dislocations in determining the ductility of metals, we can conclude that commercial purity tungsten is less ductile than tantalum partly because the dislocation core segregation energy of various impurities in tungsten is higher than that in tantalum. That is to say, impurities are more likely to be segregated into the vicinity of the dislocation core and have more chance to pin the dislocation and reduce the ability of plastic deformation. As such they tend to decrease the ductility more of tungsten than tantalum, if we assume the investigated impurities will always retard the dislocation movement. As to the effect of impurities on the plastic deformation related properties, the calculations of the GSF energy and that of the Peierls energy give conflicting results, which is due to the influence of prescribed reaction path.

4.6 Deficiency and open-ended questions

In the calculations of the GSF energy, we can see that some GSF energy curves go down a little bit at the beginning of shear displacement; this is probably because the sample is not fully relaxed or is related to the non-zero stress state before shearing. Most of the

contaminated GSF energy curves reach a non-zero value at the end of the ideal shear. This is because the matrix atoms in the supercell are only allowed to move in the z direction and thus are not fully relaxed. Another issue arises when we use a makeup strategy to correct our results of the {211} plane GSF energy is that other calculation errors might have been introduced into the final results.

When calculating the dislocation core structure, it is reasonable to apply periodic boundary conditions in the <111> directions in order to model an infinitely long dislocation. However we have also applied periodic boundary conditions in the other two directions for some practical purpose, such as to reduce the super cell size to save computational time. It is appropriate to do this for a dislocation dipole or quadruple structure, but not so for a single dislocation. This is because a single screw dislocation is not periodic in the directions perpendicular to its line. The atoms inside the supercell will move to accommodate this imposed periodic boundary condition according to the minimum potential energy principle, leading to a deviation from the authentic screw dislocation structure. Although we fix the boundary atoms to preclude this process from happening, the interaction of the inner atoms between the super cell and its periodic image will more or less influence the final core configuration and the Peierls energy calculations. For example, the results that the Peierls energy of pure Ta and that with an oxygen impurity atom go down slightly at the beginning of displacement might have come from this interaction. Another issue is that the supercell is not in a stress-free state, although we assume it is.

When we use Equation 4.1 to create a screw dislocation, we assume that the displacement field of the screw dislocation is only a function of angle θ. In fact, it is also a

function of the distance from the dislocation core and becomes weaker and weaker until it vanishes when the distance goes to a value not so far away from the core in practice. Although we have run MD simulations to create a more authentic boundary for first principles calculations, the boundary for the MD simulations satisfies exactly Equation 4.1. This will more or less introduce some error into the final results. Another source of error might have resided in the EAM potential used in the MD simulations. Many MD simulations on BCC metals have produced asymmetric core structure, which is inconsistent with the results from more accurate first-principles calculations. Since we used the output of MD simulations as the boundary conditions of the DFT calculations, it is possible for the error from the MD simulations to be carried over into the DFT results.

In the Peierls energy calculations of tantalum, all the impurities increase the Peierls energy significantly and keep this trend to the end of the displacement. In tungsten, all the impurities first decrease the Peierls energy marginally and then they increase the Peierls energy significantly. Sulfur still keeps a strong tendency of increasing the Peierls energy till the end of the displacement. This indicates that it is impossible to evaluate how much the impurity will change the Peierls energy of pure metals since the total displacement is only about b/3 and thus is not sufficient to move the dislocation core from one stable site to another.

Impurities usually pin the dislocations and make plastic deformation more difficult to take place. However, in the calculation of the Peierls energy in tungsten, all the impurities reduce the Peierls energy at the early stage of motion. According to the principle that materials always choose the easiest and most sustainable way to deform, the plastic deformation should start from the contaminated dislocations if the impurity atoms have

softened them, and from the clean dislocations if impurity atoms have hardened them to such an extent that their mobility has been reduced to below that of clean dislocations. For impurities in tungsten as investigated in this work, it is possible that plastic deformation starts from contaminated dislocation but continues with clean dislocation. In other words, although the impurities eventually harden the dislocation, it is possible for the material to circumvent these harder reaction paths. In addition, we do have an example where rhenium can soften the dislocation of tungsten by increasing the number of slip planes, although in this case the impurity atoms sit at substitutional sites [102]. All the information available so far then converges to a question: is it possible for interstitial impurities to soften the material? If yes, then how? If no, then why?

In this work, we have only investigated the segregation energy of impurities sitting at the dislocation core and their effect on a single dislocation. We have not considered the segregation energy of impurities sitting in other possible interstitial sites and their effect on other dislocation related properties. For example, although the impurities are more likely to be segregated into the dislocation core due to their higher segregation energy over there, the distribution of impurities are also influenced by the number density of the available dislocation core interstitial sites. For single crystal samples with high density of dislocations, the number density of available core sites is also high, and impurities have more chance to segregate into the dislocation core. However, for samples with low density of dislocations, such as those after thermal annealing, the number density of core sites is low, and impurities have less chance to segregate into the core sites. In addition, according to the literature [211], the segregation energy of impurities can be a function of the distance away from the dislocation core, which also influences the distribution of the impurities.

Therefore, the possible site of impurities could be inside dislocation core, or away from, and their effect on dislocation properties should also vary with different interstitial sites. On the other hand, no matter where the impurity is, it will not only influence the energy barrier of moving dislocations, but will also influence other dislocation activities such as dislocation nucleation, interactions between dislocations, and dislocation velocity, etc. Following the practice in the literature, we can also investigate the impurity effect on dislocation velocity [212]. All these mechanisms may play an important role in determining the plastic deformation ability of the metal.

When using the Duesbery-Vitek criterion [105] to check the symmetry of the dislocation core, we found that $2\gamma(b/6)$ and $\gamma(b/3)$ are quite close for tantalum, but diverse for tungsten, although $2\gamma(b/6)$ is less than $\gamma(b/3)$ in both metals, favoring symmetric core. In Romaner's work [102], when the concentration level of rhenium is increased, the screw dislocation of tungsten transit from symmetric to asymmetric core and the GSF energy decreases, resulting in a decrease in the critical stress needed to start plastic deformation. It seems that low GSF energy, an asymmetric core structure, and the ductile behavior are correlated. Whether this is universally true for BCC metals is a question that is worth to explore and clarification of this question will definitely improves our understanding of ductility of the associated metal.

CHAPTER 5: DISCUSSION

In Chapter 3 and 4 we have provided some results based on first-principles calculations and molecular dynamics simulations concerning the ductility of tungsten and tantalum. We have especially evaluated the effects of interstitial impurities on the grain boundary and dislocation behavior of these two metals. Specifically we have interrogated the problems from the role of GBs and role of dislocations, respectively. We believe, based on our results, that none of these two approaches alone is sufficient to attain a complete understanding of the problem under investigation. In this chapter, we will attempt to combine the roles of the GBs and the dislocations, and we will try to give a more holistic understanding based on the notion that the ductility of a polycrystalline metal is determined by the competition between the processes of GB/crystal separation/cleavage and dislocation activities. If the former prevails, the metal will be brittle, while if the latter prevails, the metal will be ductile.

5.1 Ductility of pure tantalum and tungsten

Following the practice in the literature, we evaluate the ductility of pure tantalum and tungsten based on our own calculations. We use the ratio of the cleavage energy to the unstable stacking energy [154] to evaluate the ductility of single crystal metals. The cleavage energy is actually the clean FS energy. Likewise, we use the ratio of the GB separation energy to the unstable stacking energy to evaluate the ductility of polycrystalline metals. The GB separation energy is chosen to be γ_{sep} instead of $2\gamma_{sep}$ in

accordance with the cleavage energy. Since straight dislocation movement is the more realistic reaction path in plastic deformation than ideal shear, we also use the ratio of the cleavage energy to the unstable Peierls energy per unit area to evaluate the ductility of single crystal metals, and the ratio of the GB separation energy to the Peierls energy per unit area to evaluate the ductility of polycrystalline metals. Here the unstable Peierls energy per unit area is defined as the maximum Peierls energy increase when the dislocation sweeps a unit area. As shown in Figure 4-10, when the dislocation core moves from one position to another easy core position, the distance it moves is $\sqrt{6}a_0/3$, and the Burgers vector is $\sqrt{3}a_0/2$. Therefore, the area swept by the dislocation of length *b* is

$$A_{Peierls} = \frac{\sqrt{6}}{3}a_0 \times \frac{\sqrt{3}}{2}a_0 = \frac{\sqrt{2}}{2}a_0^2.$$

The unstable Peierls energy is

$$\gamma_{Peierls} = \frac{\Delta E_{Peierls}^{\max}}{A_{Peierls}} = \sqrt{2}a_0^2 \Delta E_{Peierls}^{\max},$$

where $\Delta E_{Peierls}^{\max}$ is the maximum value of change in energy shown in Figure 4-12 for tantalum and Figure 4-13 for tungsten.

Table 5-1: Parameters for tantalum and tungsten

	Tantalum	Tungsten
γ_s / γ_{us}	2.43	2.36
$\gamma_{sep} / \gamma_{us}$	1.73	1.45
$\gamma_s / \gamma_{Peierls}$	32.5	16.4
$\gamma_{sep} / \gamma_{Peierls}$	23.1	10.1

The results are shown in Table 5-1. From the data presented in Table 5-1, we can see that for the four ratios listed, the value of each ratio of tantalum is higher than that of

tungsten, indicating that in the cases of both single crystal and polycrystalline metals, the ductility of pure tantalum should be always higher than that of pure tungsten. This result is consistent with that shown in Table 1-4. It is worth to mention that the ratio of cleavage/GB separation energy to unstable stacking fault energy for tantalum is very close to that for tungsten. However, the ratio of cleavage/GB separation energy to the unstable Peierls energy of tantalum is more than two times that of tungsten, indicating that using a more realistic reaction path to make the comparison should provide more authentic and reliable results. This is in keeping with the well-documented notion that pure tantalum is much more ductile than pure tungsten, be it single crystal or polycrystalline. Nevertheless, the fundamental reason underlying this needs further investigation.

5.2 Ductility of commercial purity tantalum and tungsten

A quantitative estimation of the ductility of commercial purity tantalum and tungsten is beyond the scope of this thesis. It is also largely beyond the capability of the current status of materials science at the present time due to the great complexity of this problem. Therefore, in view of this, in this section, we will attempt to provide a more or less qualitative evaluation of the ductility of commercial purity tantalum and tungsten. Our discussion will be grounded on the observation that pure tantalum is more ductile than pure tungsten. The effect of impurities on the ductility of the matrix material is determined by its influence on the dislocation movement and the cleavage/GB separation energy. On the one hand, the ductility of the matrix material decreases if the impurity decreases the cleavage/GB separation energy and/or makes the dislocation mediated plastic deformation more difficult to occur. On the other hand, it increases if otherwise. For single crystal metals where GB is nonextant, the ductility is then determined by the competition between

crystal cleavage and dislocation activities. In our calculations, the energy needed for the cleavage of a unit area of a pure crystal along {111} plane is actually two times the clean FS energy provided in Figure 3-5. Note that we cannot use two times of the contaminated FS energy as the cleavage energy of a contaminated single crystal, because the FS energy is calculated using the pure crystal as the baseline configuration. The effect of impurities on the cleavage energy can be estimated from the FS segregation energy. Similar to the contaminated GB separation energy calculated by Equation 3.8, the contaminated single crystal cleavage energy is

$$2\gamma_{FS}^{I} = 2\gamma_{FS} - \frac{\Delta\mu_{FS}^{I}}{A}, \tag{5.1}$$

where $\Delta\mu_{FS}^{I}$ is the FS segregation energy of the impurity shown in Figure 3-15. From the results that the FS segregation energy of each investigated impurity in tantalum is higher than that in tungsten, we can infer that the effect of impurities on the cleavage energy, if deleterious, is more serious in tungsten than in tantalum. As a consequence, harmful interstitial impurities will produce more reduction in the ductility of tungsten than in tantalum. As we have discussed in Chapter 4, the difference of the effect of impurities on dislocation activities between tantalum and tungsten is not easy to see. However, it is clear that the dislocation core segregation energy of each investigated individual impurity is higher in tungsten than in tantalum, indicating that more impurities will be segregated into the vicinity of the dislocation core in tungsten than in tantalum. If we assume that impurities closer to the dislocation core have stronger pinning effect to dislocations, as revealed by the dynamic strain aging behavior of some materials [213, 214], and presumably more concentration level near the dislocation core will lead to a greater pinning effect, it is then reasonable to believe that impurities will have a stronger pinning

effect on the dislocation activities in tungsten than in tantalum. This will translate to greater reduction in the ductility of tungsten compared to tantalum. Naturally, the combined effects of impurities on the cleavage energy and dislocation activities should exacerbate the decreased ductility of single crystal tungsten versus tantalum.

For polycrystalline metals, the ductility is usually determined by the competition between the GB separation energy and the energy needed to drive dislocation activities. In Chapter 3, we have shown that all the investigated impurities have a higher GB segregation energy in tungsten than in tantalum. Their effect on GB separation energy, if detrimental, is stronger in tungsten than in tantalum. We have also shown that the GB separation energy of tungsten is more sensitive to the impurity concentration level than that of tantalum. All the these results appear to underscore the hypothesis that the malignant impurities lead to more reduction in the GB separation energy in tungsten. The effect of impurities on the dislocation activities in polycrystalline metals should be similar to that in single crystal metals, i.e. impurities have a stronger pinning effect on the dislocation movement in tungsten than in tantalum. Therefore, the combined effect of impurities on the GB separation energy and dislocation activities should further worsen the ductility of polycrystalline tungsten.

Although for both single crystal and polycrystalline cases, the deleterious impurities impart more adverse effect on the ductility of commercial purity tungsten than they do on commercial purity tantalum, the primary root cause that leads to the dichotomy between the two metals is different for single crystal and polycrystalline cases.

In addition to ductility, the effects of impurities on other mechanical properties such as yield strength and ultimate strength should also be different for the two cases. We

will discuss this problem based on the following four premises. First, the impurity effect, whether deleterious or beneficial, manifests itself when the impurity has a considerable concentration level at the concerned interstitial sites. The direct evidence supporting this notion comes from our calculation results presented in Figure 3-8 that suggests increasing the concentration level of sulfur significantly decreases the GB separation energy of both tantalum and tungsten. Indirect evidence for this comes from experimental results that show the increased ductility of grain-refined commercial purity tungsten through severe plastic deformation is partly attributed to the increased GB area that has diluted the impurity concentration level [215, 216]. Second, for brittle materials, the ultimate strength is determined by the cleavage/GB separation energy; whereas for ductile materials, the ultimate strength is determined by the interaction and competition between cleavage/GB separation processes and dislocation activities, as we have discussed in Chapter 1 of this thesis. Third, the yield strength of ductile materials is determined by dislocation activities. Last, there is an empirical but widely recognized relationship between the strength and ductility of the same material. Specifically speaking, for ductile materials, the ductility decreases with the increasing yield strength, while the ultimate strength usually increases with the amount of plastic deformation at fracture. For a single crystal matrix, the impurities may be distributed in the bulk interstitial sites, in the vicinity of dislocation core, and vacancies. It is usually believed that, the dislocation core and vacant interstitial lattice sites are the energetically more favorable interstitial sites. If the vacancies are randomly distributed inside the material, then the impurities that segregate into the vacancies will not be concentrated and the concentration of impurities only occurs in the vicinity of dislocation cores. Since the bulk interstitial sites are periodically distributed inside the

single crystal, the impurity distribution thereof should also be random. According to the aforementioned first premise, the impurities should have a stronger effect on the dislocation activities and thus the yield strength of single crystalline materials than they do on the cleavage energy. Since dislocation core segregation energy of any specific impurity in tungsten is higher than that in tantalum, the impurity concentration should be higher in tungsten and thus it should have a stronger effect on the yield strength and ductility of tungsten. For a polycrystalline matrix, both the dislocation core and GB regions have high segregation energy and are therefore potential sites for impurity segregation. In this work, we have only calculated the impurity effect on CSL GBs which are usually low energy GBs with relatively small interstitial sites. The relatively large sites exist in high energy random GB regions which thus have higher segregation energy and are more energetically favorable for impurity segregation than the CSL sites and dislocation core sites. This is especially true for tungsten which is more sensitive to impurities. Therefore, in a polycrystalline matrix, the GB segregation should have stronger propensity than dislocation core segregation, and as such the impurities should have a stronger effect on the GB separation energy than they have on the yield strength of the metal. Compared with tantalum, this effect should be more prominent in tungsten due to its higher GB segregation energy and stronger sensitivity to the concentration level of impurities.

5.3 The effect of impurities on DBTT

We have shown in Chapter 3 that the GB energy, FS energy, and GB separation energy are not strong functions of temperature. It is also known that dislocation activities are thermally activated processes [87-89] where the activation energy can be overcome by thermal energy and mechanical work from external loading. The thermal energy increases

with increasing temperature, thus the mechanical work needed to overcome the remaining activation energy barrier decreases with increasing temperature. If we use the ratio of cleavage/GB separation energy to activation energy of dislocation activities as an indicator for the ductility, then obviously, increasing the temperature will increases this ratio. As a result, the ductility will be enhanced as dislocation mediated plastic deformation becomes easier. On the other hand, when the impurities decrease the cleavage/GB separation energy and/or increase the activation energy for dislocation activities, the ductility of the metal will decrease until the material becomes completely brittle. However, increasing the temperature can make the material become ductile again. Though a rough and qualitative description, this is how the impurities change the ductile-to-brittle transition temperature (DBTT) of the matrix materials.

5.4 Universal understanding of strength, ductility, and toughness

The deformation processes of materials can be grouped into two categories: non-dissipative and dissipative processes. During the non-dissipative deformation such as linear elastic deformation, the external work done to the material is stored inside the material to increase the potential energy of the materials. This stored energy can be reciprocated back and the deformed atomic configuration can be recovered during the unloading process. Therefore, there is no entropy change during the deformation and the non-dissipative process is reversible. For the dissipative deformation such as plastic deformation of metals or alloys, the external work done to the material is converted to heat and eventually dissipated into the ambient environment. This work cannot be recovered during unloading; neither can the deformed atomic configuration be recovered after removing the external load. Therefore, there is entropy change during such dissipative

deformation processes and therefore they are irreversible. Generally speaking, the mechanical properties of materials such as the strength and ductility are determined by their ability to store external work inside and dissipate it into the ambient environment.

Strength is related to the non-dissipative deformation. As we have discussed before, according to the relationship between the unit of strength and energy, we can perceive strength as the maximum amount of energy per unit volume stored inside the deformed material; whereas the stress level can be considered as the current stored energy density inside the material. When the stress reaches the strength level of the material, the material cannot store any more energy and will fail through fracture. Based on this understanding, we can estimate whether a projectile can penetrate a target material by introducing a similar concept-kinetic energy density. If the kinetic energy per unit volume of the projectile is higher than the strength of the target material, it becomes possible for the penetration process to occur. Therefore, extending the concept of strength to volumetric energy density makes it easier to compare mechanical parameters from both quasi static and dynamic loading process.

Ductility of a material is the maximum dissipative deformation that the material can withstand before failure. Engineers care about the ductility of structural materials most probably because ductility is related to the fracture toughness of the material, which is more important for structural applications. Usually high ductility combined with reasonable strength points to high toughness, or high tolerance to damage be it pre-existing or service induced. That is the fundamental reason why we measure DBTT by examining the change in facture energy as a function of temperature. Although a combination of decent ductility and high strength usually ensures high toughness, they are not always

necessary for achieving high toughness. Toughness can be fundamentally perceived as the ability of the material to store and dissipate external work. The principle for the design and producing of tough materials should be to make sure that every individual building block of the material, whether at the macro-, meso-, micro, nano- or atomic scale, contributes to store and dissipate energy upon mechanical loading, and fails concurrently if it has to. This principle has been widely used in mechanical design where the most famous work might be the Deacon's wonderful carriage whose structural components failed concurrently on the same day [217]. For ductile materials, their high strain hardening rate and/or strain rate hardening helps to suppress plastic localization, which enables more portion of the deformed material undergo plastic deformation, and thus to convert more external work into heat and dissipate it into the ambient environment. Consequently, this leads to the increase in toughness.

For brittle materials, the toughness can be increased by introducing, for example, hierarchical structures [218-220] so that when one part of the material fails though fracture, other parts can take over the load bearing and withstand external loading until every part of the material fails. Different from ductile materials, brittle materials cannot dissipate much externally imposed mechanical energy into the environment. Instead, upon fracture, the stored mechanical energy is primarily converted into the surface energy of fragmented pieces. Thus the fracture process of a brittle material is a non-dissipative process. Based on this understanding we can see that high specific surface energy favors high toughness for brittle materials. The ideal case would be when the material finally fails by breaking all the atomic bonds that constitute the material.

CHAPTER 6: SUMMARY AND CONCLUSIONS

Based on atomistic and first-principles calculations, we have investigated the effect of various impurities (H, B, C, N, O, F, Al, Si, P, S, Cl, and Fe) on the ductility of tantalum and tungsten. We have examined the cases of both single crystal and polycrystalline metals, pure and contaminated by interstitial impurities. We have attempted to provide an at least qualitative understanding of why commercial purity tungsten is much less ductile than commercial purity tantalum. Based on the understanding that ductility is determined by the competition between cleavage/GB separation and dislocation activities, both the literature and our work have shown that pure tungsten is much less ductile than pure tantalum. We have taken this notion as the reference point and have calculated the effect of impurities on the cleavage/GB separation and dislocation activities. The results show that the impurity segregation energies associated with the GB, the FS, and the dislocation core in tungsten is higher than that in tantalum. This suggests that, impurities in tungsten are more likely to be segregated into the GB region and the vicinity of dislocations. As a result, these impurities have stronger tendency to impart influence on the properties of GBs and dislocations in tungsten.

The results of calculations of the impurity effect on the cleavage/GB separation energy show that boron, carbon, nitrogen, and iron increase the GB separation energy of tantalum. Carbon can also increase the single crystal cleavage energy of tantalum; whereas only boron and carbon can increase the GB separation energy of tungsten. The rest of the

investigated impurities have a stronger deleterious effect on the cleavage/GB separation energy of tungsten than they have on that of tantalum. All these results suggest that the ductility of tungsten suffers more from the deleterious impurities than the ductility of tantalum.

Our analyses also indicate that tungsten is more sensitive to impurities than tantalum because it has smaller lattice constant and thus smaller interstitial sites when compared to tantalum, leading to more volume mismatch with the impurity atoms. We have also calculated the effect of impurities on the generalized stacking fault energy (GSF) and the Peierils energy of tantalum and tungsten. However, the obtained results are not adequate for us to make a sensible comparison between tungsten and tantalum in terms of the impurity effect on their mechanical properties, primarily due to the inappropriately chosen reaction path.

CHAPTER 7: FUTURE WORK

7.1 Impurity sensitivity to local atomic environment

As we have pointed out in Chapter 3, we hypothesize that the maximum binding energy of various impurities with tantalum and tungsten is close or at least not far away when we try to figure out the fundamental reason that gives rise to the high impurity segregation energy in tungsten. We will prove this by systematically calculating the impurity sensitivity to local atomic environment including the distance between the impurity and host atoms and the angular distribution of host atoms and compare the results between tantalum and tungsten.

There is more practical significance to calculate the impurity sensitivity to local atomic environment. The GBs that can provide potential impurity segregation sites are diverse in nature. For example, they can be low energy CSL GBs, or high energy random GBs. GBs can be grouped into six different complexions according to their detailed microstructure [221]. In addition to the GB site and the vicinity of dislocation core, the impurities can also segregate into other possible sites such as vacancies, crack-tips, etc. All these possible impurity segregation sites have different local atomic environment and thus different influences on the impurity binding energy with the matrix. However, it is not realistic to calculate the binding energy of so many impurities sitting in myriads of segregation sites. Instead, we can group the possible segregation sites into several typical atomic environments and estimate the impurity effect from the impurity sensitivity to these

local atomic environments. Another thing is that we can construct interatomic potentials for atomistic simulations based on the impurity sensitivity to local atomic environment, just as Grujicic and co-workers used environment-sensitive embedding energies of impurities to modify the Finnis-Sinclair potential for tungsten [14].

7.2 Interactions between impurities

The mechanism by which impurities influence the materials properties changes with their concentration level. Take the impurity effect on GB properties as an example. For low impurity levels, the GB separation energy can be changed through the aforementioned chemical and mechanical effects of individual impurity atoms. When the impurity level is high enough, the interaction between impurity atoms will emerge and might become more important in changing the GB separation energy. In addition to the repulsive effect between sulfur atoms in nickel [37], tantalum, and tungsten, it has also been found that bismuth impurity can form a bilayer structure in the GB of nickel and the separation energy of this contaminated GB is actually determined by the weak bonding between the two layers of bismuth atoms that cover the two adjacent nickel grains [222]. Usually commercial purity materials contain more than one impurity species and the GB structure and separation energy should change with increasing number of impurity species due to the interactions between different impurity species. In order to estimate the optimum impurity concentration level and the combination of different impurity species when trying to use impurities to optimize the properties of materials (for example, using dopant to stabilize the high energy GB of nanocrystalline materials), we need to systematically calculate the interactions between the same as well as different impurity species.

The interactions between different impurity species can be competitive or cooperative. Such interactions can be either detrimental or beneficial to the matrix materials. The competitive or cooperative interactions between impurities can influence the impurity distributions inside the matrix materials and thus change their individual effect on the properties of the matrix. For example, different impurity species can interact in the GB region through the so-called site competition effect. The impurities with high binding energy with the matrix at the GB site push the impurities with low binding energy off the GB, which is beneficial to the ductility of the matrix material since the impurities with high binding energy usually increase the GB separation energy. However, it should be noted that even if some impurities are pushed off the GB region, it is highly possible for them to stay in the vicinity of GB, but not far away from it. In this case, they should still have more or less effect on the GB properties, which is worth further investigations.

Competitions not only exist between different impurity species, but they also exist between impurity atoms and host atoms. This can be used to determine whether the impurity is interstitial or substitutional. If the impurity binding energy with the matrix material at a specific substitutional site is larger than the energy needed to remove the host atom from this site, then the impurity atom prefers to stay in the substitutional site. Otherwise, the impurity atom stays in the interstitial site. We can use DFT calculations to verify this hypothesis.

When the concentration level is higher than the impurity solubility in the matrix material, some new phases may form in the GB region, which definitely will also influence the GB properties. The new phase can be the precipitates of one single impurity species; it can also be the compound formed between different impurity species and the host atoms.

Despite the rapidly growing complexity with increasing number of impurity species, how these new phase particles are formed and how they affect the properties of the matrix materials is another worthwhile topic.

7.3 Understand the impurity effect from electronic level

Although we have performed almost all the calculations based on first principles, we have not analyzed the impurity effect on the matrix material from the electronic level. The analysis at electronic level is crucial to the understanding of the problems and has been widely used in the literature. However, the conclusions drawn from the literature are sometimes not consistent and lead to contradicting understanding. For example, some authors deemed that GB can be strengthened by forming covalent-like bonds between the impurity atom and the neighboring host atoms [64]; however, some other authors attribute the embrittled GB to the localized covalent-like bonding and the reduced mobility of the electrons [71]. The conclusions cannot contradict with each other unless they are drawn based on the wrong calculation results. As part of our future work, we are going to calculate the sensitivity of impurity binding energy with the matrix material to the local atomic environment and analyze the results at electronic level by, for example, plotting the electron density map, calculating the electron density localization function and localized density of states. We believe these prospective efforts will help us dig deeper, gain more understanding to the issue and find a way to reconcile the contradictions.

7.4 Conflict between strength and ductility/toughness

In this work, we have concentrated on the impurity effect on the properties of both GBs and dislocations based on the fact that pure tantalum is more ductile than pure tungsten. We have also qualitatively estimated the ductility of pure tantalum and tungsten

based on our DFT calculations. However, we have not answered the question why pure tantalum is more ductile than pure tungsten, and at the same time it has much lower strength. Or more generally speaking, what is the fundamental principle giving rise to the conflict between strength and ductility of materials. This is a fundamental question worth further investigations. Based on our understanding, there seems to be some conserved function of multi-variables that link the strength and ductility, and the decline of one variable leads to the growth of the other.

The conjectured conserved function is probably related to the potential energy hyper-surface/landscape which can be perceived as a multidimensional function of the coordinates of all the atoms that constitute the material. The positions of all the atoms change during the deformation process. Then the potential energy of the whole system travels on the potential energy hyper-surface along a specific pathway. The mechanical behavior of the material is determined by the pathway which can be influenced by loading conditions. The failure of the material corresponds to the pathway along which the potential energy does not change anymore. For the same material, the initial atomic configuration or the microstructure determines the starting point on the potential energy hyper-surface and thus the pathway, leading to different mechanical behavior. The information about the strength and ductility of materials should be able to be retrieved from the pathways.

The potential energy hyper-surface has many valleys which correspond to various equilibrium states. Under external loading, the potential energy of the system can travel from one valley to another. The process from the valley to the transition point is uphill and non-dissipative. The process from the transition point to another valley is downhill and

dissipative. Based on the understanding that the strength of materials is related to the non-dissipative process and the ductility is related to the dissipative process, the information about the strength and ductility of materials are contained in the features of the hyper-surface, such as the slope of the pathway from the valley to the transition point and the number of valleys along the pathway. Ductile behavior should correspond to a large number of valleys.

At absolutely zero temperature, the potential energy of the system will stay in a specific valley. However, at a finite temperature, the system can actually travel between different states assisted with thermal activation. In this case, the macro mechanical properties of the material are determined by the statistical average of the attainable valleys. In this connection, we need to understand the temperature effect from the perspective of statistical mechanics and by means of phase space analysis that is widely used in statistical mechanics. The potential energy hyper-surface is not only a function of the atomic positions, but it also is a function of the number of atoms in the material. The material system with different geometry corresponds to different starting point on the hyper-surface. Therefore, in addition to the temperature effect on the ductility and strength, we can also use the potential energy hyper-surface to understand the size effect and the geometry effect on the mechanical properties of materials. Different materials have different potential energy hyper-surface, the feature or pattern of which renders the material to have different behavior. As such, when considering different materials, the conflict of strength and ductility can be understood by comparing the potential energy hyper-surface of these materials. Based on our understanding, the potential energy hyper-surface is the key to the general understanding of the mechanical behaviors of materials.

We can also try to understand the conflict of strength and ductility from electronic level. We have known that high cohesive energy and small lattice constant favor high strength. On one hand, covalent bonding or localized electron density between bonding atoms favor high cohesive energy and high strength; on the other hand, it decrease ductility due to the reduced mobility of bonding electrons. In contrast, metallic bonding or uniform electron density favor high ductility but low strength. The effect of lattice constant manifests itself by changing the average valence electron density. Given the same number of electrons, the material with large lattice constant has large space for distributing valence electrons, thus diluting the electron density and decreasing the strength. Large space probably will also increase the mobility of valence electrons and thus the ductility of materials. All these hypotheses are important to the understanding of the conflict of strength and ductility and therefore are worth further investigations.

REFERENCES

[1] R. Z. Valiev, I. V. Alexandrov, Y. T. Zhu and T. C. Lowe, "Paradox of strength and ductility in metals processed by severe plastic deformation," *Journal of Materials Research,* vol. 17, pp. 5-8, January 2002.

[2] R. Valiev, "Nanomaterial advantage," *Nature,* vol. 419, pp. 887-889 31 October 2002.

[3] R. O. Ritchie, "The conflicts between strength and toughness," *Nature Materials,* vol. 10, pp. 817-822, 2011.

[4] G. P. M. Leyson, W. A. Curtin, L. G. Hector, Jr and C. F. Woodward, "Quantitative prediction of solute strengthening in aluminum alloys," *Nature Materials,* vol. 9, pp. 750–755, September 2010.

[5] R. J. Amodeo and N. M. Ghoniem, "Dislocation dynamics. I. A proposed methodology for deformation micromechanics," *Physical Review B,* vol. 41, pp. 6958-6967, 1 April 1990.

[6] R. J. Amodeo and N. M. Ghoniem, "Dislocation dynamics. II. Applications to the formation of persistent slip bands, planar arrays, and dislocation cells," *Physical Review B,* vol. 41, pp. 6968-6976, 1 April 1990.

[7] W. D. Callister, Jr., *Materials Science and Engineering: An Intrduction*, 6 ed. New York: John Wiley & Sons, Inc., 2003.

[8] T. E. Tietz and J. W. Wilson, *Behavior and properties of refractory metals*. Stanford, Calif.: Stanford University Press, 1965.

[9] T. Ochs, O. Beck, E. C. and B. Meyer, "Symmetrical tilt grain boundaries in body-centred cubic transition metals: An ab initio local-density-functional study," *Philosophical Magazine A,* vol. 80, pp. 351-372, February 2000.

[10] E. Lassner and W.-D. Schubert, *Tungsten : properties, chemistry, technology of the element, alloys, and chemical compounds*. New York: Kluwer Academic/Plenum Publishers, 1999.

[11] J. A. Shields, S. H. Goods, R. Gibala and T. E. Mitchell, "Deformation of high purity tantalum single crystals at 4.2 K," *Materials Science and Engineering,* vol. 20, pp. 71-81, 1975.

[12] S. Takeuchi and K. Maeda, "Slip in high purity tantalum between 0.7 and 40 K," *Acta Metallurgica,* vol. 25, pp. 1485-1490, December 1977.

[13] J. R. Davis, "Tantalum and Tantalum Alloys," in *Corrosion of Weldments*, J. R. Davis, Ed., ed: ASM International, 2006, p. 164.

[14] M. Grujicic, H. Zhao and G. L. Krasko, "Atomistic simulation of $\Sigma 3$ (111) grain boundary fracture in tungsten containing various impurities " *International Journal of Refractory Metals and Hard Materials,* vol. 15, pp. 341-355 1997.

[15] B. C. Allen, D. J. Maykuth and R. I. Jaffee, "The Recrystallization and Ductile-Brittle Transition Behaviour of Tungsten-Effect of Impurities on Polycrystals Prepared from Single Crystals," *Journal of the Institute of Metals,* vol. 90, pp. 120-128, 1961.

[16] J. R. Davis, "Tantalum and Tantalum Alloys," in *Alloying: Understanding the Basics* J. R. Davis, Ed., ed: ASM International, 2001, p. 324.

[17] D. Hull, P. Beardmore and A. P. Valintine, "Crack Propagation in Single Crystals of Tungsten," *Philosophical Magazine,* vol. 12, pp. 1021-1041, 1965.

[18] A. P. Valintine and D. Hull, "Effect of temperature on the brittle fracture of polycrystalline tungsten," *Journal of the Less Common Metals,* vol. 17, pp. 353-361, 1969.

[19] A. Wronski and A. Fourdeux, "Slip-induced cleavage in polycrystalline tungsten," *Journal of the Less Common Metals,* vol. 6, pp. 413-429, 1964.

[20] A. S. Argon and S. R. Maloof, "Plastic Deformation of Tungsten Single Crystals at Low Temperatures," *Acta Metallurgica,* vol. 14, pp. 1449-1462, November 1966.

[21] A. S. Argon and S. R. Maloof, "Fracture of Tungsten Single Crystals at Low Temperatures," *Acta Metallurgica,* vol. 14, pp. 1463-1468, November 1966.

[22] K. Farrell, A. C. Schaffhauser and J. O. Stiegler, "Recrystallization, grain growth and the ductile-brittle transition in tungsten sheet," *Journal of the Less Common Metals,* vol. 13, pp. 141-155, August 1967.

[23] P. Gumbsch, "Brittle fracture and the brittle-to-ductile transition of tungsten " *Journal of Nuclear Materials,* vol. 323, pp. 304-312, 1 December 2003.

[24] P. Gumbsch, J. Riedle, A. Hartmaier and H. F. Fischmeister, "Controlling Factors for the Brittle-to-Ductile Transition in Tungsten Single Crystals," *Science,* vol. 282, pp. 1293-1295, 13 November 1998.

[25] Y. Zhang, A. V. Ganeev, J. T. Wang, J. Q. Liu and I. V. Alexandrov, "Observations on the ductile-to-brittle transition in ultrafine-grained tungsten of commercial purity," *Materials Science and Engineering A,* vol. 503, pp. 37-40, 15 March 2009.

[26] C. L. Younger and G. N. Wright, "Effect of Reactor Irradiation on Ductile-Brittle Transition and Stress-Strain Behavior of Tungsten," NASA, Cleveland TN D-5991, September 1970.

[27] M. Faleschini, H. Kreuzer, D. Kiener and R. Pippan, "Fracture toughness investigations of tungsten alloys and SPD tungsten alloys," *Journal of Nuclear Materials,* vol. 367-370, pp. 800-805, 1 August 2007.

[28] R. W. Buckman, Jr., "New applications for tantalum and tantalum alloys " *JOM,* vol. 52, pp. 40-41, March 2000.

[29] K. G. Hoge and A. K. Mukherjee, "The temperature and strain rate dependence of the flow stress of tantalum," *Journal of Materials Science,* vol. 12, pp. 1666-1672, 1977.

[30] A. H. Cottrell, Sir. , *Dislocations and Plastic Flow in Crystals*. Oxford: Clarendon Press, 1953.

[31] J. R. Rice and J.-S. Wang, "Embrittlement of interfaces by solute segregation," *Materials Science and Engineering: A,* vol. 107, pp. 23-40, January 1989.

[32] S. Dorfman, V. Liubich, D. Fuks and K. C. Mundim, "Simulations of decohesion and slip of the Σ3<111> grain boundary in tungsten with non-empirically derived interatomic potentials: the influence of boron interstitials," *Journal of Physics: Condensed Matter,* vol. 13, pp. 6719-6740 6 August 2001.

[33] J. R. Stephens, "Effects of Interstitial Impurities on the Low-Temperature Tensile Properties of Tungsten," NASA, Washington, Technical Notes NASA TN D-2287, June 1964.

[34] M. Aucouturier, "Grain Boundary Segregations and Hydrogen Embrittlement," *Journal de Physique,* vol. 43, pp. 175-186, December 1982.

[35] J. Kameda and C. McMahon, "Solute segregation and hydrogen-induced intergranular fracture in an alloy steel," *Metallurgical and Materials Transactions A,* vol. 14, pp. 903-911, 1983.

[36] Z. Zhang, Q. Lin and Z. Yu, "Grain boundary segregation in ultra-low carbon steel," *Materials Science and Engineering A,* vol. 291, pp. 22-26, 2000.

[37] M. Yamaguchi, M. Shiga and H. Kaburaki, "Grain Boundary Decohesion by Impurity Segregation in a Nickel-Sulfur System," *Science,* vol. 307, pp. 393-397, 21 January 2005.

[38] D. D. Mason, "Segregation-induced embrittlement of grain boundaries," *Philosophical Magazine A,* vol. 39, pp. 455-468, 1979.

[39] R. Schweinfest, A. T. Paxton and M. W. Finnis, "Bismuth embrittlement of copper is an atomic size effect," *Nature,* vol. 432, pp. 1008-1011, 23 December 2004.

[40] G. Duscher, M. F. Chisholm, U. Alber and M. Ruhle, "Bismuth-induced embrittlement of copper grain boundaries," *Nature Materials,* vol. 3, pp. 621-626, 2004.

[41] G. A. López, W. Gust and E. J. Mittemeijer, "Grain boundary and surface segregation in the Cu-Bi system," *Scripta Materialia,* vol. 49, pp. 747-753, 2003.

[42] P. Rez and J. R. Alvarez, "Calculation of cohesion and changes in electronic structure due to impurity segregation at boundaries in iron " *Acta Materialia,* vol. 47, pp. 4069-4075, November 1999.

[43] A. H. Cottrell, "Strengthening of Grain-Boundaries by Segregated Interstitials in Iron," *Materials Science and Technology,* vol. 6, pp. 121-123, Feb 1990.

[44] R. Kishore and A. Kumar, "Effect of carbon on the ductilisation of electron-beam welds in molybdenum," *Journal of Nuclear Materials,* vol. 101, pp. 16-27, 1981.

[45] M. K. Miller and A. J. Bryhan, "Effect of Zr, B and C additions on the ductility of molybdenum," *Materials Science and Engineering A,* vol. 327, pp. 80-83, 2002.

[46] S. Hofmann and H. Hofmann, "Influence of Grain Boundary Segregation on Mechanical Properties of Acativated Sintered Tungsten " *Journal de Physique* vol. 46, pp. 633-640, 1985.

[47] K. B. Povarova, A. S. Drachinskii, Y. O. Tolstobrov, A. V. Krainikov, V. N. Slyunyaev, V. A. Balashov, A. P. Popov and K. I. Konovalov, "Influence of Microalloying on the Cold-Brittleness Temperature of Tungsten," *Russian Metallurgy,* pp. 129-137, 1987.

[48] K. B. Povarova, Y. O. Tolstobrov, A. P. Popov and K. I. Konovalov, "Influence of Microalloying on The Low-temperature Plasticity and Technological Expediency of Vacuum-melted Tungsten of Technical Purity," *Russian Metallurgy,* pp. 74-79, 1990.

[49] R. F. Decker and J. W. Freeman, "The mechanism of beneficial effects of boron and zirconium on creep-rupture porperties of a complex heat-resistant alloy," *Transactions of the American Institute of Mining and Metallurgical Engineers,* vol. 218, pp. 277-285, 1960.

[50] J. Kameda and C. McMahon, "Solute segregation and brittle fracture in an alloy steel," *Metallurgical and Materials Transactions A,* vol. 11, pp. 91-101, 1980.

[51] M. S. Daw and M. I. Baskes, "Semiempirical, Quantum Mechanical Calculation of Hydrogen Embrittlement in Metals," *Physical Review Letters,* vol. 50, pp. 1285-1288, 25 April 1983.

[52] D. Farkas, B. Hyde, R. Nogueira and M. Ruda, "Atomistic simulations of the effects of segregated elements on grain-boundary fracture in body-centered-cubic Fe," *Metallurgical and Materials Transactions A,* vol. 36, pp. 2067-2072, 2005.

[53] F. Ercolessi and J. B. Adams, "Interatomic Potentials from First-Principles Calculations: the Force-Matching Method," *Europhysics Letters,* vol. 26, pp. 583-588, 10 June 1994.

[54] R. P. Messmer and C. L. Briant, "The role of chemical bonding in grain boundary embrittlement," *Acta Metallurgica,* vol. 30, pp. 457-467, 1982.

[55] R. Wu, A. J. Freeman and G. B. Olson, "First Principles Determination of the Effects of Phosphorus and Boron on Iron Grain Boundary Cohesion " *Science,* vol. 265, pp. 376 - 380, 15 July 1994.

[56] G. L. Krasko and G. B. Olson, "Effect of boron, carbon, phosphorus and sulphur on intergranular cohesion in iron," *Solid State Communications,* vol. 76, pp. 247-251, 1990.

[57] G. L. Krasko and G. B. Olson, "Effect of hydrogen on the electronic structure of a grain boundary in iron," *Solid State Communications,* vol. 79, pp. 113-117, 1991.

[58] G. L. Krasko, "Effect of impurities on the electronic structure of grain boundaries and intergranular cohesion in iron and tungsten " *Materials Science and Engineering A,* vol. 234-236, pp. 1071-1074 30 August 1997.

[59] G. L. Krasko, "Effect of impurities on the electronic structure of grain boundaries and intergranular cohesion in tungsten," *International Journal of Refractory Metals and Hard Materials,* vol. 12, pp. 251-260, 1993.

[60] W. T. Geng, A. J. Freeman, R. Wu, C. B. Geller and J. E. Raynolds, "Embrittling and strengthening effects of hydrogen, boron, and phosphorus on a Sigma 5 nickel grain boundary," *Physical Review B,* vol. 60, pp. 7149–7155 1999.

[61] Y.-Q. Fen and C.-Y. Wang, "Electronic effects of nitrogen and phosphorus on iron grain boundary cohesion " *Computational Materials Science,* vol. 20, pp. 48-56, January 2001.

[62] W. T. Geng, A. J. Freeman and G. B. Olson, "Influence of alloying additions on grain boundary cohesion of transition metals: First-principles determination and its phenomenological extension," *Physical Review B,* vol. 63, p. 165415, 2001.

[63] J.-X. Shang and C.-Y. Wang, "Electronic effects of alloying elements Nb and V on body-centred-cubic Fe grain boundary cohesion," *Journal of Physics: Condensed Matter,* vol. 13, pp. 9635-9644, 2001.

[64] R. Janisch and C. Elsässer, "Segregated light elements at grain boundaries in niobium and molybdenum," *Physical Review B,* vol. 67, p. 224101, 5 June 2003.

[65] A. Y. Lozovoi, A. T. Paxton and M. W. Finnis, "Structural and chemical embrittlement of grain boundaries by impurities: A general theory and first-principles calculations for copper," *Physical Review B,* vol. 74, p. 155416, 2006.

[66] W. T. Geng, A. J. Freeman and G. B. Olson, "Atomic Size Effect in Impurity Induced Grain Boundary Embrittlement," *Materials Transactions,* vol. 47, pp. 2113-2114, August 15 2006.

[67] Y. H. Chew, C. C. Wong, Z. Bakar and J. Ling, "First-principles Simulation Study on the Effects of Dopants on the Cohesion of Gold Grain Boundary," presented at the IEEE Advanced Packaging Materials Symposium, San Jose/Silicon Valley, CA USA, 2007.

[68] J. S. Braithwaite and P. Rez, "Grain boundary impurities in iron " *Acta Materialia,* vol. 53, pp. 2715-2726 May 2005.

[69] A. Y. Lozovoi and A. T. Paxton, "Boron in copper: A perfect misfit in the bulk and cohesion enhancer at a grain boundary," *Physical Review B,* vol. 77, p. 165413, 2008.

[70] M. Yamaguchi, Y. Nishiyama and H. Kaburaki, "Decohesion of iron grain boundaries by sulfur or phosphorous segregation: First-principles calculations," *Physical Review B,* vol. 76, p. 035418, 2007.

[71] M. Yuasa and M. Mabuchi, "Bond mobility mechanism in grain boundary embrittlement: First-principles tensile tests of Fe with a P-segregated Σ3 grain boundary," *Physical Review B,* vol. 82, p. 094108, 1 September 2010.

[72] Z. X. Tian, J. X. Yan, W. Xiao and W. T. Geng, "Effect of Lateral Contraction and Magnetism on the Energy Release Upon Fracture in Metals: First-Principles Computational Tensile Tests.," *Physical Review B,* vol. 79, p. 144114, 1 April 2009.

[73] A. Giannattasio, Z. Yao, E. Tarleton and S. G. Roberts, "Brittle–ductile transitions in polycrystalline tungsten," *Philosophical Magazine,* vol. 90, pp. 3947-3959, 28 October 2010.

[74] G. I. Taylor, "The Mechanism of Plastic Deformation of Crystals. Part I. Theoretical," *Proceedings of the Royal Society of London. Series A,* vol. 145, pp. 362-387, July 2 1934.

[75] X. Z. Liao, Y. H. Zhao, Y. T. Zhu, R. Z. Valiev and D. V. Gunderov, "Grain-size effect on the deformation mechanisms of nanostructured copper processed by high-pressure torsion," *Journal of Applied Physics,* vol. 96, pp. 636-640, 1 July 2004.

[76] X. Z. Liao, Y. H. Zhao, S. G. Srinivasan, Y. T. Zhu, R. Z. Valiev and D. V. Gunderov, "Deformation twinning in nanocrystalline copper at room temperature and low strain rate," *Applied Physics Letters,* vol. 84, pp. 592-594, 26 January 2004.

[77] F. C. Frank and W. T. Read, "Multiplication Processes for Slow Moving Dislocations," *Physical Review,* vol. 79, pp. 722-723, August 1950.

[78] S. G. Roberts, P. B. Hirsch, A. S. Booth, M. Ellis and F. C. Serbena, "Dislocations, cracks and brittleness in single crystals," *Physica Scripta,* vol. 1993, p. 420, 1993.

[79] P. Gumbsch, "Modelling brittle and semi-brittle fracture processes," *Materials Science and Engineering A,* vol. 319-321, pp. 1-7, 2001.

[80] A. Hartmaier and P. Gumbsch, "Thermal activation of crack-tip plasticity: The brittle or ductile response of a stationary crack loaded to failure," *Physical Review B,* vol. 71, p. 024108, 2005.

[81] A. Kelly and N. H. Macmillan, *Strong solids*. Oxford: Clarendon Press, 1986.

[82] M. A. Meyers, S. Traiviratana, V. A. Lubarda, D. J. Benson and E. M. Bringa, "The role of dislocations in the Growth of Nanosized Voids in Ductile Failure of Metals," *JOM,* vol. 61, pp. 35-41, February 2009.

[83] P. Gumbsch, "Modeling Strain Hardening the Hard Way," *Science,* vol. 301, pp. 1857-1858, 26 September 2003.

[84] R. Madec, B. Devincre, L. Kubin, T. Hoc and D. Rodney, "The Role of Collinear Interaction in Dislocation-Induced Hardening," *Science,* vol. 301, pp. 1879-1882, September 26 2003.

[85] G. E. Dieter, "Instability in Tension," in *Mechanical Metallurgy,* 3 ed Boston: McGraw-Hill, 1986, pp. 289-291.

[86] E. W. Hart, "Theory of the tensile test," *Acta Metallurgica,* vol. 15, pp. 351-355, February 1967.

[87] B. de Meester, C. Yin, M. Doner and H. Conrad, "Thermally Activated Deformation of Crystalline Solids," in *Rate Processes in Plastic Deformation of Materials*, J. C. M. Li and A. K. Mukherjee, Eds., ed Cleveland (Ohio): ASM, 1975, pp. 175-226.

[88] J. E. Dorn and S. Rajnak, "Nucleation of Kink Pairs and the Peierls' Mechanism of Plastic Deformation," *Transactions of the Metallurgical Society of AIME,* vol. 230, pp. 1052-1064, August 1964.

[89] A. V. Granato, K. Lucke, J. Schlipf and L. J. Teutonico, "Entropy Factors for Thermally Activated Unpinning of Dislocations," *Journal of Applied Physics,* vol. 35, pp. 2732-2745, September 1964.

[90] J. Gilman, *Electronic Basis of the Strength of Materials*. Cambridge, UK; New York: Cambridge University Press, 2003.

[91] H. Conrad, "The cryogenic properties of metals," in *High-Strength Materials*, V. F. Zackey, Ed., ed. New York: Wiley, 1965, p. 436.

[92] A. Giannattasio and S. G. Roberts, "Strain-rate dependence of the brittle-to-ductile transition temperature in tungsten," *Philosophical Magazine,* vol. 87, pp. 2589-2598, June 2007.

[93] J. H. Bechtold, "Strain rate effects in tungsten," *Transactions of the American Institute of Mining, Metallurgical and Petroleum Engineers,* vol. 206, pp. 142-146, February 1956.

[94] Q. Wei, "Strain rate effects in the ultrafine grain and nanocrystalline regimes—influence on some constitutive responses," *Journal of Materials Science,* vol. 42, pp. 1709-1727, 2007.

[95] M. Legros, G. Dehm, E. Arzt and T. J. Balk, "Observation of Giant Diffusivity Along Dislocation Cores," *Science,* vol. 319, pp. 1646 - 1649, 21 March 2008.

[96] A. H. Cottrell and B. A. Bilby, "Dislocation Theory of Yielding and Strain Ageing of Iron," *Proceedings of the Physical Society. Section A,* vol. 62, p. 49, 1949.

[97] R. H. Perkins, S. H. Cox, R. K. Waits and H. M. Busey, "Tantalum Annealing and Degassing and Hardness Effects of Dissolved Gases," Los Alamos Scientific Laboratory Rept. No. LA-2136, 15 May 1957.

[98] W. D. Klopp, F. R. Schwartzberg, F. C. Holden, C. T. Sims, H. R. Ogden and R. I. Jaffee, "Investigation of the Properties of Tantalum and its Alloys," Battelle Memorial Inst., Columbus, Ohio Rept. No. WADC-TR-58-525, July 1958.

[99] P. L. Raffo, "Yielding and fracture in tungsten and tungsten-rhenium alloys," *Journal of the Less Common Metals,* vol. 17, pp. 133-149, 1969.

[100] J. P. Hirth and J. Lothe, *Theory of dislocations*, 2 ed. New York: Wiley, 1982.

[101] J. Friedel, *Dislocations*. Oxford: Pergamon Press, 1967.

[102] L. Romaner, C. Ambrosch-Draxl and R. Pippan, "Effect of Rhenium on the Dislocation Core Structure in Tungsten," *Physical Review Letters,* vol. 104, p. 195503, 14 May 2010.

[103] M. W. Finnis and J. E. Sinclair, "A simple empirical *N*-body potential for transition metals," *Philosophical Magazine A,* vol. 50, pp. 45-55, 1984.

[104] V. Vitek, "Theory of the Core Structure of Dislocations in Body-Centered-Cubic Metals," *Crystal Lattice Defects,* vol. 5, pp. 1-34, 1974.

[105] M. S. Duesbery and V. Vitek, "Plastic Anisotropy in BCC Transition Metals," *Acta Materialia,* vol. 46, pp. 1481-1492, 2 March 1998.

[106] R. Peierls, "The size of a dislocation," *Proceedings of the Physical Society,* vol. 52, pp. 34-37, 1940.

[107] F. R. N. Nabarro, "Dislocations in a simple cubic lattice," *Proceedings of the Physical Society,* vol. 59, p. 256, 1947.

[108] W. Cai, V. V. Bulatov, J. P. Chang, J. Li and S. Yip, "Anisotropic elastic interactions of a periodic dislocation array," *Physical Review Letters,* vol. 86, pp. 5727-5730, Jun 2001.

[109] R. Gröger, A. G. Bailey and V. Vitek, "Multiscale modeling of plastic deformation of molybdenum and tungsten: I. Atomistic studies of the core structure and glide of 1/2<111> screw dislocations at 0K," *Acta Materialia,* vol. 56, pp. 5401-5411, November 2008.

[110] J. Li, C. Z. Wang, J. P. Chang, W. Cai, V. V. Bulatov, K. M. Ho and S. Yip, "Core energy and Peierls stress of a screw dislocation in bcc molybdenum: A periodic-cell tight-binding study," *Physical Review B,* vol. 70, p. 104113, Sep 2004.

[111] D. E. Segall, A. Strachan, W. A. Goddard, S. Ismail-Beigi and T. A. Arias, "Ab initio and finite-temperature molecular dynamics studies of lattice resistance in tantalum," *Physical Review B,* vol. 68, p. 014104, 2003.

[112] D. R. Trinkle and C. Woodward, "The Chemistry of Deformation: How Solutes Soften Pure Metals," *Science,* vol. 310, pp. 1665-1667, 9 December 2005.

[113] L. Ventelon and F. Willaime, "Core structure and Peierls potential of screw dislocations in alpha-Fe from first principles: cluster versus dipole approaches," *Journal of Computer-Aided Materials Design,* vol. 14, pp. 85-94, 2007.

[114] W. Xu and J. A. Moriarty, "Atomistic simulation of ideal shear strength, point defects, and screw dislocations in bcc transition metals: Mo as a prototype," *Physical Review B,* vol. 54, pp. 6941–6951, 1996.

[115] W. Xu and J. A. Moriarty, "Accurate atomistic simulations of the Peierls barrier and kink-pair formation energy for <111> screw dislocations in bcc Mo," *Computational Materials Science,* vol. 9, pp. 348-356, January 1998.

[116] V. Vítek, "Intrinsic stacking faults in body-centred cubic crystals," *Philosophical Magazine,* vol. 18, pp. 773-786, 01 October 1968.

[117] V. Vítek and F. Kroupa, "Generalized splitting of dislocations," *Philosophical Magazine,* vol. 19, pp. 265-284, 01 February 1969.

[118] E. O. Hall, "The Deformation and Ageing of Mild Steel: III Discussion of Results," *Proceedings of the Physical Society B,* vol. 64, pp. 747-753, 1 September 1951.

[119] N. J. Petch, "The cleavage strength of polycrystals," *Journal of the Iron and Steel Institute,* vol. 174, pp. 25-28, 1953.

[120] M. D. Uchic, D. M. Dimiduk, J. N. Florando and W. D. Nix, "Sample Dimensions Influence Strength and Crystal Plasticity " *Science,* vol. 305, pp. 986-989, 13 August 2004.

[121] D. Jang and J. R. Greer, "Transition from a strong-yet-brittle to a stronger-and-ductile state by size reduction of metallic glasses," *Nature Materials,* vol. 9, pp. 215-219, March 2010.

[122] Q. Yu, Z.-W. Shan, J. Li, X. Huang, L. Xiao, J. Sun and E. Ma, "Strong crystal size effect on deformation twinning," *Nature,* vol. 463, pp. 335-338, 21 January 2010.

[123] J. Schiotz, F. D. Di Tolla and K. W. Jacobsen, "Softening of nanocrystalline metals at very small grain sizes," *Nature,* vol. 391, pp. 561-563, 5 February 1998.

[124] J. Schiøtz and K. W. Jacobsen, "A Maximum in the Strength of Nanocrystalline Copper," *Science,* vol. 301, pp. 1357 - 1359, 5 September 2003.

[125] Z. Pan, Y. Li and Q. Wei, "Tensile properties of nanocrystalline tantalum from molecular dynamics simulations " *Acta Materialia,* vol. 56, pp. 3470-3480 August 2008.

[126] G. P. Zheng, Y. M. Wang and M. Li, "Atomistic simulation studies on deformation mechanism of nanocrystalline cobalt " *Acta Materialia,* vol. 53, pp. 3893-3901, August 2005.

[127] N. Nagasako, M. Jahnátek, R. Asahi and J. Hafner, "Anomalies in the response of V, Nb, and Ta to tensile and shear loading: Ab initio density functional theory calculations," *Physical Review B,* vol. 81, p. 094108, 17 March 2010.

[128] L. Koči, Y. Ma, A. R. Oganov, P. Souvatzis and R. Ahuja, "Elasticity of the superconducting metals V, Nb, Ta, Mo, and W at high pressure," *Physical Review B,* vol. 77, p. 214101, 2008.

[129] P. Söderlind, O. Eriksson, J. M. Wills and A. M. Boring, "Theory of elastic constants of cubic transition metals and alloys," *Physical Review B,* vol. 48, p. 5844, 1993.

[130] K. W. Katahara, M. H. Manghnan and E. S. Fisher, "Pressure derivatives of the elastic moduli of BCC Ti-V-Cr, Nb-Mo and Ta-W alloys," *Journal of Physics F: Metal Physics,* vol. 9, pp. 773-790, 1979.

[131] F. H. Featherston and J. R. Neighbours, "Elastic Constants of Tantalum, Tungsten, and Molybdenum," *Physical Review,* vol. 130, pp. 1324-1333, 1963.

[132] R. Ayres, "Elastic constants of tungsten-rhenium alloys from 77 to 298 °K," *Journal of Applied Physics,* vol. 46, p. 1526, 1975.

[133] Y. Mishin and A. Y. Lozovoi, "Angular-dependent interactomic potential for tantalum," *Acta Materialia,* vol. 54, pp. 5013-5026, 2006.

[134] S. L. Frederiksen and K. W. Jacobsen, "Density functional theory studies of screw dislocation core structures in bcc metals," *Philosophical Magazine,* vol. 83, pp. 365-375, Jan 2003.

[135] G. Wang, A. Strachan, T. Cagin and W. A. Goddard, "Molecular dynamics simulations of 1/2 a<1 1 1> screw dislocation in Ta," *Materials Science and Engineering A,* vol. 309-310, pp. 133-137, 2001.

[136] P. A. Gordon, T. Neeraj, Y. Li and J. Li, "Screw dislocation mobility in BCC metals: the role of the compact core on double-kink nucleation," *Modelling and Simulation in Materials Science and Engineering,* vol. 18, Dec 2010.

[137] M. Mrovec, R. Gröger, A. G. Bailey, D. Nguyen-Manh, C. Elsässer and V. Vitek, "Bond-order potential for simulations of extended defects in tungsten," *Physical Review B,* vol. 75, p. 104119, 1 March 2007.

[138] L. H. Yang and J. A. Moriarty, "Kink-pair mechanisms for a/2 <111> screw dislocation motion in bcc tantalum," *Materials Science and Engineering A,* vol. 319-321, pp. 124-129, 2001.

[139] S. Ogata, J. Li and S. Yip, "Ideal Pure Shear Strength of Aluminum and Copper," *Science,* vol. 298, pp. 807-811, October 25, 2002 2002.

[140] V. V. Bulatov, L. L. Hsiung, M. Tang, A. Aresenlis, M. C. Bartelt, W. Cai, J. N. Florando, M. Hiratani, M. Rhee, G. Hommes, T. G. Pierce and T. D. d. l. Rubia, "Dislocation multi-junctions and strain hardening," *Nature,* vol. 440, pp. 1174-1178, 27 April 2006.

[141] B. Devincre, T. Hoc and L. Kubin, "Dislocation Mean Free Paths and Strain Hardening of Crystals," *Science,* vol. 320, pp. 1745-1748, 27 June 2008.

[142] B. Devincre and L. P. Kubin, "Simulations of forest interactions and strain hardening in FCC crystals," *Modelling and Simulation in Materials Science and Engineering,* vol. 2, p. 559, 1994.

[143] V. Vitek, "Core structure of screw dislocations in body-centred cubic metals: relation to symmetry and interatomic bonding," *Philosophical Magazine,* vol. 84, pp. 415-428, Jan-Feb 2004.

[144] K. Ito and V. Vitek, "Atomistic study of non-Schmid effects in the plastic yielding of bcc metals," *Philosophical Magazine A,* vol. 81, pp. 1387-1407, 01 May 2001.

[145] Y. Cheng, M. Mrovec and P. Gumbsch, "Atomistic simulations of interactions between the $1/2\langle 111\rangle$ edge dislocation and symmetric tilt grain boundaries in tungsten," *Philosophical Magazine,* vol. 88, pp. 547-560, 1 February 2008.

[146] P. M. Derlet, P. Gumbsch, R. Hoagland, J. Li, D. L. McDowell, H. Van Swygenhoven and J. Wang, "Atomistic Simulations of Dislocations in Confined Volumes," *MRS Bulletin,* vol. 34, pp. 184-189, March 2009.

[147] A. Cottrell, "The art of simplification in materials science," *MRS Bulletin,* vol. 22, pp. 15-19, May 1997.

[148] L. Vitos, P. A. Korzhavyi and B. Johansson, "Stainless steel optimization from quantum mechanical calculations," *Nature Materials,* vol. 2, pp. 25-28, January 2003.

[149] G. N. Greaves, A. L. Greer, R. S. Lakes and T. Rouxel, "Poisson's ratio and modern materials," *Nature Materials,* vol. 10, pp. 823-837, 2011.

[150] J. J. Lewandowski, W. H. Wang and A. L. Greer, "Intrinsic plasticity or brittleness of metallic glasses," *Philosophical Magazine Letters,* vol. 85, pp. 77-87, 2005/02/01 2005.

[151] S. F. Pugh, "Relations between the elastic moduli and the plastic properties of polycrystalline pure metals," *Philosophical Magazine,* vol. 45, pp. 823-843, 1954/08/01 1954.

[152] Z. A. D. Lethbridge, R. I. Walton, A. S. H. Marmier, C. W. Smith and K. E. Evans, "Elastic anisotropy and extreme Poisson’s ratios in single crystals," *Acta Materialia,* vol. 58, pp. 6444-6451, 2010.

[153] A. Kelly, W. R. Tyson and A. H. Cottrell, "Ductile and brittle crystals " *Philosophical Magazine,* vol. 15, pp. 567-586, March 1967.

[154] J. R. Rice, "Dislocation Nucleation From a Crack Tip: an Analysis Based on the Peierls Concept," *Journal of Mechanics and Physics of Solids,* vol. 40, pp. 239-271, 1992.

[155] J. R. Rice and R. Thomson, "Ductile versus brittle behaviour of crystals," *Philosophical Magazine,* vol. 29, pp. 73-96, 1974.

[156] J. R. Rice, "Hydrogen and Interfacial Cohesion," in *Effect of Hydrogen on Behavior of Materials*, A. W. Thompson and I. M. Berstein, Eds., ed New York: Metallurgical Society of AIME, 1976, pp. 455-466.

[157] P. M. Anderson and J. R. Rice, "Dislocation Emission from Cracks in Crystals or Along Crystal Interfaces," *Scripta Metallurgica,* vol. 20, pp. 1467-1472, 1986.

[158] A. J. Pons and A. Karma, "Helical crack-front instability in mixed-mode fracture," *Nature,* vol. 464, pp. 85-89, 4 March 2010.

[159] M. J. Buehler and H. Gao, "Dynamical fracture instabilities due to local hyperelasticity at crack tips," *Nature,* vol. 439, pp. 307-310, 2006.

[160] J. R. Kermode, T. Albaret, D. Sherman, N. Bernstein, P. Gumbsch, M. C. Payne, G. Csányi and A. De Vita, "Low-speed fracture instabilities in a brittle crystal," *Nature,* vol. 455, pp. 1224-1227 30 October 2008.

[161] X. H. Zeng and A. Hartmaier, "Modeling size effects on fracture toughness by dislocation dynamics," *Acta Materialia,* vol. 58, pp. 301-310, January 2009.

[162] D. Roundy, C. R. Krenn, M. L. Cohen and J. W. Morris, Jr., "The ideal strength of tungsten," *Philosophical Magazine A,* vol. 81, pp. 1725-1747, July 2001.

[163] E. B. Tadmor and S. Hai, "A Peierls criterion for the onset of deformation twinning at a crack tip," *Journal of the Mechanics and Physics of Solids,* vol. 51, pp. 765-793, 2003.

[164] A. Latapie and D. Farkas, "Molecular dynamics simulations of stress-induced phase transformations and grain nucleation at crack tips in Fe," *Modelling and Simulation in Materials Science and Engineering,* vol. 11, pp. 745-753, September 2003.

[165] E. A. Carter, "Challenges in Modeling Materials Properties Without Experimental Input," *Science,* vol. 321, pp. 800 - 803, 8 August 2008.

[166] A. J. Cohen, P. Mori-Sánchez and W. Yang, "Insights into Current Limitations of Density Functional Theory," *Science,* vol. 321, pp. 792-794, 8 August 2008.

[167] J. J. Kohanoff, *Electronic structure calculations for solids and molecules: theory and computational methods*. Cambridge, UK; New York: Cambridge University Press, 2006.

[168] R. M. Martin, *Electronic structure : basic theory and practical methods*. Cambridge, UK; New York: Cambridge University Press, 2004.

[169] S. R. Billeter, A. Curioni and W. Andreoni, "Efficient linear scaling geometry optimization and transition-state search for direct wavefunction optimization

schemes in density functional theory using a plane-wave basis," *Computational Materials Science,* vol. 27, pp. 437-445, June 2003.

[170] D. J. Chadi and M. L. Cohen, "Special Points in the Brillouin Zone," *Physical Review B,* vol. 8, pp. 5747-5753, 15 December 1973.

[171] L. Genovese, T. Deutsch and S. Goedecker, "Efficient and accurate three-dimensional Poisson solver for surface problems," *The Journal of Chemical Physics,* vol. 127, p. 054704, 7 August 2007.

[172] L. Genovese, T. Deutsch, A. Neelov, S. Goedecker and G. Beylkin, "Efficient solution of Poisson's equation with free boundary conditions," *Journal of Chemical Physics,* vol. 125, Aug 2006.

[173] T. P. Hamilton and P. Pulay, "Direct inversion in the iterative subspace (DIIS) optimization of open ‐ shell, excited ‐ state, and small multiconfiguration SCF wave functions " *Journal of Chemical Physics,* vol. 84, pp. 5728-5734, May 1986.

[174] G. Kresse, Furthm, uuml and J. ller, "Efficient iterative schemes for ab initio total-energy calculations using a plane-wave basis set," *Physical Review B,* vol. 54, pp. 11169–11186 15 October 1996.

[175] H. J. Monkhorst and J. D. Pack, "Special points for Brillouin-zone integrations," *Physical Review B,* vol. 13, pp. 5188–5192, 1976.

[176] J. Moreno and J. M. Soler, "Optimal meshes for integrals in real- and reciprocal-space unit cells," *Physical Review B,* vol. 45, pp. 13891–13898 15 June 1992.

[177] K. Capelle, "A Bird's-Eye View of Density-Functional Theory," *Brazilian Journal of Physics,* vol. 36, pp. 1318-1343, December 2006.

[178] P. Hohenberg and W. Kohn, "Inhomogeneous Electron Gas," *Physical Review,* vol. 136, pp. B864-B871, 9 November 1964.

[179] W. Kohn, "Nobel Lecture: Electronic structure of matter—wave functions and density functionals," *Reviews of Modern Physics,* vol. 71, pp. 1253-1266, 1999.

[180] W. Kohn and L. J. Sham, "Self-Consistent Equations Including Exchange and Correlation Effects," *Physical Review,* vol. 140, pp. A1133-1138, 15 November 1965.

[181] J. A. Pople, "Nobel Lecture: Quantum chemical models," *Reviews of Modern Physics,* vol. 71, pp. 1267-1274, 1999.

[182] J. P. Perdew, K. Burke and M. Ernzerhof, "Generalized Gradient Approximation Made Simple," *Physical Review Letters,* vol. 77, pp. 3865-3868, 1996.

[183] J. P. Perdew and Y. Wang, "Accurate and simple analytic representation of the electron-gas correlation energy," *Physical Review B,* vol. 45, pp. 13244-13249, 1992.

[184] S. Goedecker, M. Teter and J. Hutter, "Separable dual-space Gaussian pseudopotentials," *Physical Review B,* vol. 54, pp. 1703-1710, 15 July 1996.

[185] C. Hartwigsen, S. Goedecker and J. Hutter, "Relativistic separable dual-space Gaussian pseudopotentials from H to Rn," *Physical Review B,* vol. 58, pp. 3641-3662, 1998.

[186] H. Hellmann, "A New Approximation Method in the Problem of Many Electrons," *The Journal of Chemical Physics,* vol. 3, pp. 61-61, 1935.

[187] W. E. Pickett, "Pseudopotential methods in condensed matter applications," *Computer Physics reports,* vol. 9, pp. 115-197, 1989.

[188] D. Vanderbilt, "Soft self-consistent pseudopotentials in a generalized eigenvalue formalism," *Physical Review B,* vol. 41, pp. 7892-7895, 15 April 1990.

[189] D. S. Sholl and J. A. Steckel, "Nuts and Bolts of DFT Calculations," in *Density Functional Theory*, ed: John Wiley & Sons, Inc., 2009, pp. 49-81.

[190] H. Grimmer, W. Bollmann and D. H. Warrington, "Coincidence-Site Lattice and Complete Pattern-Shift Lattices in Cubic Crystals," *Acta Crystallographica Section A,* vol. 30, pp. 197-207, March 1974.

[191] "CPMD, http://www.cpmd.org/, Copyright IBM Corp 1990-2008, Copyright MPI für Festkörperforschung Stuttgart 1997-2001.," ed.

[192] R. Car and M. Parrinelo, "Unified Approach for Molecular Dynamics and Density-Functional Theory," *Physical Review Letters,* vol. 55, pp. 2471-2474, 25 November 1985.

[193] S. Plimpton, "Fast Parallel Algorithms for Short-Range Molecular Dynamics," *Journal of Computational Physics,* vol. 117, pp. 1-19, 1995.

[194] S. Plimpton, R. Pollock and M. Stevens, "Particle-Mesh Ewald and rRESPA for Parallel Molecular Dynamics Simulations " in *Proceedings of the Eighth SIAM Conference on Parallel Processing for Scientific Computing*, Minneapolis, MN, 1997.

[195] Y. Li, D. J. Siegel, J. B. Adams and X.-Y. Liu, "Embedded-atom-method tantalum potential developed by the force-matching method," *Physical Review B,* vol. 67, p. 125101, 4 March 2003.

[196] X. W. Zhou, H. N. G. Wadley, R. A. Johnson, D. J. Larson, N. Tabat, A. Cerezo, A. K. Petford-Long, G. D. W. Smith, P. H. Clifton, R. L. Martens and T. F. Kelly,

"Atomic Scale Structure of Sputtered Metal Multilayers," *Acta Materialia,* vol. 49, pp. 4005-4015, 14 November 2001.

[197] M. Yamaguchi, M. Shiga and H. Kaburaki, "First-Principles Study on Segregation Energy and Embrittling Potency of Hydrogen in NiΣ5(012) Tilt Grain Boundary," *Journal of the Physical Society of Japan,* vol. 73, pp. 441-449, February 2004.

[198] B. Gludovatz, S. Wurster, T. Weingärtner, A. Hoffmann and R. Pippan, "Influence of impurities on the fracture behaviour of tungsten," *Philosophical Magazine,* vol. 91, pp. 3006-3020, 01 August 2011.

[199] J. H. Rose, J. R. Smith and J. Ferrante, "Universal features of bonding in metals," *Physical Review B,* vol. 28, pp. 1835–1845 1983.

[200] J. E. Jones, "On the Determination of Molecular Fields. II. From the Equation of State of a Gas," *Proceedings of the Royal Society of London. Series A,* vol. 106, pp. 463-477, 1 October 1924.

[201] D. McLean, *Grain Boundaries in Metals*. London: Oxford University Press, 1957.

[202] U. v. Barth and L. Hedin, "A local exchange-correlation potential for the spin polarized case. I," *Journal of Physics C: Solid State Physics,* vol. 5, p. 1629, 1972.

[203] O. Gunnarsson and B. I. Lundqvist, "Exchange and correlation in atoms, molecules, and solids by the spin-density-functional formalism," *Physical Review B,* vol. 13, pp. 4274-4298, 1976.

[204] M. Tang, L. P. Kubin and G. R. Canova, "Dislocation mobility and the mechanical response of b.c.c. single crystals: A mesoscopic approach," *Acta Materialia,* vol. 46, pp. 3221-3235, 1998.

[205] C. Woodward and S. I. Rao, "Flexible Ab Initio Boundary Conditions: Simulating Isolated Dislocations in bcc Mo and Ta," *Physical Review Letters,* vol. 88, p. 216402, 27 May 2002.

[206] Z. Chen, G. Lu, N. Kioussis and N. M. Ghoniem, "The crucial role of chemistry on mobile properties of dislocation," *Philosophical Magazine,* vol. 90, pp. 3757-3765, 2010/09/21 2010.

[207] N. Choly, G. Lu, W. E and E. Kaxiras, "Multiscale simulations in simple metals: A density-functional-based methodology," *Physical Review B,* vol. 71, p. 094101, 2005.

[208] G. J. Ackland and R. Thetford, "An improved N-body semi-empirical model for body-centred cubic transition metals," *Philosophical Magazine A,* vol. 56, pp. 15-30, 1987.

[209] V. Vitek, R. C. Perrin and D. K. Bowen, "The Core Structure of 1/2<111> Screw Dislocations in B.C.C. Crystals," *Philosophical Magazine,* vol. 21, pp. 1049-1073, 1970.

[210] M. S. Duesbery and W. Xu, "The motion of edge dislocations in body-centered cubic metals," *Scripta Materialia,* vol. 39, pp. 283-287, 1998.

[211] P. V. Nerikar, D. C. Parfitt, L. A. Casillas Trujillo, D. A. Andersson, C. Unal, S. B. Sinnott, R. W. Grimes, B. P. Uberuaga and C. R. Stanek, "Segregation of xenon to dislocations and grain boundaries in uranium dioxide," *Physical Review B,* vol. 84, p. 174105, 2011.

[212] Y. Murao, T. Taishi, Y. Tokumoto, Y. Ohno and I. Yonenage, "Impurity effects on the generation and velocity of dislocations in Ge," *Journal of Applied Physics,* vol. 109, p. 113502, 1 June 2011.

[213] J. Cheng and S. Nemat-Nasser, "A model for experimentally-observed high-strain-rate dynamic strain aging in titanium," *Acta Materialia,* vol. 48, pp. 3131-3144, 2000.

[214] A. Van Den Beukel and U. F. Kocks, "The strain dependence of static and dynamic strain-aging," *Acta Metallurgica,* vol. 30, pp. 1027-1034, 1982.

[215] Q. Wei, T. Jiao, K. T. Remash, E. Ma, L. J. Kesckes, L. Magness, R. Dowding, V. U. Kazykhanov and R. Z. Valiev, "Mechanical behavior and dynamic failure of high-strength ultrafine grained tungsten under uniaxial compression," *Acta Materialia,* vol. 54, pp. 77-87, 2006.

[216] Q. Wei, H. T. Zhang, B. E. Schuster, K. T. Ramesh, R. Z. Valiev, L. J. Kecskes, R. J. Dowding, L. Magness and K. Cho, "Microstructure and mechanical properties of super-strong nanocrystalline tungsten processed by high-pressure torsion," *Acta Materialia,* vol. 54, pp. 4079-4089, 2006.

[217] J. H. Saleh, "Perspectives in Design: The Deacon's Masterpiece and the Hundred-Year Aircraft, Spacecraft, and Other Complex Engineering Systems," *Journal of Mechanical Design,* vol. 127, pp. 845-850, 2005.

[218] E. Munch, M. E. Launey, D. H. Alsem, E. Saiz, A. P. Tomsia and R. O. Ritchie, "Tough, Bio-Inspired Hybrid Materials," *Science,* vol. 322, pp. 1516-1520, 5 December 2008.

[219] X. Li, W.-C. Chang, Y. J. Chao, R. Wang and M. Chang, "Nanoscale Structural and Mechanical Characterization of a Natural Nanocomposite Material: The Shell of Red Abalone," *Nano Letters,* vol. 4, pp. 613-617, 2004.

[220] B. J. F. Bruet, J. Song, M. C. Boyce and C. Ortiz, "Materials design principles of ancient fish armour," *Nature Materials,* vol. 7, pp. 748-756, 2008.

[221] S. J. Dillon, M. Tang, W. C. Carter and M. P. Harmer, "Complexion: A new concept for kinetic engineering in materials science," *Acta Materialia,* vol. 55, pp. 6208-6218 October 2007.

[222] J. Luo, H. Cheng, K. M. Asl, C. J. Kiely and M. P. Harmer, "The Role of a Bilayer Interfacial Phase on Liquid Metal Embrittlement," *Science,* vol. 333, pp. 1730-1733, 23 September 2011.

LIST OF JOURNAL PUBLICATIONS

1. **Zhiliang Pan**, F. Xu, S. N. Mathaudhu, L. J. Kecskes, W. H. Yin, X. Y. Zhang, K. T. Hartwig and Q. Wei, "Microstructural evolution and mechanical properties of niobium processed by equal channel angular extrusion up to 24 passes," *Acta Materialia,* vol. 60, pp. 2310-2323, 2012.

2. Z. Huang, H. Li, **Zhiliang Pan**, Q. Wei, Y. J. Chao and X. Li, "Uncovering high-strain rate protection mechanism in nacre," *Scientific Reports,* vol. 1, p. 148, 2011.

3. B. Schuster, J. Ligda, **Zhiliang Pan** and Q. Wei, "Nanocrystalline refractory metals for extreme condition applications," *JOM,* vol. 63, pp. 27-31, 2011.

4. Q. Wei, **Zhiliang Pan**, X. Wu, B. E. Schuster, L. J. Kecskes and R. Z. Valiev, "Microstructure and Mechanical properties at different length scales and strain rates of nanocrystalline tantalum produced by high-pressure torsion," *Acta Materialia,* vol. 59, pp. 2423-2436, April 2011.

5. Y. Z. Guo, Y. L. Li, **Zhiliang Pan**, F. H. Zhou and Q. Wei, "A numerical study of microstructure effect on adiabatic shear instability: Application to nanostructured/ultrafine grained materials," *Mechanics of Materials,* vol. 42, pp. 1020-1029, 2010.

6. **Zhiliang Pan**, Y. Li and Q. Wei, "Tensile properties of nanocrystalline tantalum from molecular dynamics simulations " *Acta Materialia,* vol. 56, pp. 3470-3480, August 2008.

7. **Zhiliang Pan**, Y. Guo, S. N. Mathaudhu, L. J. Kecskes, K. T. Hartwig and Q. Wei, "Quasi-static and dynamic mechanical properties of commercial-purity tungsten processed by ECAE at low temperatures " *Journal of Materials Science,* vol. 43, pp. 7379-7384, December 2008.

8. **Zhiliang Pan**, Y. Li and Q. Wei, "Molecular dynamics simulation of nanocrystalline tantalum under uniaxial tension," *Solid State Phenomena,* vol. 139, pp. 83-88, 2008.

VITA

Zhiliang Pan was born in Cao County, Shandong province, P.R. China on May 12, 1978. After completing high school in 1999, he attended Northwestern Polytechnical University in Xi'an, China. He graduated with a Bachelor of Engineering degree in 2003. From 2003-2006, he continued his study as a graduate student in the same university and graduated with a Master of Engineering degree in 2006. He then entered the Huawei Technologies Co., Ltd. and worked there as a software engineer to develop LAN switch driver program. After five months of working, he joined the University of North Carolina at Charlotte in the spring 2007 as a PhD student in the Department of Mechanical Engineering and Engineering Science.